M.A. Hoorn

Stress State Dependent Fracture Prediction in Shells

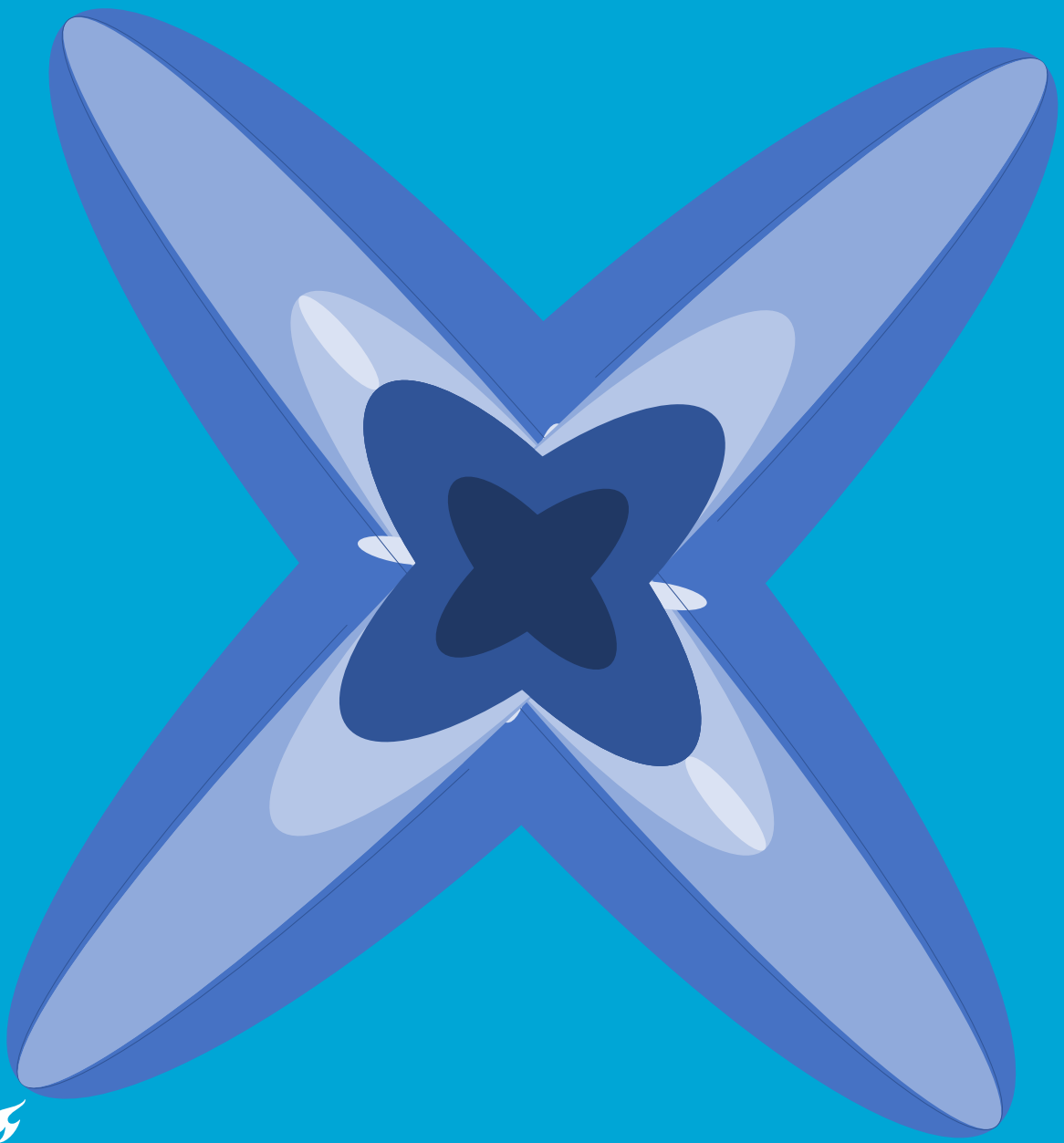

TU Delft

Stress State Dependent Fracture Prediction in Shells

By

M.A. Hoorn

in partial fulfilment of the requirements for the degree of

Master of Science
in Offshore and Dredging Engineering

at the Delft University of Technology,
to be defended publicly on Friday, October 25, 2020, at 10:00 AM.

Supervisor:	Dr.	C.L. Walters,	TU Delft
Thesis committee:	Dr. Ir.	S.A. Miedema,	TU Delft, chairman
	Ir.	O.J. Coppejans,	TNO, supervisor
	Dr. Ir.	J.H. den Besten,	TU Delft

TU Delft

Preface

This master thesis is submitted as part of the requirement for obtaining the degree of Master of Science in Offshore and Dredging Engineering at the Delft University of Technology (TU Delft).

I would like to express my sincere gratitude to everyone for their support and guidance throughout this work. First, I would like to thank Carey Walters, who guided me and helped me through research in prediction of ductile fracture and necking of hardening materials. Among other things, I appreciate the time taken to drive me to a path of progress during biweekly meetings and to help to understand what research already exists.

I would also like to thank Hossein Heidari for explaining his work on sheet instability. I would like to thank Okko Coppejans for listening to ideas in development and explaining existing and developing fracture prediction theories. Furthermore, I would like to thank Martijn Hoogeland, who helped to guide development to a practical product, together with Okko Coppejans and André van Erkel.

As a semi-final mention, but not least important is the family and friends, who supported me throughout my studies and encouraged me to continue development. As a final mention, I want to thank my friends and fencing friends for making the entire experience enjoyable and for widening my knowledge.

.

M.A. Hoorn

Delft September 2020

Contents

Abstract

The goal of this thesis is to propose a stress state dependent ductile fracture criterion for shell elements that can be used for crash simulations for example collisions of ships with offshore structures. Fracture has been extensively researched for solid elements for finite element analysis in Bai & Wierzbicki [2009], among others. Shells have also been investigated as a special case of the findings of solid elements. These elements are mostly used in large, thin-walled structures such as ships, as they reduce the minimum required elements in a model, which reduces computation time. Dunand & Mohr [2010] reported that these elements are unable to capture through-thickness necking. This necking localises strain and creates stress concentrations that decrease the validity of plane stress assumption of shells.

In contrast to prior research, this thesis focuses on shell elements that are in the range of 0.5 to 5 times the material thickness by proposing a phenomenological correction method. This method estimates the effective strain perpendicular to the neck at the instance of fracture based on the assumption that the stress state doesn't change at the onset of necking and a simplified analytical model of the neck itself.

The preference for a correction method is validated from a numerical plate model based on analysis proposed by Marciniak et al. [1973].

From comparison with the numerical results, it can be concluded that the proposed method performed better than existing methods for smaller shell elements lengths and similar for larger shell elements. The improvement is most dependent on the accuracy of the necking strain. A complete simplified approach for testing and effective fracture strain prediction is proposed and validated with calibration and raking experiments from Haag et al. [2017] and Bijleveld [2018].

Nomenclature

Latin Symbols

Symbol:	Meaning:	Unit:
[**F**]	Deformation gradient tensor	[-]
l_e	Element length	[mm]
L_{el}	Element length normalized by plate thickness	[-]
n	Hardening parameter	[-]
t	Time	[s]
t_p	Plate thickness	[mm]

Greek Symbols

Symbol	Meaning:	Unit:
α	Strain ratio	[-]
β	Stress ratio	[-]
γ	Element size dependency	[-]
ε	True strain	[-]
$\dot{\varepsilon}$	Strain rate	[s^{-1}]
$\bar{\varepsilon}_p$	Equivalent plastic strain	[-]
ε_{eq}^{f}	Equivalent plastic strain until fracture	[-]
ε_{eff}^{f}	Effective equivalent plastic strain until fracture	[-]
$\varepsilon_1^{f*}, \varepsilon_2^{f*}, \varepsilon_3^{f*}$	First, second, and third principal effective fracture	[-]
$\varepsilon_{1,F}, \varepsilon_{2,F}, \varepsilon_{3,F}$	First, second, and third principal fracture strain	[-]
$\varepsilon_{1,N}, \varepsilon_{2,N}, \varepsilon_{3,N}$	First, second, and third principal necking strain	[-]
$\varepsilon_1, \varepsilon_2, \varepsilon_3$	First, second, and third principal strain	[-]
η	Stress triaxiality	[-]
θ	Lode parameter/angle	[-]
$\bar{\theta}$	Linear mapped Lode parameter	[-]
θ_L	Xue Lode angle	[-]
$d\lambda$	Hardening parameter	[-]
ξ	Normalized Third Invariant of the stress deviator	[-]
σ	True stress	[N/mm^2]
$\bar{\sigma}$	Equivalent stress	[N/mm^2]
$\sigma_1, \sigma_2, \sigma_3$	First, second, third principal stress	[N/mm^2]
$\bar{\sigma}^f$	Equivalent fracture stress	[N/mm^2]
τ	Shear stress	[N/mm^2]

Symbol	Meaning:	Unit:
τ_{cr}	Critical shear stress	[N/mm^2]
$\tau_{\max}$	Maximum shear stress until fracture	[N/mm^2]
$\phi_{equivalent}$	Initial imperfection band angle with respect to σ_1 for a mirrored scenario	[rad]
ϕ_0	Initial imperfection band angle with respect to σ_1	[rad]

Acronyms

BWH	Bressan Williams Hill
DNV-GL	Det Norske Veritas - Germanischer Lloyd
DIC	Digital Image Correlation
DSSE	Domain of Shell to Solid Equivalence
TNO	Dutch Organization for Applied Scientific Research
EFFLD	Effective Fracture Forming Limit Diagram
FEM	Finite Element Method
FFLD	Fracture Forming Limit Diagram
FLD	Forming Limit Diagram
HC	Hosford-Coulomb
MK	Marciniak-Kuczynski
MMC	Modified Mohr-Coulomb
PMK	Post Marciniak-Kuczynski
RP	Recommended Practices
TUD	Technical University Delft

Table of figures

1 Introduction

1.1. Motivation

Ships are designed to withstand predefined accidental loading scenarios. These accidental scenarios include raking, grounding, or blast, and weapon effects. These scenarios are assessed with the Finite Element Method (FEM). For FEM, conservative fracture initiation models are used, for example DNV-GL RP-C204 from Det Norske Veritas [2010] and C208 from Det Norske Veritas [2013]. These models increase the required resilience of a design to survive a scenario, increasing both minimum weight and costs. With improved accuracy, a design can possibly still satisfy specific design scenarios, while reducing costs and weight of that design. Therefore, the focus in this thesis is to improve accuracy of fracture prediction in shell elements used to model ships in FEM.

Fracture is extensively researched for solid elements for FEM by several authors; for example, Tvergaard and Needleman [1984], Bai & Wierzbicki [2009], Mohr & Marcadet [2015], among others. These papers propose methods for predicting the fracture strain depending on how a solid element is stressed, in other words its stress state. However, shell elements are mostly used in crash simulations due to their computational efficiency, as one element can describe the entire thickness and a larger surface than a solid element. However, stresses in shells are limited to plane stress, which, as mentioned by Dunand & Mohr [2010], makes them unable to capture through-thickness necking. Through-thickness necking is the instability caused by local plate thinning in an area called the neck, which results in a strain localization. Through-thickness necking is accounted for in a limited manner with failure criteria which have an inverse linear dependence on element length in recommended practices (RP's) that are given by classification societies. These previously mentioned RP's neglect stress state dependency of both fracture and necking strain. Besides the previously mentioned methods, one can also use stress state dependent fracture or through-thickness necking criteria as was proposed for sheets by Goodwin [1968] and Keeler [1961]. The through-thickness necking criteria is used to estimate the failure strain of shell elements, because at that point, strains localise, and only a local volume will achieve the fracture strain. As previously mentioned, the shell element does not capture through-thickness necking. Therefore, necking or fracture criteria will underestimate or overestimate, respectively, the equivalent plastic strain at which fracture is initiated in a shell element when necking precedes fracture. This failure strain is henceforth referred to as the effective fracture strain. This effective fracture strain is equal to the fracture strain when fracture precedes necking because no correction is required. There are correction methods for when necking precedes fracture. These homogenise the strain in and outside the neck, for example, Ehlers et al. [2008], and Walters [2014]. These methods only work for shell element lengths larger than five times the material thickness. This makes it

desirable, for future application, to use a benchmark to find out how current methods perform at different element sizes and stress states.

1.2. Objective and Scope

The first objective of this thesis is to find and validate methods for obtaining the effective fracture strain for different element sizes and stress states. The second objective is to extend the limits of existing methods such as proposed in Walters [2014], for elements smaller than five times the plate thickness. Therefore, this thesis aims to answer the following question:

How can ductile fracture strains for hardening materials be converted to effective fracture strains in shell elements with practical dimensions for crash simulation?

As of now, it is not clear how the neck influences the effective fracture strain. This question is answered partly by the following research questions based on the literature review found in Appendix A:

1. **How can the accuracy of stress state dependent ductile fracture prediction models for shell elements be evaluated?**
2. **How do fracture strains in solids translate to effective fracture strains in shells smaller than five times the plate thickness?**
3. **What are the effects of boundary conditions on through-thickness necking?**

Plates are often modelled with shell elements. In this thesis, detailed models of plates are made with solid elements that represent the shell elements, which requires boundary conditions that accurately represent a shell in a field of shell elements in a real structure.

1.3. Thesis Outline

This thesis starts in Chapter 2 by providing background information, such as stress state and what a plasticity model is. The subsequent chapters are aiding in answering the main research question. The main assumption in this thesis is that shells cannot capture fracture when it is preceded by through-thickness necking. However, it is possible to correct for necking in failure strain for shells and methods for this are presented in Chapter 3, answering the second sub research question. These methods determine the effective fracture strain by homogenizing the strain inside and outside the neck over the element length (Bijleveld, 2018; Walters, 2014), or by estimating the shape of the neck. The accuracy of these methods is validated with a solid model of a plate which can capture through-thickness necking. This model is described in Chapter 4, calibrated in Chapter 5, and the performance of the presented methods is evaluated in Chapter 6. Together, these chapters answer the first sub research question. This model uses a set of boundary conditions which are further assessed in Chapter 7. The thesis and research questions are

concluded in Chapter 8, and recommendations for future research are reported in chapter 9. At the end of the thesis in Chapter 10, the most critical assumptions are discussed.

2 Background

Stress-state dependent ductile fracture prediction methods use terms not often used in general engineering; therefore, these are explained within this chapter and used throughout the thesis.

Main assumptions

The material deformation is assumed fully plastic as the elastic strains are negligible for fracture prediction. This assumption allows the assumption of conservation of volume in equation 2.1 relating the three principal strains:

$$(\varepsilon_1 + 1)(\varepsilon_2 + 1)(\varepsilon_3 + 1) = 1 \tag{2.1}$$

with $\varepsilon_1, \varepsilon_2, \varepsilon_3$ as the main principal strains.

The direction in which plastic strain increments $d\varepsilon_{ij}$ occur is assumed to be normal to the yield surface, with the associated flow rule shown in equation 2.2:

$$d\varepsilon_{ij} = d\lambda \frac{\partial \bar{\sigma}}{\partial \sigma_{ij}} \tag{2.2}$$

with:

- $\bar{\sigma}$ as the equivalent stress
- $d\lambda$ as the hardening parameter, which is dependent on the equivalent plastic strain $\bar{\varepsilon}_p$ shown in equation 2.3.

$$d\bar{\varepsilon}_p = \frac{\sqrt{2}}{3}\sqrt{(d\varepsilon_1 - d\varepsilon_2)^2 + (d\varepsilon_2 - d\varepsilon_3)^2 + (d\varepsilon_3 - d\varepsilon_1)^2} \tag{2.3}$$

The plastic strain can be simplified to equation 2.4, as shown by Lee [2005], small strains, plane stress, proportional straining, and conservation of volume.

$$d\bar{\varepsilon}_p = d\varepsilon_1 \frac{2}{\sqrt{3}}\sqrt{\alpha^2 + \alpha + 1} \rightarrow d\varepsilon_1 = d\bar{\varepsilon}_p \frac{\sqrt{3}}{2}\frac{1}{\sqrt{\alpha^2 + \alpha + 1}} \tag{2.4}$$

with the strain ratio α from equation 2.5 for proportional straining.

$$\alpha = \frac{d\varepsilon_2}{d\varepsilon_1} \approx \frac{\varepsilon_2}{\varepsilon_1} \tag{2.5}$$

The fracture models applied in this thesis use the von Mises equivalent stress $\bar{\sigma}$ in equation 2.6.

$$\bar{\sigma} = \sqrt{\frac{1}{2}[(\sigma_1 - \sigma_2)^2 + (\sigma_2 - \sigma_3)^2 + (\sigma_3 - \sigma_1)^2]} \tag{2.6}$$

with σ_1,σ_2, and σ_3 as the first, second and third principal stress.

The relation between stress and strain can be estimated with Hencky's equations in equation 2.7, which is derived from the associated flow rule and assumes incompressibility.

$$\frac{d\varepsilon_1}{2\sigma_1-\sigma_2-\sigma_3}=\frac{d\varepsilon_2}{2\sigma_2-\sigma_1-\sigma_3}=\frac{d\varepsilon_3}{2\sigma_3-\sigma_1-\sigma_2}=\frac{d\bar{\varepsilon}_p}{\bar{\sigma}} \tag{2.7}$$

Besides the magnitude of strain, the state of stress is also of importance in fracture prediction (McClintock, 1968; Rice & Tracey, 1969; Hancock & Mackenzie, 1976; Johnson & Cook, 1985; Bao & Wierzbicki, 2003; Mohr & Marcadet, 2015) , which is in this thesis mainly expressed with stress triaxiality η in equation 2.8 as proposed by Rice & Tracey [1969].

$$\eta=\frac{\sigma_m}{\bar{\sigma}} \tag{2.8}$$

with σ_m as the average stress in equation 2.9.

$$\sigma_m=\frac{\sigma_1+\sigma_2+\sigma_3}{3} \tag{2.9}$$

For plane stress ($\sigma_3=0$), η can be expressed with equation 2.10.

$$\eta=\frac{\sigma_1+\sigma_2}{3}\frac{1}{\sqrt{-\sigma_1\sigma_2+{\sigma_2}^2+{\sigma_1}^2}}=\frac{1+\beta}{3}\frac{1}{\sqrt{\beta^2-\beta+1}} \tag{2.10}$$

with β as the stress ratio in equation 2.11.

$$\beta=\frac{\sigma_2}{\sigma_1} \tag{2.11}$$

The stress ratio is expressed in strain ratio in equation 2.12 by assuming von Mises yield function, constant strain path, proportional straining, and associated flow rule.

$$\beta=\frac{1+2\alpha}{\alpha+2} \tag{2.12}$$

The Lode parameter $\overline{\theta}$ (Lode, 1925) is a useful parameter that was first associated to ductile fracture by Rice and Tracey [1969]. This Lode parameter can be obtained with the third normalized invariant ξ (Malvern, 1969) of the stress tensor, as is shown by Wierzbicki & Xue [2005] and Bai & Wierzbicki [2008a] in equation 2.13. In the case of plane stress, the Lode parameter can be related to the stress triaxiality as shown in equation 2.14.

$$\xi=cos(3\theta\,)=cos[\frac{\pi}{2}(1-\overline{\theta})]=-\frac{27}{2}\eta\left(\eta^2-\frac{1}{3}\right) \tag{2.13}$$

$$\overline{\theta}=1-\frac{2}{\pi}\cos^{-1}\left[-\frac{27}{2}\eta\left(\eta^2-\frac{1}{3}\right)\right] \tag{2.14}$$

See Table 1 for η, $\overline{\theta}$, and ξ of unique plane stress states which are also plotted in Figure 1 together with $\overline{\theta}$ as function of η for plane strain and stress.

Table 1 Unique stress states and their triaxiality, Lode parameter and third invariant.

STRESS STATE	CONDITION	η	$\overline{\theta}$	ξ
UNI-AXIAL	$\sigma_2 = \sigma_3 = 0$	1/3	-1	1
EQUI-BIAXIAL	$\sigma_1 = \sigma_2$ $\sigma_3 = 0$	2/3	1	-1
PLANE STRAIN	$\sigma_3 = 0$ $\varepsilon_3 = 0$	$1/\sqrt{3}$	0	0

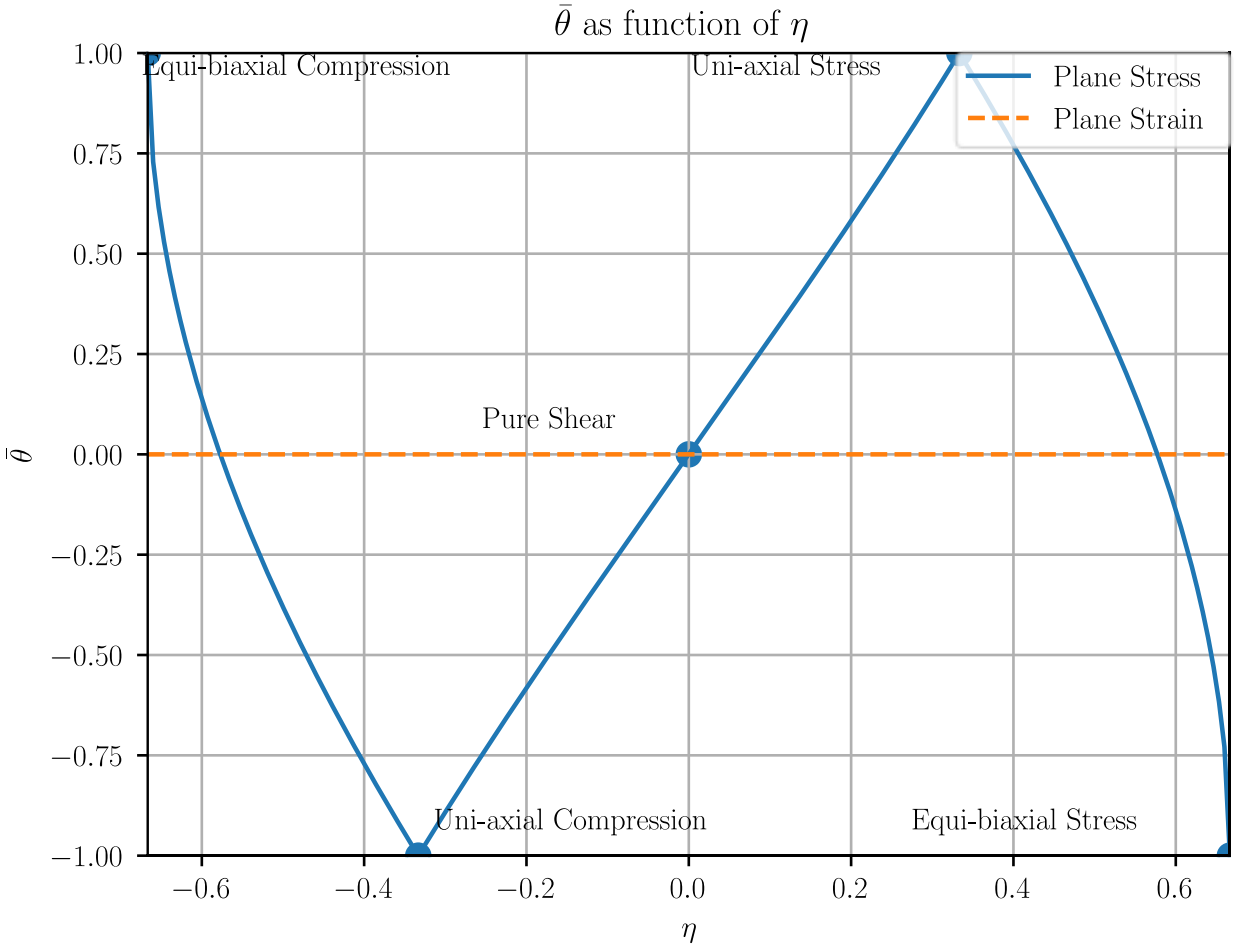

Figure 1 Lode Parameter as a function of stress triaxiality from Wierzbicki & Xue [2005]

The hardening model describes the relationship between plastic strain and stress. This section explains how this relation is obtained from a uniaxial tensile test based on the approach used by Dunand & Mohr [2010]. The method starts by obtaining the true stress strain curve from extensometer and load cell measurements. These provide length and force measurements, which are converted to true stress and strain with the classical formulas in equation 2.15 and 2.16.

$$\bar{\varepsilon}_{eq} = \ln\left(\bar{\varepsilon}_{eng} + 1\right) \tag{2.15}$$

$$\bar{\sigma} = \bar{\sigma}_{eng}\left(\bar{\varepsilon}_{eng} + 1\right) \tag{2.16}$$

with:

- $\bar{\varepsilon}_{eng}$ as the engineering strain obtained by dividing the new gage length with its original length.
- $\bar{\sigma}_{eng}$ as the engineering stress obtained by dividing the measured force by the original area of the cross-section of the gage length.
- $\bar{\sigma}$, and $\bar{\varepsilon}_{eq}$ as the true stress and strain, respectively.

The true stress strain relation is fitted with a hardening model. For example, the hardening proposed by Swift [1952] $\bar{\sigma}_{\mathrm{Swift}}$ in equation 2.17 or by Voce [1948] $\bar{\sigma}_{\mathrm{Voce}}$ in equation 2.18 or a combination of the two as proposed by Alsos et al. [2008] $\bar{\sigma}_{\mathrm{Voce+Swift}}$ in equation 2.19.

$$\bar{\sigma}_{\mathrm{Swift}} = K\left(\varepsilon_0 + \bar{\varepsilon}_p\right)^n \tag{2.17}$$

$$\bar{\sigma}_{\mathrm{Voce}} = k_0 + Q\left[1 - exp\left(-\beta_v \bar{\varepsilon}_p\right)\right] \tag{2.18}$$

$$\bar{\sigma}_{\mathrm{Voce+Swift}} = \alpha_{VS} \cdot \bar{\sigma}_{\mathrm{Voce}} + (1 - \alpha_{VS}) \cdot \bar{\sigma}_{\mathrm{Swift}} \tag{2.19}$$

With ε_0, K, n, k_0, Q, α_{VS} and β_v as material parameters.

The classical formulas presented in equation 2.15 and 2.16 assume that the plate keeps a constant cross-section over its length during deformation, which is valid until strains localize and the stress reaches a maximum (ultimate tensile strength). This point is called necking and can be obtained with the Considère condition in equation 2.20 (Considère, 1885).

$$\frac{d\sigma_1}{d\varepsilon_1} = \sigma_1 \tag{2.20}$$

After necking, the true stress relation can be calibrated with a Finite Element Method (FEM) model of the tensile test. The correct hardening model is obtained by adjusting the hardening model parameters in FEM until the force displacement curve of the FEM model and tensile test converge. The model only simulates the gage length as the displacement is known from the extensometer.

The FEM model of the tensile test requires solid elements to capture deformation correctly. The size of the elements is determined by the thickness for example, Lee [2005] recommends 12 elements through the half-thickness, and Bijleveld [2018] obtained convergence with six elements through the half-thickness. These models require an imperfection in width over the cross-section at the centre of the specimen to initiate necking as the simulation represents a perfect plate which the tensile test specimen is not.

3 Failure criteria

3.1. Introduction

This chapter aims to partially answer the first research question:
"*How do fracture strains in solids translate to effective fracture strains in shells smaller than five times the plate thickness?*". This is done by answering how the fracture and necking strain are predicted and explaining why and how the fracture strain is corrected.

Outline

A logical failure criterion for shell elements is the fracture strain of the material (Paragraph 3.2), obtained from Fracture Forming Limit Diagram (FFLD). Another failure criterion is the strain at which the strains localise through the thickness (Paragraph 3.3) because, after necking global strain to ultimate failure is relatively small over larger length scales. The deformation between necking and ultimate failure is evaluated by adjusting fracture strain with the necking strain as a function of element size (Paragraph 3.4). These methods are only recommended for larger element sizes because then the neck can be treated as if it is negligible relative to the element, as implied by Ehlers [2009]. A theoretical correction model is proposed (Paragraph 3.5) for smaller elements. The method determines the strain experienced by a shell element when it fractures by estimating the strain inside and outside the neck. For reference, the recommended practices for predicting fracture are presented (Paragraph 3.6).

3.2. Fracture Criteria

Only two stress state dependent phenomenological ductile fracture criteria are considered in this thesis. These are the Hosford Coulomb (HC) from Mohr & Marcadet [2015] and Modified Mohr Coulomb (MMC) from Bai & Wierzbicki [2008] models/approaches, as these agree with fracture strains found in experiments in terms of accuracy expressed in Root Mean Square Error (RMSE) for DH36 (Park et al., 2019) and S235 (Bijleveld et al., 2018). Alternative fracture models do exist but are not used within this thesis. An example is the continuum damage model called the Gurson-Tvergaard-Needleman damage model. This model is based on the porous ductile material model proposed by Gurson [1977] and revised by Tvergaard [1982] and Tvergaard and Needleman [1984].
The MMC is based on a maximum stress combination in equation 3.1 (Coulomb, 1776).

$$max(\tau + c_1\sigma_n) = c_2 \tag{3.1}$$

with c_1 as a slope relation between shear and normal stress and c_2 cohesion.

This maximum stress combination was expressed in terms of stress-triaxiality and Lode parameter in equation 3.2 (Bai & Wierzbicki, 2008).

$$\bar{\sigma}^f(\eta,\bar{\theta}) = c_2\left[\sqrt{\frac{1+c_1^2}{3}}\cos\left(\frac{\pi}{6}-\bar{\theta}\right)+c_1\left(\eta+\frac{1}{3}\sin\left(\frac{\pi}{6}-\bar{\theta}\right)\right)\right]^{-1} \tag{3.2}$$

The MMC model is expressed in terms of equivalent plastic strain in equation 3.3 as proposed by Bai et al. [2008], by assuming: von Mises plasticity, monotonic loading, and a stress state dependent hardening model:

$$\varepsilon_{\mathrm{eq}}^f(\eta,\bar{\theta}) = \left(\frac{K}{c_2}\left[\sqrt{\frac{1+c_1^2}{3}}\cos\left(\frac{\bar{\theta}\pi}{6}\right)+c_1\eta+\frac{1}{3}\sin\left(\frac{\bar{\theta}\pi}{6}\right)\right]\right)^{\frac{1}{n}} \tag{3.3}$$

This relation can be reduced to one calibration parameter as suggested by Voormeeren et al. [2014] for plane stress and stress triaxialities between one third and two thirds, and this represents the maximum shear stress criterion.

The Hosford-Coulomb (HC) model in equation 3.4 was introduced in Mohr & Marcadet [2015] and is a micro mechanically motivated model which is quite similar to the MMC. This equation is rewritten in terms of η and $\overline{\theta}$ in equation 3.5 for future application with a maximum von Mises stress $\bar{\sigma}^f$.

$$(\frac{1}{2}[(\sigma_1-\sigma_2)^a+(\sigma_2-\sigma_3)^a+(\sigma_1-\sigma_3)^a])^{\frac{1}{a}}+c(\sigma_1+\sigma_3)=b \tag{3.4}$$

$$\bar{\sigma}^f(\eta,\bar{\theta}) = \frac{b}{\{\frac{1}{2}[(f_1-f_2)^a+(f_2-f_3)^a+(f_1-f_3)^a]\}^{\frac{1}{a}}+c(2\eta+f_1+f_3)} \tag{3.5}$$

With:

$$f_1[\overline{\theta}] = \frac{2}{3}\cos\left(\frac{\pi}{6}(1-\overline{\theta})\right), f_2[\overline{\theta}] = \frac{2}{3}\cos\left(\frac{\pi}{6}(3+\overline{\theta})\right), f_3[\overline{\theta}] = -\frac{2}{3}\cos\left(\frac{\pi}{6}(1+\overline{\theta})\right) \tag{3.6}$$

This equation has three calibration parameters a, b, and c. For a direct link to experiments, the HC model is converted to equivalent plastic strain to failure with hardening models from Swift [1952] and Voce [1948] equation 2.20. These parameter effects can be described as followed:

- a determines Lode angle and triaxiality dependency if $c = 0$ and $a = 2$ the function becomes the von Mises yield criterion.
- b adjusts locus height in stress and strain.
- c determines Lode angle and triaxiality dependency, as for $c = 0$, the function becomes independent of the stress triaxiality and becomes symmetric in the Lode angle.

One can modify this model to two calibration parameters with the plane stress assumption for shell elements. The main difference in the performance of the HC model and MMC model is found between uni- and equi-biaxial tension (plain stress) as the MMC does not include the second principal stress.
The HC can be translated to strain space for proportional loading and only plane stress in equation 3.7.

$$\varepsilon_{\mathrm{eq}}^{f}[\eta] = b(1+c)^{\frac{1}{n_f}}\left[\left\{\frac{1}{2}\left((g_1-g_2)^a + g_1^a + g_2^a\right)\right\}^{\frac{1}{a}} + cg_1\right]^{-\frac{1}{n_f}} \tag{3.7}$$

with g_1 and g_2 in equation 3.8 and 3.9 respectively:

$$g_1[\eta] = \frac{3}{2}\eta + \sqrt{\frac{1}{3} - \frac{3}{4}\eta^2} \tag{3.8}$$

$$g_2[\eta] = \frac{3}{2}\eta - \sqrt{\frac{1}{3} - \frac{3}{4}\eta^2} \tag{3.9}$$

with $n_f = 0.1$ as the fixed transformation coefficient as suggested by Roth & Mohr [2016].The HC model uses the primary and secondary band of localization as a failure criterion. The primary band is caused by pre-existing voids that evolve while new ones nucleate. This increases porosity and work hardening of the material.

3.3. Failure Criteria from Standards

Det Norske Veritas - Germanischer Lloyd (DNV-GL) defined failure criteria in Recommended Practices (RP) C208 (Det Norske Veritas, 2013) and C204 (Det Norske Veritas, 2010) which are shown in equations 3.10 and 3.11, respectively. These are generalized fracture criteria for steel plates

$$\varepsilon_1^f = \varepsilon_{crg}\left(1 + \frac{5t_p}{3l_e}\right) \tag{3.10}$$

$$\varepsilon_1^f = 0.02 + 0.65\frac{t_p}{l_e} \tag{3.11}$$

with:

- ε_{crg} calibrated with a FEM simulation of a strained plate.
- t_p as the plate thickness.
- l_e as the element length.

DNV-RP-C204 states a maximum strain, but not a maximum principal strain or equivalent plastic strain, which results in two separate failure criteria.

3.4. Necking Criteria

The instant at which strain starts to localise can be determined experimentally or estimated with analytical models presented in this paragraph. Hill [1952] proposed for through-thickness necking that a line exists at an angle ϕ with respect to the first principal stress σ_1 of zero extension parallel to the line. This angle ϕ is given by Hill [1952] in equation 3.12 for $-0.5 \leq \alpha \leq 0$, and is $90°$ for $0 < \alpha \leq 1$.

$$\phi = \arctan\left(\frac{1}{\sqrt{-\alpha}}\right) \tag{3.12}$$

The necking criterion is obtained with the assumption that necking will occur when the capacity loss due to thickness reduction equals the increased capacity caused by work hardening in equation 3.13 for plane stress ($-0.5 \leq \alpha \leq 1$).

$$\frac{d\sigma_1}{\sigma_1} = -d\varepsilon_3 = (1+\alpha)d\varepsilon_1 \tag{3.13}$$

The difference between the Considère condition and Hill necking criterion is that the latter takes into account differences in stress state into account with thickness reduction while the Considère condition in equation 2.21 only takes into account that the critical stress in one direction into account. These two conditions intersect at plane strain ($\alpha = 0$).

Bressan & Williams [1983] proposed a model with a plane of zero extension, expressed in equation 3.14 for stress states between plane strain and equi-biaxial strain ($0 < \alpha < 1$). This angle is represented by ϕ in Mohr's circle defined by equation 3.15.

$$d\varepsilon_{33} = d\varepsilon_1 \sin^2\phi + d\varepsilon_3 \cos^2\phi = d\varepsilon_1(\sin^2\phi - (1+\alpha)\cos^2\phi) = 0 \tag{3.14}$$

$$\cos(2\phi) = -\frac{\alpha}{2+\alpha} \tag{3.15}$$

In this plane, shear is expressed for plane stress, as shown in equation 3.16. Strain localization is expected at a critical value of shear τ_{cr} in equation 3.17. This shear is expressed in equation 3.18 with von Mises plasticity and associated flow rule.

$$\tau \equiv \sigma_{12} = (\sigma_3 - \sigma_1)\cos\varphi \sin\varphi = -\frac{\sigma_1}{2}\sin 2\phi \tag{3.16}$$

$$|\tau| = \frac{\sigma_1}{2}\sqrt{1 - \left(\frac{\alpha}{2+\alpha}\right)^2} = \tau_{cr} \tag{3.17}$$

$$\bar{\sigma} - \sqrt{3}\tau_{cr}\frac{\sqrt{1+\beta+\beta^2}}{\sqrt{1+\beta}} = 0 \tag{3.18}$$

The Bressan-Williams is a through thickness necking criterion at which a critical shear causes instability instead of first principal stress used by the Hill necking criterion and Considère condition.

Alsos et al. [2008] combined these different necking criteria in equation 3.19 and 3.20 for two ranges of α. These equations are in terms of first principal necking strain by assuming power law hardening, von Mises plasticity, and the associated flow rule.

$$\varepsilon_1^n = \frac{\widehat{\varepsilon_1}}{1+\alpha} \quad , for\ \alpha \leq 0 \tag{3.19}$$

$$\varepsilon_1^n = \frac{1}{\sqrt{\alpha^2+\alpha+1}}\left(\frac{\varepsilon_1^{-2n}(\alpha+1)}{\alpha^2+\alpha+1}\right)^{-\frac{1}{2n}} \quad , for\ \alpha > 0 \tag{3.20}$$

with $\hat{\varepsilon_1}$ = n as a calibration parameter, so that the necking strain at $\alpha = 0$ is the same for both necking criteria.

Swift [1952] proposed an extension of the Considère condition in equation 2.21 for biaxial loads. This maximum force criterion is for diffuse necking when two perpendicular loads simultaneously reach a maximum force resulting in equation 3.21 for plane stress ($-0.5 \leq \alpha \leq 1$).

$$\frac{d\sigma_1}{d\varepsilon_1} = \sigma_1 \text{ and } \frac{d\sigma_2}{d\varepsilon_2} = \sigma_2 \tag{3.21}$$

This necking criterion equals the Considère condition for uniaxial stress state ($\alpha = -0.5$) and equi-biaxial stress state ($\alpha = 1$).

Stören & Rice [1975] proposed a method to allows the neck to form in plane strain with bifurcation, and a solution is constructed in equation 3.22 by Stoughton & Zhu [2004].

$$\begin{pmatrix} \varepsilon_1 \\ \varepsilon_2 \end{pmatrix} = \begin{pmatrix} \frac{3\alpha^2+n(2+\alpha)^2}{2(1+2\alpha)(1+\alpha+\alpha^2)} \\ \frac{\alpha(3\alpha^2+n(2+\alpha)^2)}{2(1+2\alpha)(1+\alpha+\alpha^2)} \end{pmatrix} \tag{3.22}$$

Marciniak-Kuczynski analysis (MK-analysis) as proposed by Marciniak et al. [1973] simulates an infinite plate with a thin band that has a smaller thickness, representing an initial imperfection that promotes necking, and increasing strains until it necks. The necking point is described by Safikhani et al. [2009] in equation 3.23.

$$\left|\frac{d\varepsilon_3^B}{d\varepsilon_3^A}\right| > 10 \tag{3.23}$$

with:

- ε_3^B = through-thickness strain in the neck.
- ε_3^A = through-thickness strain outside the neck.

This method is implemented in FEM with shell elements by Pack & Mohr [2017] with incrementally increasing displacement constraints to apply strain. These constraints are mirrored on each edge of the plate, as shown in Figure 2, to strain the plate in multiple strain ratios and stress states. The onset of necking is described in equation 3.24 by a triaxiality change due to localization as defined by Pack & Mohr [2017].

$$\left|\frac{d\eta}{d\bar{\varepsilon}_p}\right| \gg 1 \tag{3.24}$$

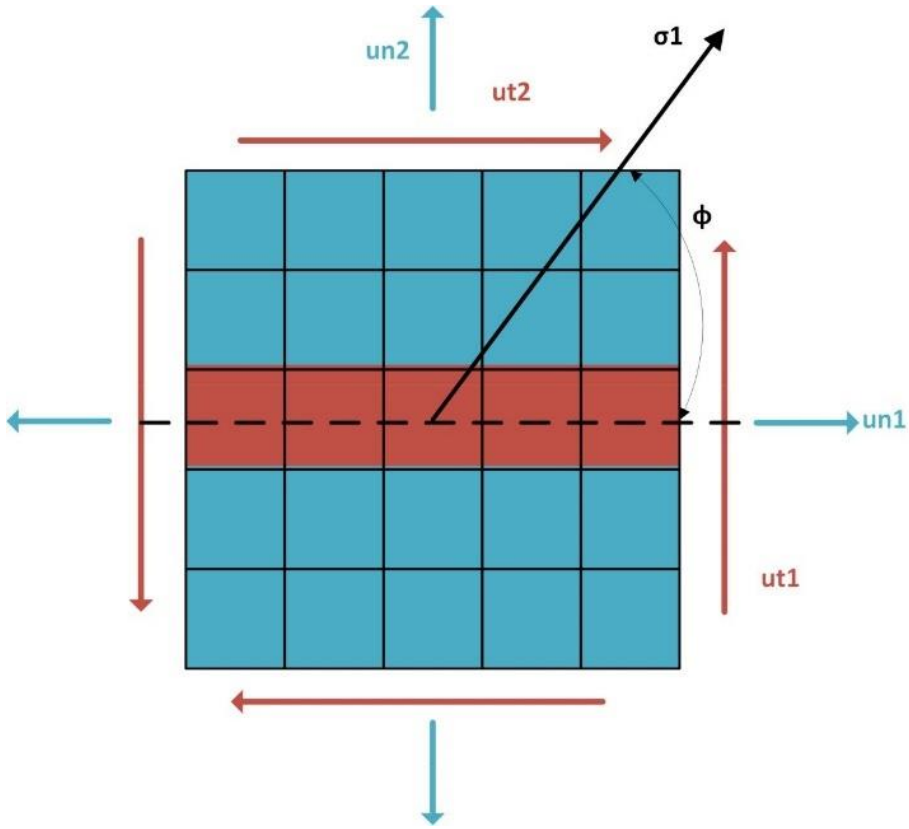

Figure 2 Boundary conditions on a plate for MK analysis as suggested by Pack & Mohr [2017]

Alternatively, for a plate loaded by membrane stress that necks before fracture, the difference in effective fracture strain applied on the boundaries and necking strain reduces with increasing element size. This relation can be used as a necking criterion in FEM simulations, as shown in equation 3.25.

$$\lim_{\frac{l_e}{t_p}\to\infty} \varepsilon^f_{\text{eff}}\left(\frac{l_e}{t_p},\eta\right) \to \min\left(\varepsilon^n_{eq}(\eta),\varepsilon^f_{\text{eq}}(\eta)\right) \tag{3.25}$$

Within this thesis, the MK analysis is performed with FEM. For comparison a more conventional method is used in this thesis based on Safikhani et al. [2009] and a script provided by H. Heidari. This approach analyses a plate strained with a specific strain ratio (α), and initial thickness imperfection (f_0) over a band with an initial angle (ϕ_0) between the band and the direction of the first principal strain (ε_1). The method analyses force equilibrium orthogonal to the necking band over a cross-section through the thickness over a length L_0 orthogonal to the imperfection band. The initial thickness imperfection is distributed as shown in equation 3.26 over L_0.

$$t = t_p + t_p(f_0 - 1)\,cos\left(\frac{x}{2L_0}\pi\right), for\ x \le L_0 \tag{3.26}$$

With:

- x as the distance orthogonal to the neck band orientation from the centre of the imperfection.

- f_0 as the thickness imperfection ratio which is the ratio of the minimum and maximum initial plate thickness.

The strain is incrementally increased by applying an initial deformation in the thickness $\Delta t = -0.005 t_p$. The actual deformation is solved for the equilibrium of forces, with the exception at $x = 0$ to increase strain. The strain is incrementally increased until equation 3.23 is satisfied with ε_3^B from $x = 0$ and ε_3^A from $x = L_0$. For more detailed information, see Safikhani et al. [2009], but the strain gradient in that paper is neglected, and the hardening model is defined by Voce-Swift as defined in equation 2.19.

3.5. Effective Fracture Strain Correction for Shell Element Size

This section is devoted to explaining correction methods for fracture strain for different shell element sizes as shells cannot describe strain after through-thickness necking (Dunand & Mohr, 2010). The framework from Walters [2014] is presented along with a corrected version suggested by Bijleveld et al. [2018] and alternative methods.

Analysis of current methods

One primary method for correcting the effective fracture strain is proposed by Ehlers et al. [2008] in equation 3.27 for the uniaxial stress state. This equation homogenises a local neck within a length t_p over a large element length $l_e > 5t_p$.

$$\varepsilon_{eff}^f \left(\frac{t_p}{l_e}\right) = n + \left(\varepsilon_n^f - n\right)\frac{t_p}{l_e} \tag{3.27}$$

with:

- n as the hardening exponent from equation 2.17. This is the assumed homogenous strain outside the neck and is obtained from the Considère condition in equation 2.20 and the Swift hardening model in equation 2.17.
- ε_n^f as the effective fracture strain at $t_p/l_e = 1$ at the uniaxial stress state.

This method assumes that the neck is within the element and is a function of t_p/l_e as the neck length is assumed proportional to the plate thickness (t_p) as proposed by Scharrer [2002]. Equation 3.27 is similar to the empirically derived equation 3.10 from collision tests in Scharrer [2002] for larger element lengths.
The application of equation 3.27 is extended to plane stress by using stress state dependent fracture and necking loci, as proposed by Walters [2014] in equation 3.28. This extension is also only applicable for $l_e > 5t_p$ and when necking precedes fracture as otherwise the effective fracture strain is equal to the fracture strain.

$$\varepsilon_{eff}^f(\eta, l_e) = \varepsilon_{eq}^n(\eta) + \left(\varepsilon_{eq}^f(\eta) - \varepsilon_{eq}^n(\eta)\right)\gamma = A(\eta) + B(\eta)\gamma \tag{3.28}$$

with γ as the element size dependency as function of t_p/l_e. Multiple interpretations of this function are possible, Ehlers [2008] and Walters [2014] defined it as in equation 3.29.

$$\gamma = \frac{t_p}{l_e} \tag{3.29}$$

The stress state dependent effective fracture strain in equation 3.29 is demonstrated to work (Walters, 2014) for a pressurized pipe test from Hwang et al. [2009].

The relation of equation 3.28 and 3.29 can be validated by optical measurement of a fractured plate with different field sizes representing shells elements with varying lengths from Tang et al. [2015]. This

A non-linear, element-size dependency is proposed in equation 3.30 by Bijleveld [2018]. This equation is non-linear to have a maximum effective fracture strain equal to the fracture strain. The range of element size dependency is equal to $0 \leq \gamma \leq 1$.

$$\gamma = \tanh\left(c_3 \left[\frac{t_p}{l_e}\right]^{c_4}\right) \tag{3.30}$$

with c_3 and c_4 calibrated with a tensile test for different mesh sizes. This method of calibration includes the diffuse necking during the tensile test, which makes equation 3.30 only valid for the tensile test with which it is calibrated.

The applicability of correction methods varies with element size:

- $\boldsymbol{0 \leq l_e/t_p < 0.2}$ The ability of shell elements to capture the engineering stress and strain relation diverges with smaller elements in this range. For indication, see Figure 3 from Park et al. [2018] who showed the capability of shell and solid elements to capture post-necking of a tensile test for EH36. All element lengths have the same Hollomon power law model proposed by Hollomon [1945], which is equal to equation 2.18 with $\varepsilon_0 = 0$, with material hardening parameters fitted with the engineering stress and strain before the onset of necking. The stress strain relation from experiments and models composed out of solid elements converge with smaller elements. This is also true for shell elements, but after $l_e/t_p = 0.2$ the stress and strain relation start to diverge.
- $\boldsymbol{0.2 < l_e/t_p < 5}$ Shell elements can contain 0 to 100% of the neck, and equation 3.29 does not describe element size dependence accurately for this range.
- $\boldsymbol{5 \leq l_e/t_p \leq 10}$ The neck is assumed to be contained within a shell element and can be homogenised over an element with equation 3.28 and 3.29.
- $\boldsymbol{l_e/t_p \gg 10}$ The post-necking strain becomes negligible relative to the necking strain. Instead of a correction method, the lowest failure strain, necking or fracture strain is proposed (Keeler, 1961; Goodwin, 1968; Pack & Mohr, 2017).

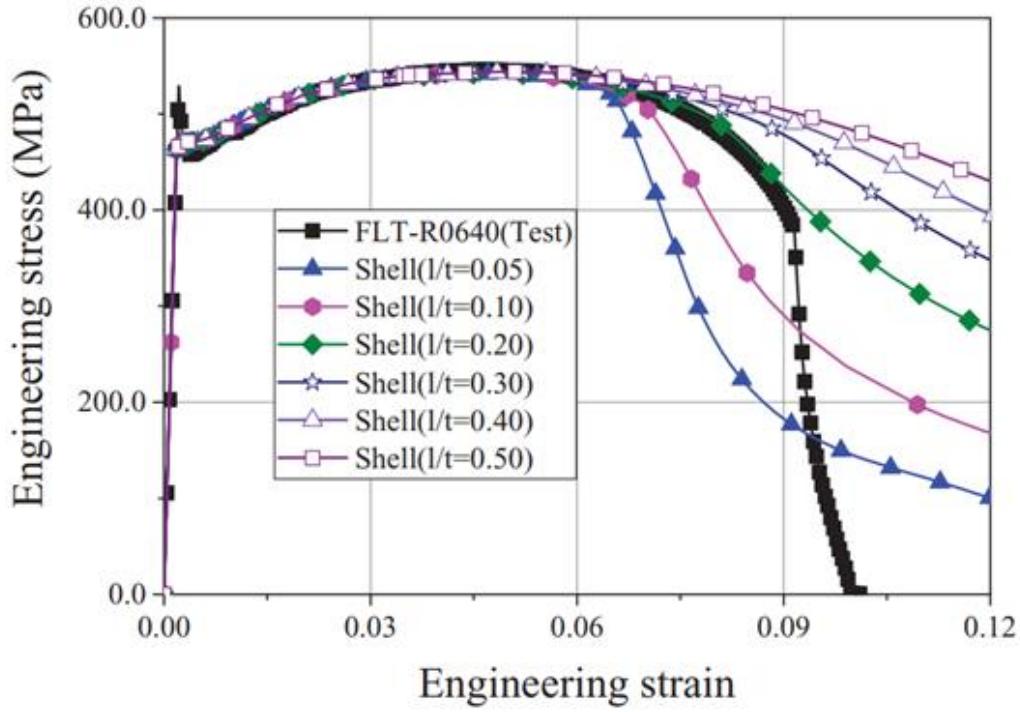

Figure 3 Capability of capturing pre and post-necking for shell elements (S4R) from Park et al. [2018].

Another method is suggested by Pack & Mohr [2017] called: Domain Shell to Solid Equivalence (DSSE). This method determines a domain in which through-thickness necking does not occur with MK-analysis. Within this domain, the fracture models for solids also apply to shells. This method uses the HC fracture locus to curve-fit the necking strains at specific stress states, as shown in equation 3.31. For situations in which necking occurs before fracture, the necking strain should be used as the failure criterion.

$$\varepsilon_{\mathrm{eq}}^{n}[\eta] = b\left[\frac{1}{2}\left((g_1 - g_2)^d + g_1^d + g_2^d\right)\right]^{-\frac{1}{p\cdot d}} \tag{3.31}$$

with:

- b as the $\varepsilon_{\mathrm{eq}}^{f}$ at the equibiaxial stress state ($\alpha = 1$) when no necking is percieved.
- p =0.01 as the shape of MK calibration by Pack and Mohr [2017].
- g_1 and g_2 from equation 3.8 and 3.9.
- $\varepsilon_{\mathrm{eq}}^{n}$ as the equivalent plastic necking strain
- d as a calibration parameter, which is implicitly solved in equation 3.32.

$$\left(1 + 2^{d-1}\right)^{\frac{1}{d}} = \sqrt{3}\left(\frac{\varepsilon_{\mathrm{eq-PST}}^{n}}{b}\right)^{-p} \tag{3.32}$$

with:

- $\varepsilon_{\mathrm{eq-PST}}^{n}$ as the equivalent plastic necking strain at plane strain.

This method deletes through-thickness integration points when necking, and elements are deleted when all through-thickness integration points are necking, or the fracture strain is reached for one integration point.

3.6. Proposed Effective Fracture Strain Correction

The proposed method must improve upon the techniques presented in the previous paragraph. This is deemed possible by assuming a non-linear relation between ε_{eq}^{eff}, ε_{eq}^{f}m ε_{eq}^{n}, and t_p/l_e. The method assumes a strain distribution in the neck, and the effect of stress state is considered with neck geometry based on the MK model. A strain distribution is considered instead of homogenizing to enable calculation of ε_{eq}^{eff} for elements smaller than the neck.

The proposed method is based on analytically deriving the first and second principle true strain of a plate that is necking. The effective fracture strain $\varepsilon_{\text{eff}}^{f}$ is obtained with first and second principal true strain at which the plate fractures, represented by ε_1^{f*} and ε_2^{f*}. The third principal true strain ε_3^{f*} is obtained with the conservation of volume (equation 2.1).

The loading is applied with a constant strain path with incrementally increased strain as the shell does not detect necking. The strain is applied to the boundaries with a constant strain ratio α (equation 2.5), which is obtained from the stress state η (equation 2.10) as β can be expressed by α (equation 2.12) assuming plane stress, a constant strain path (α, β, and η are assumed constant), von Mises, and associated flow rule. The plate is assumed to deform as a perfect plate uniformly before through-thickness necking, and afterwards, a necking band is created at an angle ϕ_0 with ε_1. Strain parallel to the band is not localized, while orthogonal to the band, the plastic strain is limited to within the neck.

Figure 4 shows a quarter through-thickness section of a plate orthogonal to the neck. Figure 4.a shows the initial assumed perfect geometry, which is in Figure 4.b stretched uniformly right before necking. Figure 4.c shows the plate strained non-uniformly after necking as all plastic deformation orthogonal to the necking band is limited to within the neck after necking.

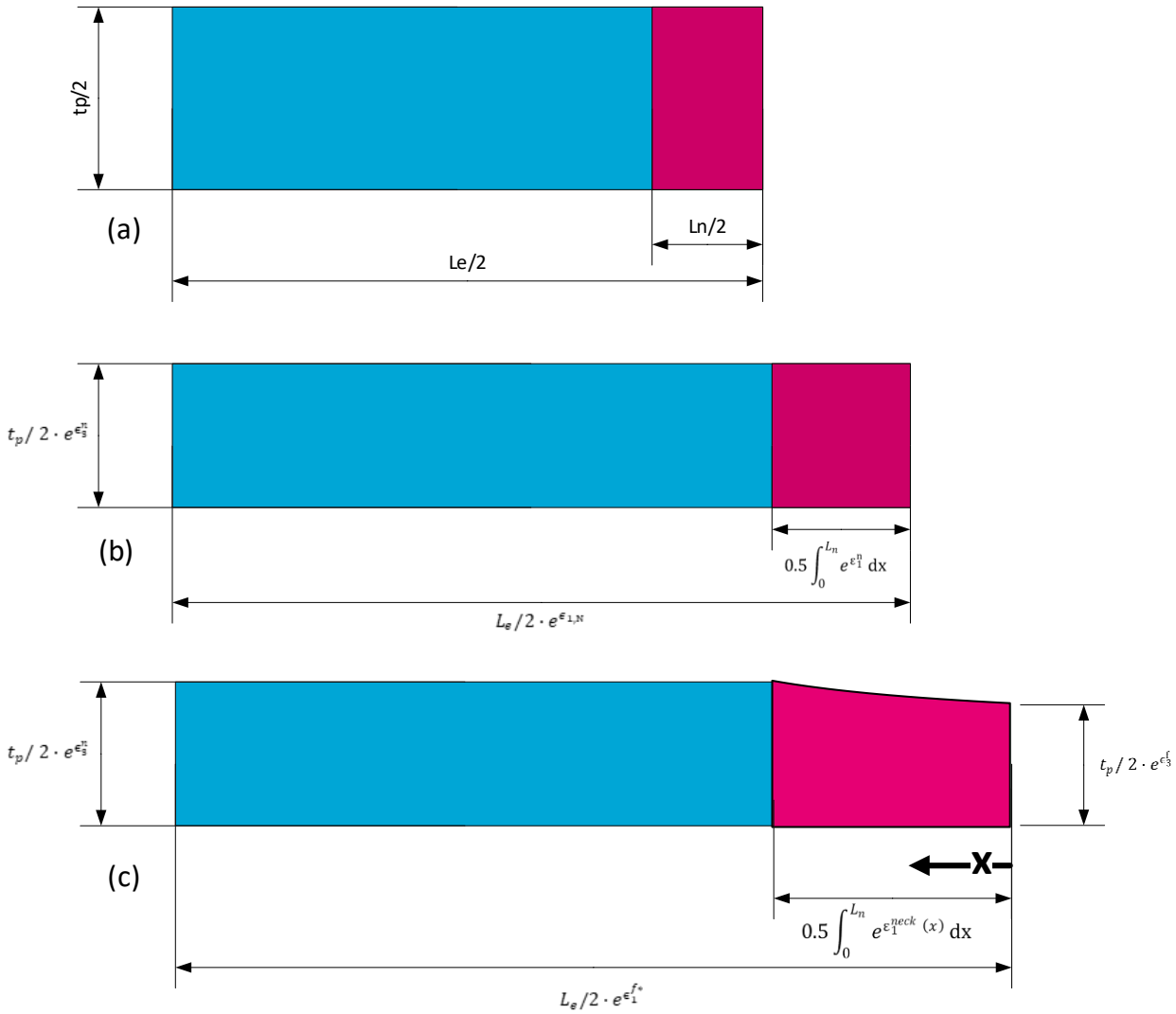

Figure 4 Assumed neck deformation in a quarter of a cross-section orthogonal to the neck

Strain Distribution

The first assumed distribution simplifies the thickness distribution by assuming a linear first principal true strain distribution in equation 3.33, with P and H as constants independent of x.

$$\varepsilon_1^{neck}(x) = Px + H, 0 \le x \le L_n \tag{3.33}$$

with L_n and x as the neck length and distance from the centre of the neck, both normalized by the initial plate thickness and are values before deformation. At the centre of the neck, the fracture strain is assumed and at outside the neck the strain is equal to the necking strain. These assumptions solve H in equation 3.34 and P in equation 3.35.

$$\varepsilon_1^{neck}(0) = \varepsilon_1^f \rightarrow H = \varepsilon_1^f \tag{3.34}$$

$$\varepsilon_1^{neck}(c_1) = \varepsilon_1^n \rightarrow P = \frac{\varepsilon_1^n - \varepsilon_1^f}{L_n} \tag{3.35}$$

With the conservation of volume, the third principal true strain distribution over the thickness becomes equal to equation 3.36.

$$\varepsilon_3(x) = \frac{1}{(1+\varepsilon_2^n)\left(\frac{\varepsilon_1^n - \varepsilon_1^f}{L_n}x + \varepsilon_1^f + 1\right)} - 1, 0 \le x \le L_n \tag{3.36}$$

Effective fracture strain for a neck orthogonal to the first principal strain

The true distribution is not seen by the shell, which only sees global change over the element. The true strain is integrated over the full length of the shell element. This integration is done in two parts in equation 3.37 for inside and outside of the neck. Equation 3.38 is the solution for when the element is smaller than the neck.

$$\varepsilon_1^{f*} = ln(\frac{L_x^{new}}{L_{el}}) = ln(\frac{\int_0^{L_n} e^{\varepsilon_1^{neck}}\,dx + \int_{L_n}^{L_{el}} e^{\varepsilon_1^n}\,dx}{L_{el}}) = ln\left(\frac{\frac{L_n}{\varepsilon_1^n - \varepsilon_1^f}\left(e^{\varepsilon_1^n} - e^{\varepsilon_1^f}\right) + e^{\varepsilon_1^n}(L_{el} - L_n)}{L_{el}}\right), L_{el} \ge L_n \tag{3.37}$$

$$\varepsilon_1^{f*} = ln\left(\frac{L_n e^{\varepsilon_1^f}}{(\varepsilon_1^n - \varepsilon_1^f)\cdot L_{el}}\left(e^{\frac{\varepsilon_1^n - \varepsilon_1^f}{L_n}\cdot L_{el}} - 1\right)\right), L_{el} < L_n \tag{3.38}$$

With L_{el} as the undeformed element length normalized by the plate thickness.

The shell is assumed to have a constant strain path with equation 3.39 as it cannot detect necking.

$$\varepsilon_2^{f*} = \varepsilon_1^{f*} \cdot \alpha \tag{3.39}$$

The third principal effective fracture strain observed by the shell is obtained with conservation of volume in equation 3.40.

$$\varepsilon_3^{f*} = \frac{1}{\left(\varepsilon_2^{f*} + 1\right)\left(\varepsilon_1^{f*} + 1\right)} - 1 \tag{3.40}$$

Assuming proportional strains, the effective equivalent plastic fracture strain becomes 3.41.

$$\varepsilon_{eq}^{eff} = \frac{\sqrt{2}}{3}\sqrt{\left(\varepsilon_1^{f*} - \varepsilon_2^{f*}\right)^2 + \left(\varepsilon_2^{f*} - \varepsilon_3^{f*}\right)^2 + \left(\varepsilon_3^{f*} - \varepsilon_1^{f*}\right)^2} \tag{3.41}$$

Effective fracture strain for other Neck Orientations

The previous equation for ε_{eq}^{eff} is for a neck orthogonal to ε_1, but for stress states between the uni-axial and plane strain stress, this is not the case (Hill, 1952). The angle ϕ_0 is used to express the angle between ε_1 and the necking band orientation. The same linear distribution is assumed as in equation 3.33 but in a different orientation. The distribution is corrected for the neck orientation with the rotation matrix and its transpose in equation 3.42, 3.43, and 3.44.

$$\varepsilon_{x-eng}^{\phi_0} = e^{\varepsilon_2^{f*}} cos^2(\phi_0) + e^{\varepsilon_1^{f*}} sin^2(\phi_0) + \gamma_{12} sin(\phi_0) cos(\phi_0) - 1 \tag{3.42}$$

$$\varepsilon_{y-eng}^{\phi_0} = e^{\varepsilon_2^{f*}} sin^2(\phi_0) + e^{\varepsilon_1^{f*}} cos^2(\phi_0) - \gamma_{12} sin(\phi_0) cos(\phi_0) - 1 \tag{3.43}$$

$$\gamma_{xy-eng}^{\phi_0} = 2\left(e^{\varepsilon_1^{f*}} - e^{\varepsilon_2^{f*}}\right) sin(\phi_0) cos(\phi_0) + \gamma_{12}\left(sin^2(\phi_0) - cos^2(\phi_0)\right) - 1 \tag{3.44}$$

with $\varepsilon_x^{\phi_0}, \varepsilon_y^{\phi_0}$ as the average strains perpendicular to and along the neck, respectively. The shear strain in the neck and global coordinates is expressed with $\gamma_{xy}^{\phi_0}$ and γ_{12} respectively, with $\gamma_{12} = 0$.

The new length orthogonal to the neck is equal to equation 3.45.

$$L_x^{new} = \int_{L_n}^{\frac{L_{el}}{sin(\phi_0)}} e^{\varepsilon_x^n}\, dx + \int_0^{L_n} e^{\varepsilon_x^{neck}}\, dx = \int_0^{\frac{L_{el}}{sin(\phi_0)}} e^{\varepsilon_x^{total}}\, dx \tag{3.45}$$

Equation 3.45 is solved with equations 3.33, 3.39, and 3.42, which results in equation 3.46, and is integrated to 3.47 for an implicit solution of ε_1^{f*}.

$$\begin{aligned}
&\int_{L_n}^{\frac{L_{el}}{sin(\phi_0)}} \left(e^{\alpha\varepsilon_1^n} cos^2(\phi_0) + e^{\varepsilon_1^n} sin^2(\phi_0)\right) dx + \int_0^{L_n} \left(e^{(Px+H)\alpha} cos^2(\phi_0) + e^{(Px+H)} sin^2(\phi_0)\right) dx = \\
&\qquad \int_0^{\frac{L_{el}}{sin(\phi_0)}} \left(e^{\alpha\varepsilon_1^{f*}} cos^2(\phi_0) + e^{\varepsilon_1^{f*}} sin^2(\phi_0)\right) dx \qquad (3.46) \\
&\left(\frac{L_{el}}{sin(\phi_0)} - L_n\right)\left(e^{\alpha\varepsilon_1^n} cos^2(\phi_0) + e^{\varepsilon_1^n} sin^2(\phi_0)\right) + \\
&\left(\left(\frac{1}{\alpha P} e^{\alpha(PL_n+H)} cos^2(\phi_0) + \frac{1}{P} e^{(PL_n+H)} sin^2(\phi_0)\right) - \left(\frac{1}{\alpha P} e^{\alpha H} cos^2(\phi_0) + \frac{1}{P} e^{H} sin^2(\phi_0)\right)\right) = \\
&\qquad \frac{L_{el}}{sin(\phi_0)}\left(e^{\alpha\varepsilon_1^{f*}} cos^2(\phi_0) + e^{\varepsilon_1^{f*}} sin^2(\phi_0)\right) \qquad (3.47)
\end{aligned}$$

The effective fracture strain is found by solving ε_1^{f*} from equation 3.47 with $\alpha, \varepsilon_1^f, \varepsilon_1^n, c_1, \phi_0$ known, ε_2^{f*} from equation 3.39, and ε_{eq}^{eff} from equation 3.41. This method only applies for stress states at which through-thickness necking precedes fracture, as otherwise $\varepsilon_{eq}^{eff}(\eta) = \varepsilon_{eq}^{f}(\eta)$.

Equation 3.47 is recommended for solving ε_1^{f*} for $\phi_0 \neq \pi/2$. However, solvers can be avoided when one uses equation 3.37 or equation 3.38 and neglect the neck orientation in exchange for a small error. This error can be reduced by using ε_1^{f*} from the previous method but solving equation 3.47 with a 1st order Taylor polynomial estimate for the exponent nearby the initial assessment, resulting in equation 3.48.

$$\varepsilon_{1-new}^{f*} = \frac{\mathrm{e}^{\alpha\varepsilon_1^{f*}}\cos^2(\phi)\,\alpha\varepsilon_1^{f*} + \mathrm{e}^{\varepsilon_1^{f*}}\sin^2(\phi)\,\varepsilon_1^{f*} - \mathrm{e}^{\alpha\varepsilon_1^{f*}}\cos^2(\phi) - \sin^2(\phi)\,\mathrm{e}^{\varepsilon_1^{f*}} + \varepsilon_{x-eng}^{\phi_0} + 1}{\alpha\cos^2(\phi)\,\mathrm{e}^{\varepsilon_1^{f*}\alpha} + \sin^2(\phi)\,\mathrm{e}^{\varepsilon_1^{f*}}} \tag{3.48}$$

With $\varepsilon_{x-eng}^{\phi_0}$ from equation 3.49.

$$\varepsilon_{x-eng}^{\phi_0} = \frac{sin(\phi_0)}{L_{el}}\left(\begin{array}{c}\left(\frac{L_{el}}{sin(\phi_0)} - L_n\right)\left(e^{\alpha\varepsilon_1^n}cos^2(\phi_0) + e^{\varepsilon_1^n}sin^2(\phi_0)\right) + \\ \left(\frac{1}{\alpha P}e^{\alpha(PL_n+H)}cos^2(\phi_0) + \frac{1}{P}e^{(PL_n+H)}sin^2(\phi_0)\right) - \left(\frac{1}{\alpha P}e^{\alpha H}cos^2(\phi_0) + \frac{1}{P}e^{H}sin^2(\phi_0)\right)\end{array}\right) - 1 \tag{3.49}$$

These formulas include an error dependent on the difference between ε_1^{f*} and ε_{1-new}^{f*}, and is estimated to be relatively small, but when more accuracy is desired, a higher-order Taylor polynomial could be used for estimation of the exponential function.

Neck Rotation

The method that is presented assumes a neck with an angle ϕ_0 between the first principal and the neck, but this is the initial orientation with the lowest strain that causes necking. This means that the orientation at necking initiation ϕ_n in equation 3.50 might be more accurate. This difference is assumed negligible further in the thesis.

$$\phi_\mathrm{n} = \tan^{-1}\left(\tan(\phi_0)\frac{e^{\varepsilon_1^n}}{e^{\varepsilon_2^n}}\right) = \tan^{-1}\left(\tan(\phi_0)\,e^{\varepsilon_1^n(1-\alpha)}\right), for\ \phi_0 \neq 90° \tag{3.50}$$

Neck length

The proposed method requires only one calibration parameter L_n. This parameter is explicitly solved from equation 3.40 and 3.41 to equation 3.57 and 3.58 for elements smaller and larger than the neck, respectively. These equations assume that the neckband is orthogonal to ε_1 ($\phi_0 = 90°$).

The effective fracture strain is obtained by measuring an initial length L_{el} between two points and measuring the change in length after fracture. This length is measured with crosses painted on the surface in the longitudinal direction of a tensile specimen. The first principal strain on the surface is assumed constant through the thickness due to the plane stress assumption. The crosses allow for measuring from the centre of each point before and after deformation of the test specimen.

The explicit solution of L_n is obtained by reordering equation 3.37 to equation 3.51, simplifying the equation to 3.52 with the LambertW function, reordering the function as a solution of P in equation 3.53, and using the definition of P to form equation 3.54 for the explicit solution of L_n. For elements larger than the neck the explicit solution of L_n only requires reordering equation 3.38 to equation 3.55.

$$-\left(PL_{el}e^{\varepsilon_1^{f*}} + e^{\varepsilon_1^f}\right)e^{-\left(PL_{el}e^{\varepsilon_1^{f*}} + e^{\varepsilon_1^f}\right)} = -e^{\left(-\varepsilon_1^{f*} + \varepsilon_1^f - e^{\varepsilon_1^f - \varepsilon_1^{f*}}\right)} \tag{3.51}$$

with:

- ε_1^{f*} as the first principal true fracture strain of a shell element with shell element length L_{el} divided by its plate thickness of a simulation of an experiment.
- $\varepsilon_{1,\mathrm{N}}$ and $\varepsilon_{1,\mathrm{F}}$ as the first principal true necking and fracture strain of the experiment.
- The LambertW function is a solution of w for an input z of equation $we^w = z$.
- A as defined in equation 3.35.

$$-\left(PL_{el}e^{\varepsilon_1^{f*}} + e^{\varepsilon_1^{f}}\right) = Lambert\mathrm{W}\left(-e^{\left(-\varepsilon_1^{f*}+\varepsilon_1^{f}-e^{\varepsilon_1^{f}-\varepsilon_1^{f*}}\right)}\right) \tag{3.52}$$

With the LambertW function is a solution of w for an input z of $we^w = z$.

$$P = -\frac{e^{\varepsilon_1^{f}} + Lambert\mathrm{W}\left(-e^{\left(-\varepsilon_1^{f*}+\varepsilon_1^{f}-e^{\varepsilon_1^{f}-\varepsilon_1^{f*}}\right)}\right)}{L_{el}e^{\varepsilon_1^{f*}}} \tag{3.53}$$

$$L_n = \frac{L_{el}e^{\varepsilon_1^{f*}}}{e^{\varepsilon_1^{f}} + e^{\varepsilon_1^{f*}}Lambert\mathrm{W}\left(-e^{\left(-\varepsilon_1^{f*}+\varepsilon_1^{f}-e^{\varepsilon_1^{f}-\varepsilon_1^{f*}}\right)}\right)}\left(\varepsilon_1^{f} - \varepsilon_1^{n}\right), L_{el} \le L_n \tag{3.54}$$

$$L_n = \frac{L_{el}\left(e^{\varepsilon_1^{n}} - e^{\varepsilon_1^{f*}}\right)}{\left(\varepsilon_1^{f} - \varepsilon_1^{n} + 1\right)e^{\varepsilon_1^{n}} - e^{\varepsilon_1^{f}}}\left(\varepsilon_1^{f} - \varepsilon_1^{n}\right), L_{el} > L_n \tag{3.55}$$

3.7. Conclusion

This chapter aimed to answer the second research question:

"*How do fracture strains in solids translate to effective fracture strains in shells smaller than five times the plate thickness?*". This is done in Paragraph 3.6 by estimating the shape of a neck and how a shell would interpret it in terms of effective first principal true fracture strain ε_1^{f*} in equation 3.40 and 3.41. Alternative methods that calculate the effect of the neck are presented in Paragraph 3.5. These methods use a relation of the necking, fracture and effective fracture strain, which is non-linearly (Walters, 2014; Bijleveld et al., 2018) dependent on the element size. These relations require the fracture and necking strain for which FFLD (Paragraph 3.2) and Forming limit Diagram (FLD) (Paragraph 3.4) are presented, respectively. As a comparison to the multi-axial data given in 3.2 and 3.4, the simplified failure criteria by classification institutes are given in Paragraph 3.5.

The novelty in this chapter is a method for determining the neck width in equation 3.54 and equation 3.55, a method for predicting the effective fracture strain for smaller elements in equation 3.37 and 3.38 and introducing the effect of neckband orientation on the effective fracture strain.

4 Necking Model Description

4.1. Introduction

This chapter aims to partially answer the first research question:
"*How can the accuracy of stress state dependent ductile fracture prediction models for shell elements be evaluated?*".

For this evaluation, a benchmark is required that delivers $\varepsilon_{\mathrm{eff}}^{f}$ for different shell element sizes and stress states. Usually, experiments are the benchmark, but these have limitations to element sizes and stress states. Instead, usage of a FEM model that is calibrated with experiments is proposed. This model must simulate shells that represent a part of a plate and must be able to capture pre- and post-necking behaviour at specific stress states.
This chapter defines two models: one solid element model for capturing the post-necking behaviour until fracture, hereafter called the "solid MK model" and a shell element model to calibrate the geometrical imperfection of the previous model, subsequently the "DSSE model", as one is required to initiate necking. This imperfection is a band over which the plate thickness is locally thinner, based on Marciniak et al. [1973] and the FEM implementation is based on Pack & Mohr [2017].

Outline

This Chapter is built up by explaining the geometry (Paragraph 4.2) and material model (Paragraph 4.3) of the plate that was modelled. This plate is strained as a centre section of an infinite plate with periodic boundary conditions (Paragraph 4.4) that strain the plate as a shell. This strain imposes a constant specific stress state and incrementally increases effective plastic strain until fracture. These boundaries apply a proportional load path for easy calibration of an effective fracture strain forming limit diagram.

4.2. Mesh Geometry

The geometry of the model to determine the FLD is based on the shell model from Pack & Mohr [2017], as shown in Figure 2. The model is a $20t_p$ by $20t_p$ square of composed out of a 21 by 21 mesh of square shells with the thickness equal to the plate thickness, with the exception of a horizontal band with a thickness imperfection f_i. This imperfection was 0.5, 1, and 1.5% difference in plate thickness in separate simulations. For obtaining the FLD for S235 a different mesh geometry is used with $t_p = 6\,mm$.
For predicting fracture, the same plate dimensions are used, but the model is composed out of solids to predict fracture with a stress state dependent fracture locus designed for solids. The locus calibrated in

Bijleveld et al. [2018] with 13 solid elements through the thickness was used. The final model requires a midplane for determining shell strains (otherwise one must be extrapolated) with 12 elements through the thickness. The surface is described by $21 \cdot 13$ solid elements in the width and length with an element in the centre to predict fracture. These specifications result in solid elements that are $20t_p/21/13$ wide and long, and $t_p/13$ high. The thickness imperfection band is applied by scaling nodes along the imperfection band relative to the midplane. This abrupt thickness change is comparable to that of the shell model.
The 12 elements through the thickness are lower than the 12 through the half-thickness, as suggested by Lee [2005]. This change in element length may impact the stresses, fracture locus and the ability to capture post necking behaviour.
The thickness imperfection band is a simple alternative to statistical variation of geometry and material properties. This variation can be justified by 3d optical measurements from Gorji et al. [2016]. The thickness variation of a tensile test specimen with a nominal thickness of 1.05mm is shown in Figure 5. 1% thickness imperfection for a plate of 1.02mm nominal thickness. These measurements make the range of 0.5% to 1.5% thickness imperfection used by Pack & Mohr [2017] realistic.

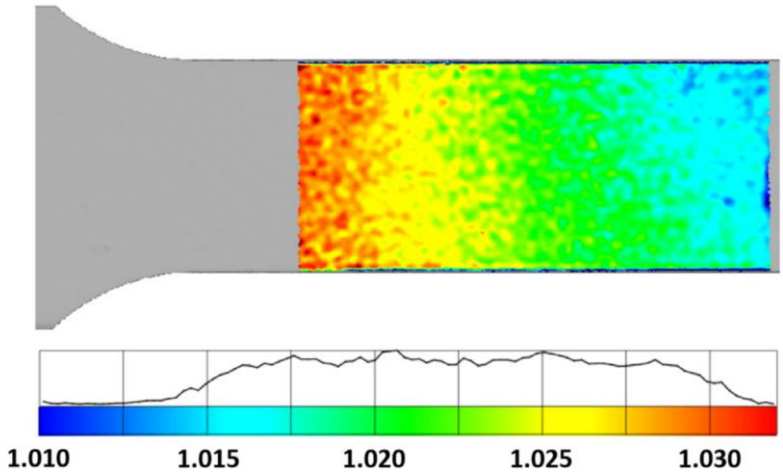

Figure 5 Thickness distribution of the undeformed tensile specimen, captured by an optical 3D measuring device. From Gorji et al. [2016].

4.3. Material Description

The fracture locus and plasticity model for the material considered in this thesis S235JR is as calibrated by Bijleveld et al. [2018]. The plasticity model is obtained by inverse engineering a tensile test with $\bar{\sigma}_{\text{Voce+Swift}}$ hardening model as suggested by Alsos et al. [2008]. The fracture strain is determined through damage growth indicated by a damage parameter D from 0 (initially) to 1 (at fracture), with damage accumulation for proportional loading, with equation 4.1, as proposed by Johnson & Cook [1985].

$$dD = \frac{d\bar{\varepsilon}_p}{\bar{\varepsilon}_p^f[\eta, \bar{\theta}]} \xrightarrow{discretize} \Delta D = \frac{\Delta\bar{\varepsilon}_p}{\bar{\varepsilon}_f(\eta, \bar{\theta})} \tag{4.1}$$

The stress state dependent fracture model is calibrated by reducing the RMSE of damage estimations with load paths containing triaxiality, Lode angle, and effective strain until fracture from multiple tests simulated in solids by Bijleveld et al. [2018]. The calibrated values from the material properties and ductile fracture locus are shown in

Table 3 and Table 2, respectively. Table 2 shows two values for two different calibrations each separated with a comma. The first value is calibrated when assuming $c = 0$, and the latter value assuming $c \neq 0$. The fracture locus is improved by using the uni-axial test that obtained lower fracture strains for calibration instead of the higher strains as during equi-biaxial tests the weakest direction will initiate fracture earlier. The elastic part is modelled with Young's modulus of 216 GPa at 0.2% offset strain, yield strength of 298MPa, and the Poisson ratio of 0.3 as recommended by RP-C208 (Det Norske Veritas, 2013).

Comparison Material

For comparison and verification of the shell model, another material is also simulated: DP from Pack & Mohr [2017]. This model has: $t_p = 1\ mm$, and hardening parameters from table 3 for DP.

Table 2 Calibration parameters of fracture locus from Bijleveld [2018] *and calibrated based on load paths.*

FRACTURE MODEL S235	PARAMETER	VALUE	UNIT
HC	a	0.474, 0.733	-
(STRESS BASED)	b	1241, 962.86	MPa
	c	0, 811E-17	-

Table 3 Calibration parameters of plasticity model S235 from Bijleveld [2018] *and DP from* Pack & Mohr [2017]

MODEL	PARAMETER	VALUE S235	VALUE DP	UNIT
COMBINED	α_{vs}	0.724	0.7	-
SWIFT-VOCE	k_0	0	349.5	MPa
HARDENING	Q	0.0801	536.4	MPa
	β_V	1.16E-13	93.1	-
	K	1102	1315.4	MPa
	ε_0	6.17E-3	0.28E-4	-
	n	0.220	0.146	-

4.4. Boundary conditions

The plate is loaded as a shell with an incremental increase of effective plastic strain while maintaining a specific stress state by controlling the strain ratio α. This assumes a constant strain path and incremental strain increase; both are typically applied to a shell during a crash simulation until fracture. The assumption

of a constant strain path is justified for pre- and post-necking as crash simulation models are not designed to detect necking in shells and will not change the strain or stress ratio after necking.
The strain ratio is imposed on the elements by applying the engineering strain from equation 4.2 and 4.3 to a plate.

$$\varepsilon_{1\mathrm{BC}} = -1 + e^{\frac{\bar{\varepsilon}_p\sqrt{3}}{2\sqrt{\alpha^2-\alpha+1}}} = \lambda_{p1} - 1 \tag{4.2}$$

$$\varepsilon_{2\mathrm{BC}} = -1 + e^{\frac{\bar{\varepsilon}_p\alpha\sqrt{3}}{2\sqrt{\alpha^2-\alpha+1}}} = \lambda_{p2} - 1 \tag{4.3}$$

with:

$$\bar{\varepsilon}_p = \int d\bar{\varepsilon}_p \approx \dot{\bar{\varepsilon}}_p t \tag{4.4}$$

With t as time.
Assuming proportional loading with a constant strain rate $\dot{\bar{\varepsilon}}_p$ and constant strain path.
The rotation of the principal stress coordinate system leads to the following equation 4.5 for imperfection band angle with respect to the main principal strain of $\pi/4 \leq \phi_0 \leq \pi/2$, as proposed by Pack & Mohr [2017]. This matrix shows the deformation gradient as a function of displacement applied at the edges.

$$[\mathbf{F}] = \begin{bmatrix} \frac{u_{n1}}{L} + 1 & \frac{u_{t2}}{L} & 0 \\ \frac{u_{t1}}{L} & \frac{u_{n2}}{L} + 1 & 0 \\ 0 & 0 & \mathrm{F}_{33} \end{bmatrix} \tag{4.5}$$

The displacements of the edges are obtained by the engineering strain in in each direction expressed in equation 4.6, 4.7, and 4.8.

$$F_{11} = \lambda_{p1} sin^2(\phi_0) + \lambda_{p2} cos^2(\phi_0) \tag{4.6}$$

$$F_{22} = \lambda_{p1} cos^2(\phi_0) + \lambda_{p2} sin^2(\phi_0) \tag{4.7}$$

$$F_{12} = F_{21} = \left(\lambda_{p1} - \lambda_{p2}\right) sin(\phi_0) cos(\phi_0) \tag{4.8}$$

The parameters λ_{p1} and λ_{p2} are used as strain histories for convenience in equation 4.9, and 4.10, respectively.

$$\lambda_{p1}[t] = \exp\left(\frac{\sqrt{3}\dot{\bar{\varepsilon}}_p \cdot t}{2\sqrt{(1+\gamma+\gamma^2)}}\right) \tag{4.9}$$

$$\lambda_{p2}[t] = \exp\left(\frac{\sqrt{3} \cdot \alpha \cdot \dot{\bar{\varepsilon}}_p \cdot t}{2\sqrt{(1+\gamma+\gamma^2)}}\right) \tag{4.10}$$

With $\mathbf{F}$ as a deformation gradient, and $\mathrm{F}_{33}$is trivial for the 2D shell model boundary conditions.
$u_{n1}, u_{n2}, u_{t1}, u_{t2}$ are relative displacements as indicated in Figure 2. These are applied to a model with Period Boundary Conditions (PBC). These PBC are applied on shells, and solids for each surface layer of solid elements, but the edge of shell elements are constrained in the z-coordinate/out-of-plane direction. In

contrast, this constraint is only applied at the edge of the midplane in the solid model to allow free thickness deformation.

Virtual Shells

The previously mentioned model is a global-local approach of a shell with $L_{el}/t_p = 20$, but the goal of this model is to derive how the effective fracture strain in shells is dependent on element size over plate thickness ratio L_{el}/t_p and stress state. This effective fracture strain is derived for multiple element sizes by applying on the nodes of a square shell the nodal displacement of four midplane centred nodes of the solid model. The element size varies by taking more outward nodes, resulting in 136 shell elements with an element length, as shown in equation 4.11.

$$L_{el}^{virt} = L_{el}^{solid}(1 + 2N) = \frac{20t_p}{21{\cdot}13}(1 + 2N) \tag{4.11}$$

with:

- L_{el}^{virt} as the virtual element length.
- L_{el}^{solid} as the solid in plane element length.
- N as the number of nodes from the centre element with range $0 \leq N \leq 136$.

Forcing Location of Fracture

In the model that was described here, fracture can occur outside the centre, which is not beneficial for virtual elements that must capture a fractured element. Therefore, the centre element column has 2% thickness imperfection, as illustrated in Figure 6, instead of f_i applied to other elements in the imperfection band to force fracture in the centre.

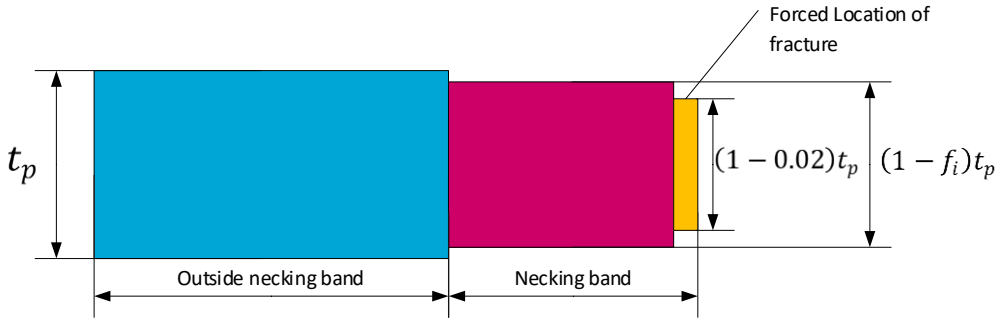

Figure 6 Half cross-section of plate orthogonal to the necking band, indicating thickness variation.

4.5. Conclusion

This chapter aims to answer the first research question partially:

"*How can the accuracy of stress state dependent ductile fracture prediction models for shell elements be evaluated?*".

This question is partially answered by providing a benchmark model that simulates deformation and post-through-thickness necking based on the MK-analysis. With the assumption that a thickness imperfection of 0.5,1,1.5% in a band will induce necking in a plate comparable to what would happen in an experiment. The plate's constraints impose a specific stress state with strains, while also changing the orientation of the first principal stress with respect to the imperfection band. The plate has PBC so that it represents a section of an infinite plate, as intended by the MK-analysis. The geometry and model are based on and validated with Pack & Mohr [2017], while the final shell and solid model uses material parameters for S235 from Bijleveld et al. [2018] and Haag et al. [2017]. The shell version of the model is used for calibration of imperfection size and orientation of the necking band. This shell model is extended with solids to accurately model post necking plastic flow, based on that the material model calibrated for the used element size in a simulation a tensile test. Midplane nodal displacements are used in combination with virtual shells to determine how the effective fracture forming limit diagram (EFFLD) changes with element size. Fracture is forced in the centre of the plate by an extra imperfection.

5 Model Calibration

5.1. Introduction

This chapter aims to partially answer the first research question:

"*How can the accuracy of stress state dependent ductile fracture prediction models for shell elements be evaluated?*".

This accuracy is evaluated using a solid element model calibrated by a shell model as defined in the previous chapter. This chapter explains the calibration procedure of two calibration parameters, thickness imperfection, and the angle between the band and the first principle stress for each stress state.

Outline

The calibration procedure starts with calibrating the necking curve, by first determining when the plate is determined to neck (Paragraph 5.2). For necking to occur, the plate must contain an imperfection. The effect of a thickness imperfection and imperfection orientation is explored, and the correct imperfection is determined for each stress state (Paragraph 5.3). The model is compared to the results of Pack & Mohr [2017] for model validation and comparing the FLD of two comparable metals DP and S235. For each model, the minimum failure strain at each stress state represents points of the FLD, and that orientation is simulated with solids for each stress state.

5.2. Imperfection Band orientation and size

MK models are highly dependent on orientation and imperfection size and require calibration. This calibration is performed by using the lowest necking strains of all imperfection orientations to create an FLD for each separate imperfection size. A conservative FLD is chosen based on experiments, for example the current material, S235, did not neck in equi-biaxial stress state and thus an FLD is chosen that intersects the FFLD at that stress state. The assumption is that through-thickness necking and fracture coincides at that point, as suggested by Pack & Mohr [2017] as a conservative estimate. The model is in this paragraph compared to findings from Pack and Mohr, and a conventional MK analysis.

Analytical Band Orientation

In Marciniak et al. [1973], it was proposed that through-thickness localisation can be caused by material or geometrical defects, which could be described by a thickness imperfection band with an angle ϕ_0 between the main principal strain ε_1 and the band, as indicated in Figure 2. This angle is analytically obtained by Hill [1952] in equation 3.12 for $\alpha < 0$ and is otherwise $90°$.

Model Validation

Necking is assumed to occur at the band orientation that leads to the minimum necking strain according to equation 3.24 for that stress state. Therefore, multiple band orientations are simulated, and the true necking strain is assumed to be the minimum necking strain of all of them. This true necking strain obtained from the shell element plate model is compared to the true necking strain obtained from the solid plate model. This comparison is made to see if DSSE is a good approximation for the much more complicated analysis for the solid element plate model.

The model from Pack & Mohr [2017] is compared to the models with either Linear Boundary Conditions (LBC) or Periodic Boundary Conditions (PBC) to model the plate as a part of an infinite plate. The necking strain of each band orientation and stress state for DP steel as reference material is shown in Figure 7 and Figure 8 for PBC and LBC, respectively. The Hill angle mentioned in these figures is from equation 3.16 for $\alpha < 0$, and otherwise 90^o. Theoretically this is the band orientation that initiates the lowest necking strain for a plate without imperfection, but the model has an imperfection, causing earlier necking initiation for band orientation closer to 90^o. Therefore, additional orientations are simulated with increments of one degree, indicated Hill angle + N_2 with N_2 as the increment in degrees. As a reference, the fracture locus, denoted as 'HC fracture strain', is shown as calibrated by Pack and Mohr [2017]. The correctness of the model is determined by the degree of similarity with the fit FLD by Pack & Mohr [2017], denoted as 'DSSE Pack and Mohr' in the figures. Both models are approximations, as the goal is to simulate a shell element within a plate with unknown dimensions and constraints. This situation is not simulated with the LBC model nor by the PBC model. Still, the PBC model is assessed in the following sections, as it is considered as the most representative constraint scenario.

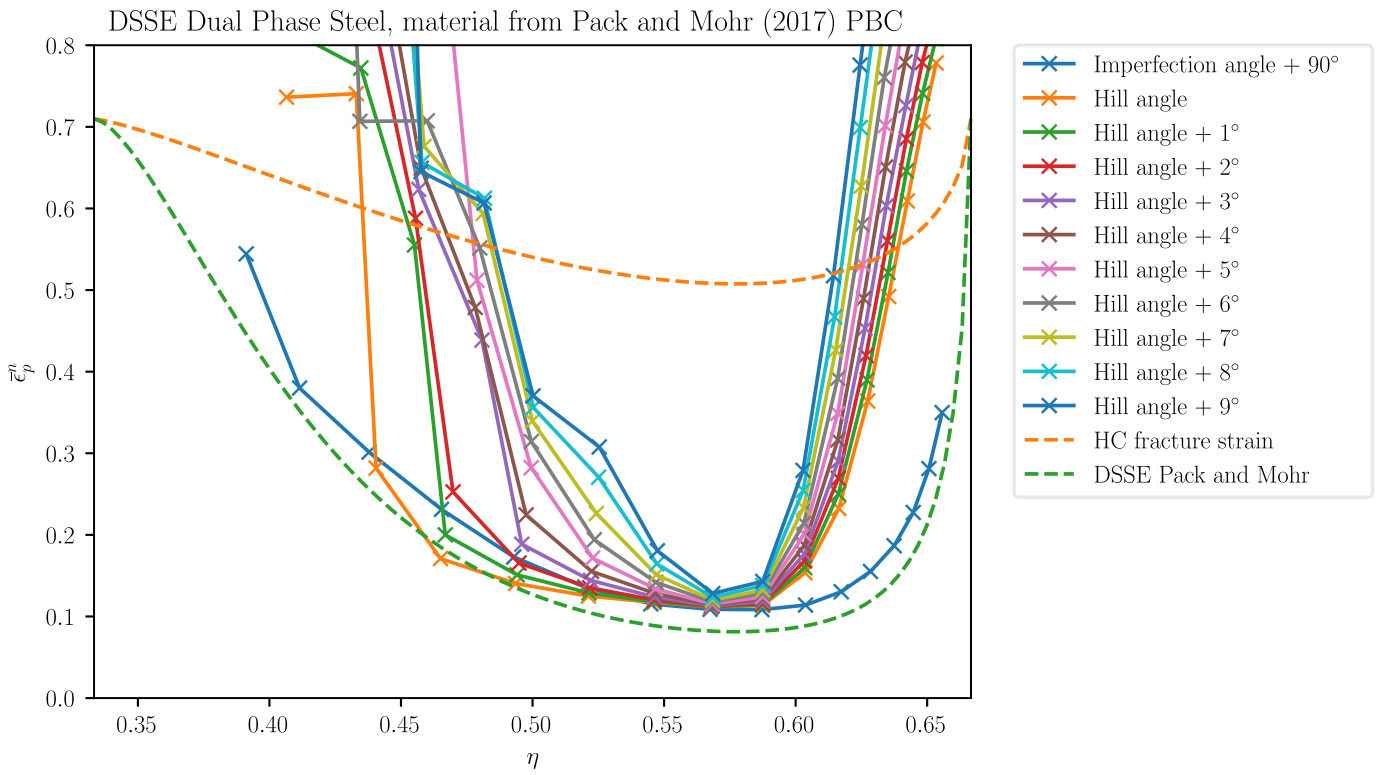

Figure 7 PBC DSSE DP with different imperfection angles

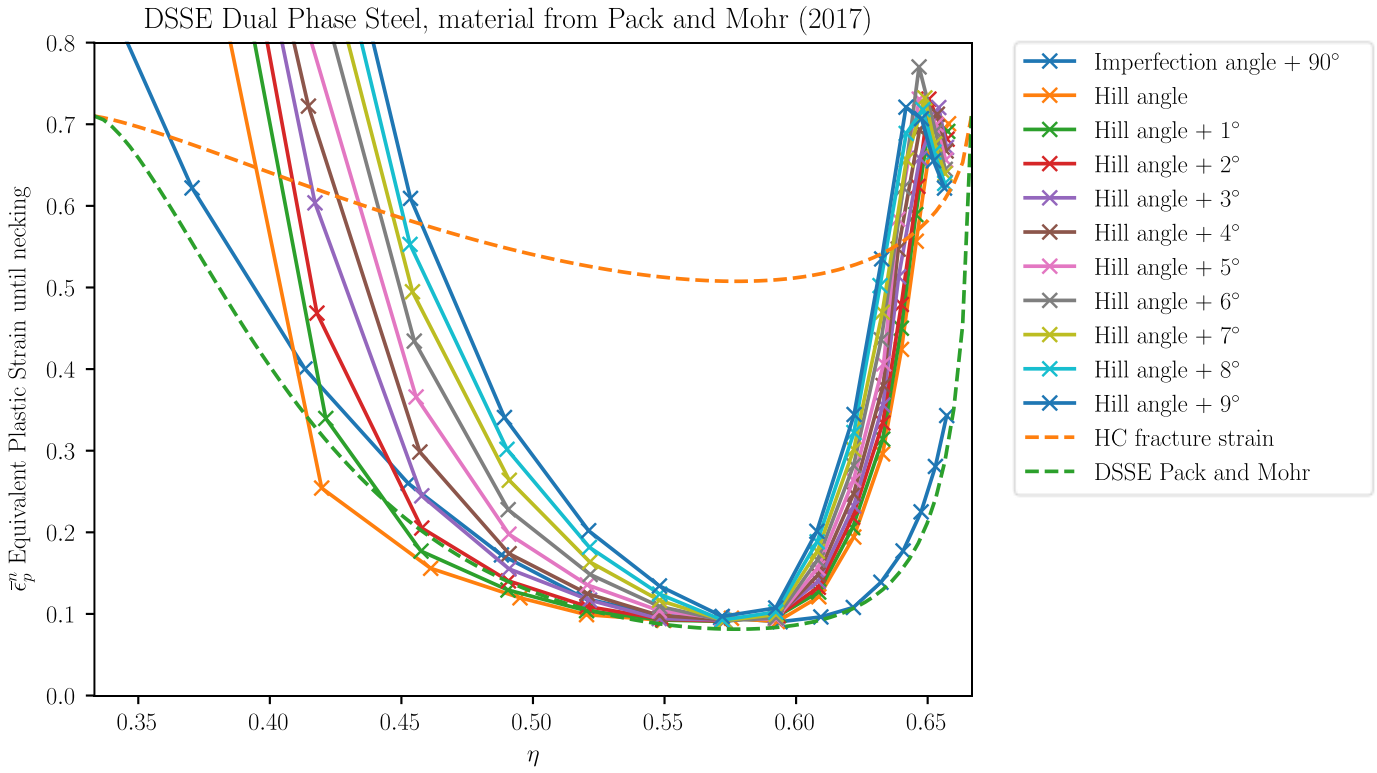

Figure 8 LBC DSSE DP with different imperfection angles

Analysis

The calibration procedure is repeated with S235JR and material parameters as calibrated by Bijleveld [2018]. An alternative model with PBC is also simulated at 90 different imperfection band orientations to show that there is no other orientation that will cause necking earlier. For clarity, every fifth neck band orientation angle in degrees is labelled with "ϕ = $angle$" and coloured, while others are coloured light grey. This FLD is shown in Figure 9 and Figure 10 for the PBC and LBC model, respectively.

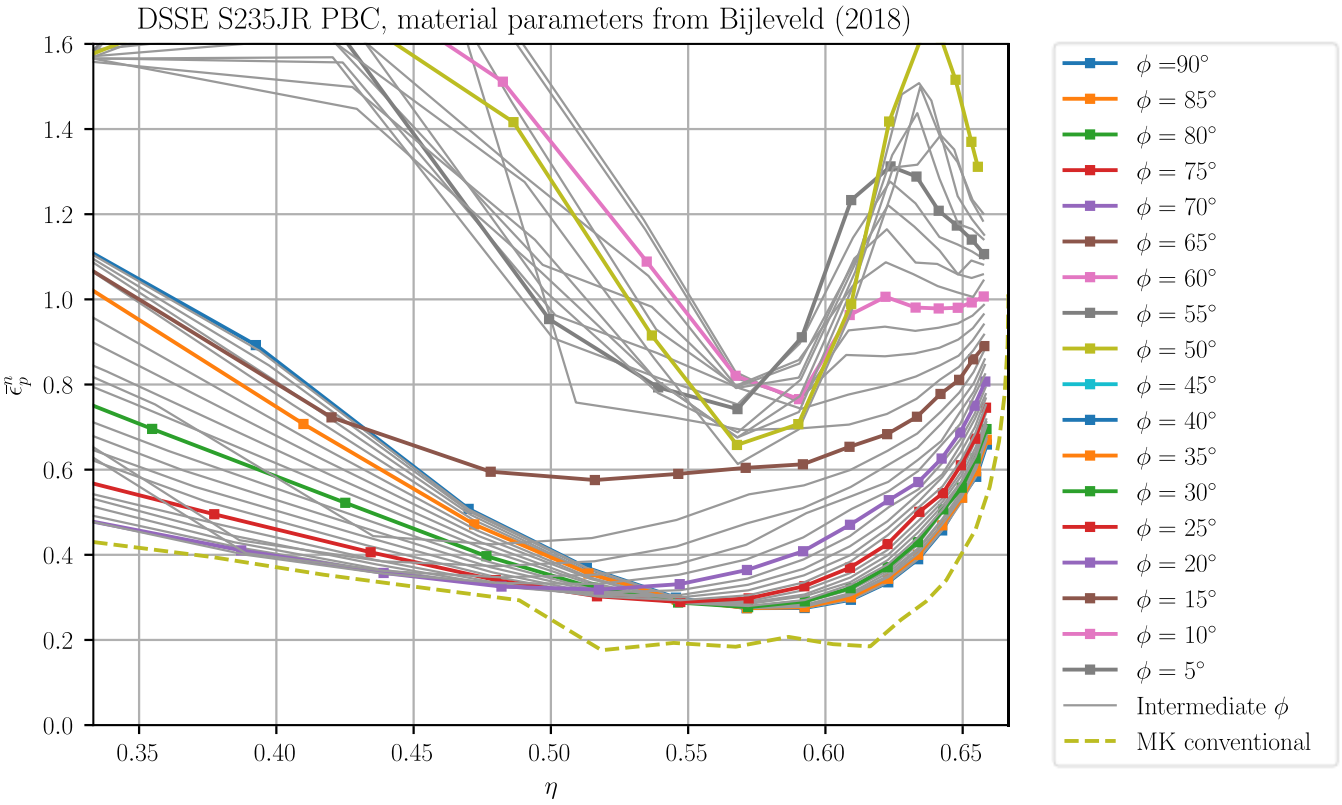

Figure 9 PBC DSSE S235JR with different imperfection band angles

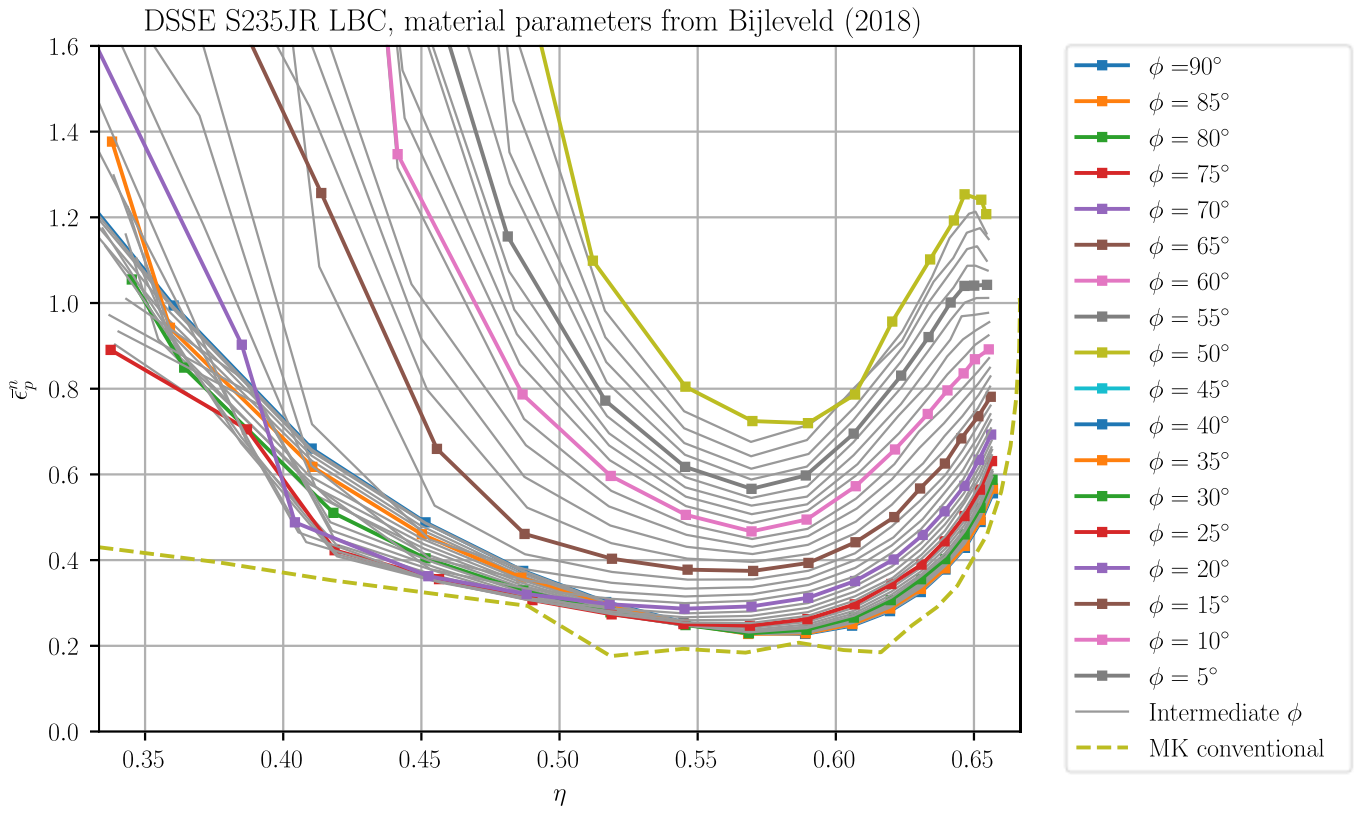

Figure 10 LBC DSSE S235JR with different imperfection band angles

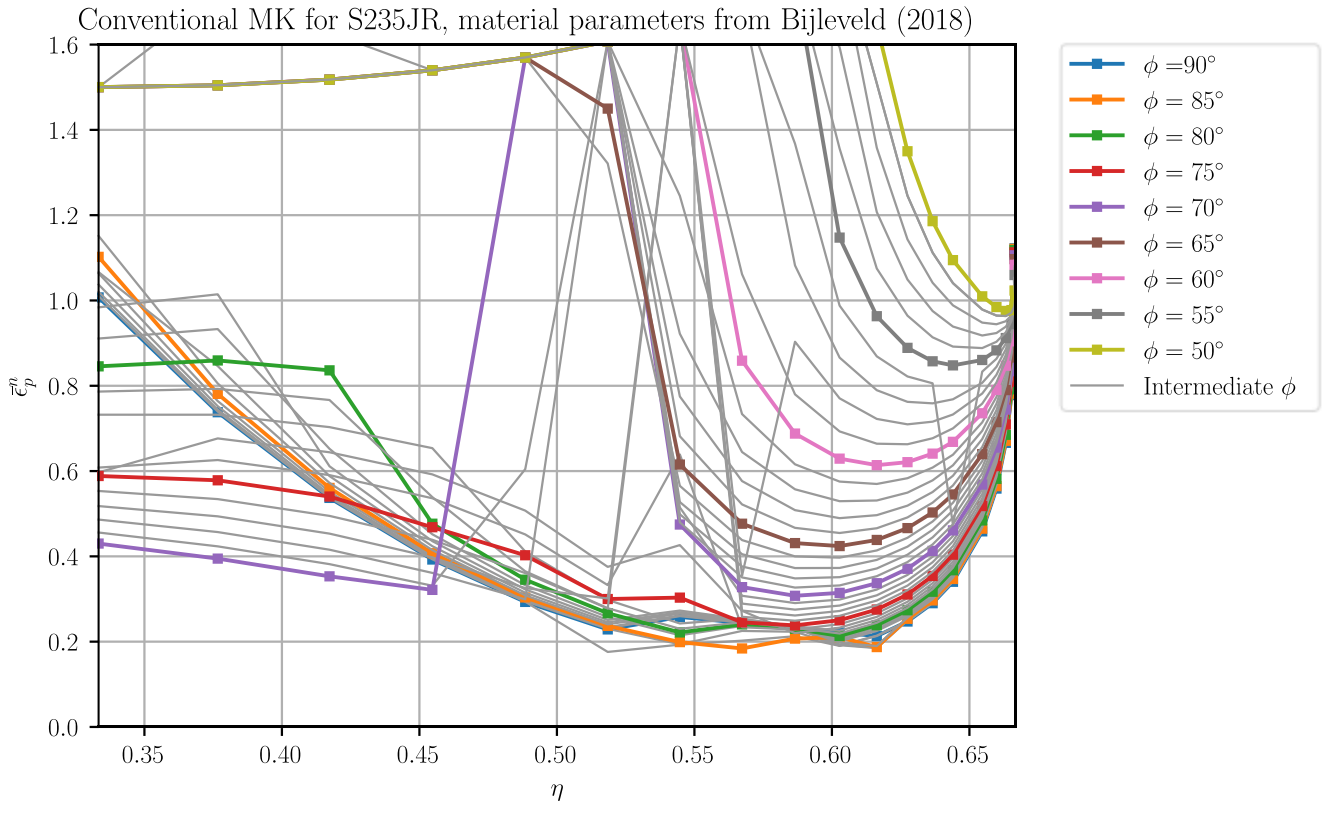

Figure 11 Conventional MK for S235JR with different imperfection angles

The necking strain for each band orientation and stress state from the conventional MK analysis is shown in Figure 11 for comparison, which is based on Safikhani et al. [2009]. For clarity, every fifth neck band angle with the first principle strain in degrees is labelled with "$\phi = angle$" and coloured, while others are coloured light grey

The conventional model is unstable in the plane strain stress state but can still function as a reference for other stress states during calibration. Therefore, the results of the conventional method are interpolated when necking occurs at almost no plastic strain. Two weaknesses in this model are, the plane stress assumption, and it only analyses a cross-section perpendicular to the neck band. The weakest orientation for different strain ratios is shown in Table 4, together with the orientation from Hill's criterion.

Table 4 Imperfection band orientation with respect to the first principal stress for S235JR with 1% thickness imperfection

	LOWEST FLD ϕ FOR MK			
ALPHA	Hill°	CONV°	LBC°	PBC°
-0.50	63	70	75	50
-0.43	67	70	72	69
-0.37	70	70	73	69
-0.30	73	90	73	69
-0.23	77	89	74	71
-0.17	81	89	76	74
-0.10	84	85	77	78
-0.03	88	85	83	90
0.03	90	89	89	90
0.10	90	87	90	90

By comparing the PBC and LBC model, the third research question "*What are the effects of boundary conditions on through-thickness necking?"* is answered.

The PBC model, compared to the LBC model agrees more with the conventional model in uni-axial to plane strain stress state, while between plane strain and equi-biaxial stress state, it is the other way around. The imperfection band orientations for $-0.5 \leq \alpha \leq 0.1$ vary for all three models. The PBC model is, in theory, a part of an infinite plate, as suggested by MK-analysis. At the same time, the LBC uses exact displacements as would be applied on a plate with the exact dimensions.

The LBC boundary conditions force the strain ratio over the boundary conditions which may in case of a slight neck concentration relatively more compression at the edges of the neck when compared to the edges outside of the neck. These edge constraints may cause a more uni-axial stress state locally for uni-axial ($\eta = 0.33$) to plane strain stress state ($\eta = 0.58$) and may increase necking strain.

For the PBC, LBC, and conventional MK models, the models with band orientations $\phi_0 > \pi/2$ are mirrored

versions of the models with a necking band orientation of $\phi_{equivalent} = \pi - \phi_0$. The main difference is that the first and second principle strains are switched, increasing the necking strain. In general, necking strains were higher, as in not within the plot limits for when $\phi_0 > \pi/2$, but this was expected, and the relevant orientations are nearby those expected by Hill in equation 3.12.

5.4. Conclusion

This chapter aims to partially answer the first research question: "*How can the accuracy of stress state dependent ductile fracture prediction models for shell elements be evaluated?*", which is done by calibrating the model with the results from Pack and Mohr [2017]. Based on the results, the PBC model seems to be used by Pack and Mohr [2017] and is used for future analysis as it is meant to model a part of an infinite plate. The one percent imperfection results in specific neck orientations Table 5, which are used for the solid MK model.

6 Performance of Failure Criteria

6.1. Introduction

The model described in the previous chapters is designed to capture post-through-thickness necking, fracture, and the failure criteria presented in Chapter 3 are compared with results from this model. This chapter answers the first research sub question: "*How can the accuracy of stress state dependent ductile fracture prediction models for shell elements be evaluated?*".

This question is answered by assessing methods to predict the effective fracture strain, from Chapter 3, in terms of deviation from the effective fracture strain that is found from the solid model described and calibrated in Chapter 4 and 5, respectively. The error is normalized for fair comparison in accuracy over element size and stress state with Normalized Absolute Error (NAE) in equation 6.1.

$$\mathrm{NAE} = \frac{1}{n}\sum_{i=1}^{n}\left|\frac{f_i - y_i}{f_i}\right| \tag{6.1}$$

With:

- f_i, as the results from a higher accuracy method, in this case, the results from the solid element plate model.
- y_i, as the results from a shell element method.
- n, as the number of values evaluated.

Outline

Before analysing the results from the PBC solid model, expectations are stated (Paragraph 6.2.) for analysing deviations and their causation. The first result from this analysis is the performance of conventional failure criteria (Paragraph 6.3.), together with the calibrated FLD using shells. Deviations of FLD are assessed together with the previously mentioned calibration criterion (Paragraph 6.4.). With this, the EFFLD correction methods for shells are considered (Paragraph 6.5 and Paragraph 6.6). With the importance of FLD considered, more variations of the FLD are assessed (Paragraph 6.7.). With this information, conclusions are made (Paragraph 6.8.)

6.2. Expectations

The model, as described, will have deviations from experiments and between solid and shell element models. These are explained in this paragraph.

Deviation between models and experiments:

The model considers an imperfection band with the orientation that causes necking at the lowest strain, together with an extra imperfection in the centre to force failure in the centre. These assumptions are conservative and will cause failure earlier in the model than experiments, but both are justified to model thickness inhomogeneity of plates.

The initial assumptions of fracture prediction are:

- The type of fracture is ductile and describable by phenomenological models such as HC and MMC.
- Strain localisation by through-thickness necking is not entirely captured by shells (Dunand & Mohr, 2010), and effective fracture strain requires a correction based on the through-thickness necking strain unless necking doesn't precede fracture.
- The fracture locus for shells is different than solids, as the shell element assume plane stress and cannot capture through thickness strain localisation.
- The amount of the neck is captured within a neck depends on the l_e/t_p ratio, as suggested by Ehlers et al. [2008] as Scharrer et al. [2002] found that the neck was proportional to the necking strain.

6.3. Conventional Failure Criteria

The resulting effective plastic strain to fracture of midplane virtual elements is displayed in Figure 12 together with conventional failure for details on the failure criteria, see Chapter 3.

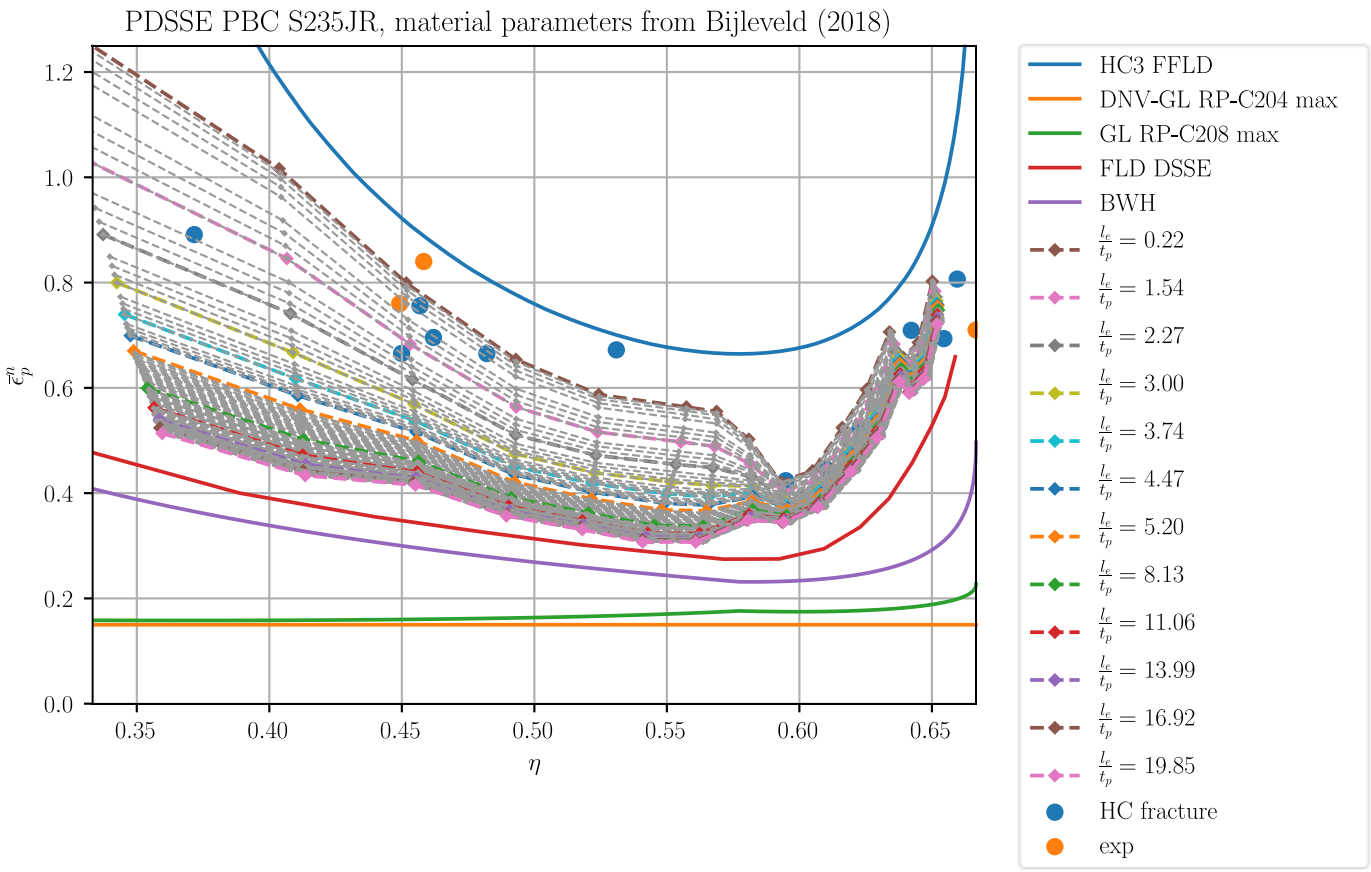

Figure 12 Effective plastic strain until fracture at different element sizes

In Figure 15, the first labelled failure criteria for shell elements are the maximum fracture strains from RP-C204 and RP-C208, as the minimum element size is $5t_p$. As a lower bound of failure criterium is when necking precedes fracture, the FLD is therefore also displayed in Figure 12. The two variants displayed are FLD from the DSSE shell model and the BWH FLD. The model is deemed fractured when a solid element is fractured according to the HC fracture locus, labelled as the HC3 FFLD, with the number indicating the number of calibration parameters used. The strain at which the solid element failed in each plate model is labelled as “HC fracture” at the average stress state of the failed element. As the FFLD and material parameters are fit from experiments, a link is required to those original experiments. This is done by displaying the measured fracture strains and average stress state of three experiments with the material used in the model, labelled as exp. The first two experiments are uni-axial tensile experiments performed by Haag et al. [2017], and strains were measured with a calliper based on area reduction in thickness and width direction. The average is shown for the average of three tested parallel and orthogonal to the rolling direction. The third experiment is an equi-biaxial punch test from Bijleveld [2018] was cut from the same plate as the tensile tests and the fracture strain was measured will a ball point micrometer. The results from

the smallest element size of $l_e/t_p = 0.073$ are omitted as at that location plane stress is not applicable and different stress states are observed than applied externally.

For $\eta \leq 0.577$, the second principle strain is negative, and strain is applied on the edges with displacement. This causes reduced strain ratios outside the neck after necking, which will cause compression when $\alpha \leq -0.5$ changing the stress state outside of the neck towards to pure shear $\eta = 0$. This is seen in Figure 15 for $\eta < 0.45$ by the triaxiality being a function of element length.

At $\eta \approx 0.45$ a dip is seen in convergence of lines representing the EFFLD in Figure 12. This discontinuity is caused by the discontinuity in the necking strain, which could be something physical or an error. The source of this error could be that the model did not detect necking initiation due to the implicit formulation even though arc length control is applied to prevent this.

Figure 12 illustrates the difference in fracture for shell and solid elements, which is that the shell element is not limited by plate thickness in size but cannot capture the through-thickness localisation inside the element. This is best seen for the uni-axial stress states to equi-biaxial stress states ($0.47 \leq \eta \leq 0.67$), as the fracture strains of shell elements are close to the failed solid element. This means that there is a small difference between necking and fracture strain, and the fracture strains for the solids are lower than for plane stress. In the uni-axial stress state to the plane strain state, the difference between effective fracture strain is relatively larger. This is caused by a larger difference between necking and fracture strain, and the neck orientation, which causes instability earlier. Still, strains are less localised than when the neck is perpendicular to the main principal strain.

The FFLD calibrated with solid element models of experiments cannot be used directly to predict fracture in shell elements.

Figure 12 shows that the effective fracture strain converges for increasing shell element size to an FLD, which is different from BWH or the DSSE method, but the latter comes closer to it. This is probably caused by the fact that solid elements can describe through-thickness stress variations, and smaller elements may smoothen variations stress, preventing instability at lower strains. Also, the imperfection is less abrupt for the solid element after deformation in the solid model and may prevent earlier strain localisation.

The EFFLD can be described more as a continuous curve between $2.27 \leq l_e/t_p \leq 5.20$ for larger or smaller element lengths outside of this range the EFFLD becomes more discontinuous. The point at which the EFFLD becomes discontinuous is plane strain at which also the orientation of the neck changes from a function of η for $\eta < 0.58$ (plane strain) to 90° for $\eta \geq 0.58$.

FLD and FFLD as Failure Criteria

To start, conventional methods to predict failure in shell elements such as FFLD and FLD are compared to $\varepsilon_{\mathrm{eff}}^{f}$ from the solid element plate model. This comparison is made at the stress states evaluated by the plate

model and is evaluated in terms of NAE as function of l_e/t_p in Figure 13, to determine whether a correction for element length is required. The fracture locus for solid elements is not applicable for shell elements, instead the $\varepsilon_{\text{eff}}^{f}$ from Figure 12 at $l_e/t_p = 0.22$ is used as the true fracture strain for a shell element at the average stress state of the failed element. The fracture strain at the different stress states are assumed to be points of the true FFLD and its NAE with $\varepsilon_{\text{eff}}^{f}$ is labelled in Figure 13 with "FFLD". The true necking strain is assumed to be $\varepsilon_{\text{eff}}^{f}$ of the solid element model at $l_e/t_p = 19.85$ and its NAE with $\varepsilon_{\text{eff}}^{f}$ is labelled in Figure 13 with "FLD". The other FLD label in Figure 13 "FLD DSSE" is the necking strain obtained from the shell element plate model in Chapter 5.

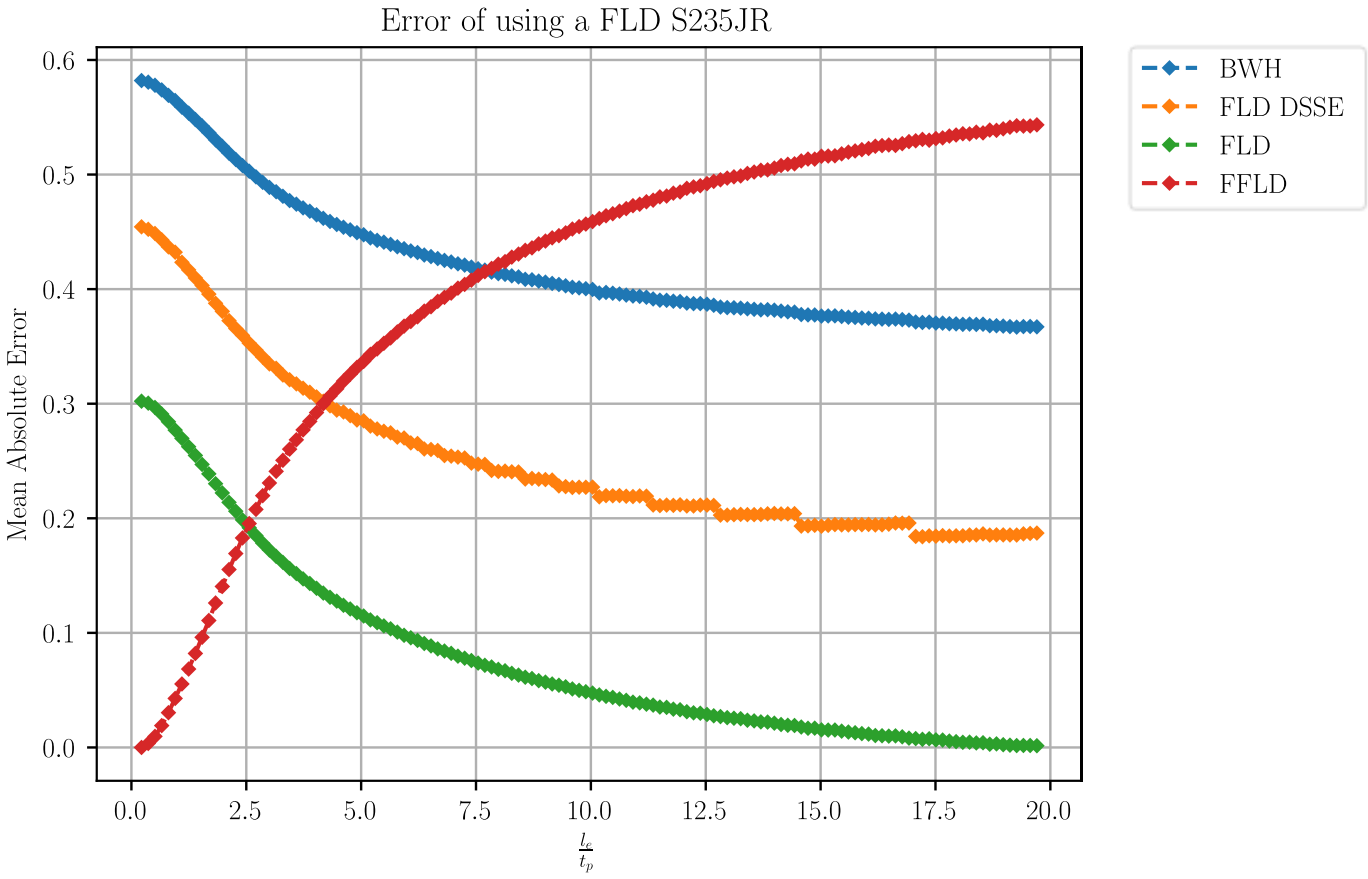

Figure 13 FLD and found FFLD and performance at different element sizes

One observation is that the NAE is highly dependent on the FLD when necking precedes fracture. Another observation is that one calibrated fracture locus does not work for other element sizes as otherwise, the NAE of the FFLD would remain constant. In the best-case scenario, a correction works better than a fit of the EFFLD at each element size using fracture criteria such as HC and MMC as shown in Figure 14. The fits are for ductile fracture criteria and are not expected to perform well at larger element sizes when necking precedes fracture. Also, these fits are continuous, and will also best fit at the element sizes at

which the EFFLD is more continuous, in this case at $l_e/t_p \approx 2.4$. An overview of ranges of NAE within ranges of l_e/t_p for each failure criterion is shown in Table 5.

Table 5 % NAE for FLD, FFLD, and Loci fits

%NAE FOR FLD, FFLD, AND LOCI FITS

	FLD			FFLD	fit	
	Model	DSSE	BWH	Model	HC	MMC
1<LE/TP<5	12- 30	28-44	44-59	0-34	5-12	5-12
5<LE/TP<10	4-12	22-28	39-44	34-46	8-11	7-10
10<LE/TP<20	0-4	18-22	36-39	46-54	11-13	10-13

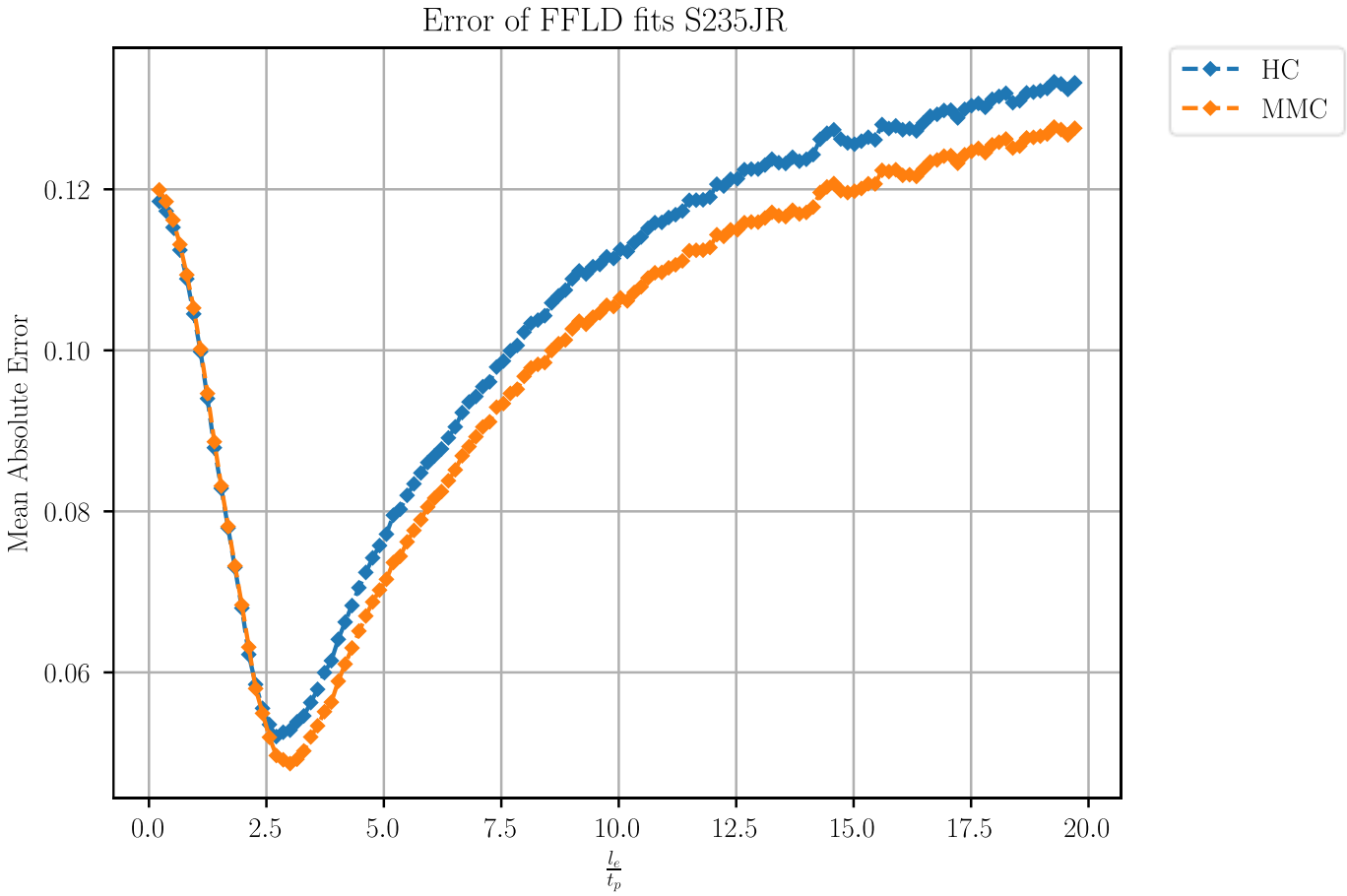

Figure 14 Performance of fitting HC or MMC at different element sizes

Performance of Necking Criteria

The solid MK model presented in this thesis captures deformation instability initiated by an imperfection over a range of plane of stress states. This method is considered more accurate because strains are not assumed small, and the effect of normal stress on necking is also considered. However, this method is too

complicated and computationally expensive for engineering practice. Therefore, analytical models presented in Paragraph 3.2 are compared with the solid MK model in Figure 15.

The FLD named Fracture Solid MK model $L_{el}/t_p = 19.85$ represents an approximation of the limit of the effective fracture strain and the necking strain based on MK analysis with a solid model.

The MK HC fit is a fit of the HC fracture model of MK analysis with shell elements (Pack & Mohr, 2017).

BWH is shown as necking criterion defined by Bressan-Williams $\sqrt{3}/3 \leq \eta \leq 2/3$ and Hill necking criterion for $1/3 \leq \eta \leq \sqrt{3}/3$. Either the power law or Voce-Swift hardening model is used for determining the FLD.

The necking criterion defined by Bressan-Williams is caused by shear instability and is expected to dominate for $\sqrt{3}/3 \leq \eta \leq 2/3$.

The “Hill” graph displays straining instability is the strain at which the loss in integrity due to surface reduction is higher than the increased stiffness due to hardening.

The “Swift” graph shows a diffuse necking criterion similar to Hill but does not consider the specific orientation of instability.

“Stören-Rice Bifurcation” indicates the predecessor of MK analysis and neglects thickness imperfection. The FLD of the bifurcation is a specific solution proposed by Stoughton & Zhu [2004].

From Figure 15, can be concluded that a correct hardening model, in this case, Voce-Swift, aids in predicting through-thickness necking. In this case, Hill correctly predicts necking for $1/3 \leq \eta \leq \sqrt{3}/3$. The HC fit of the MK analysis performed the best for $\sqrt{3}/3 \leq \eta \leq 2/3$.

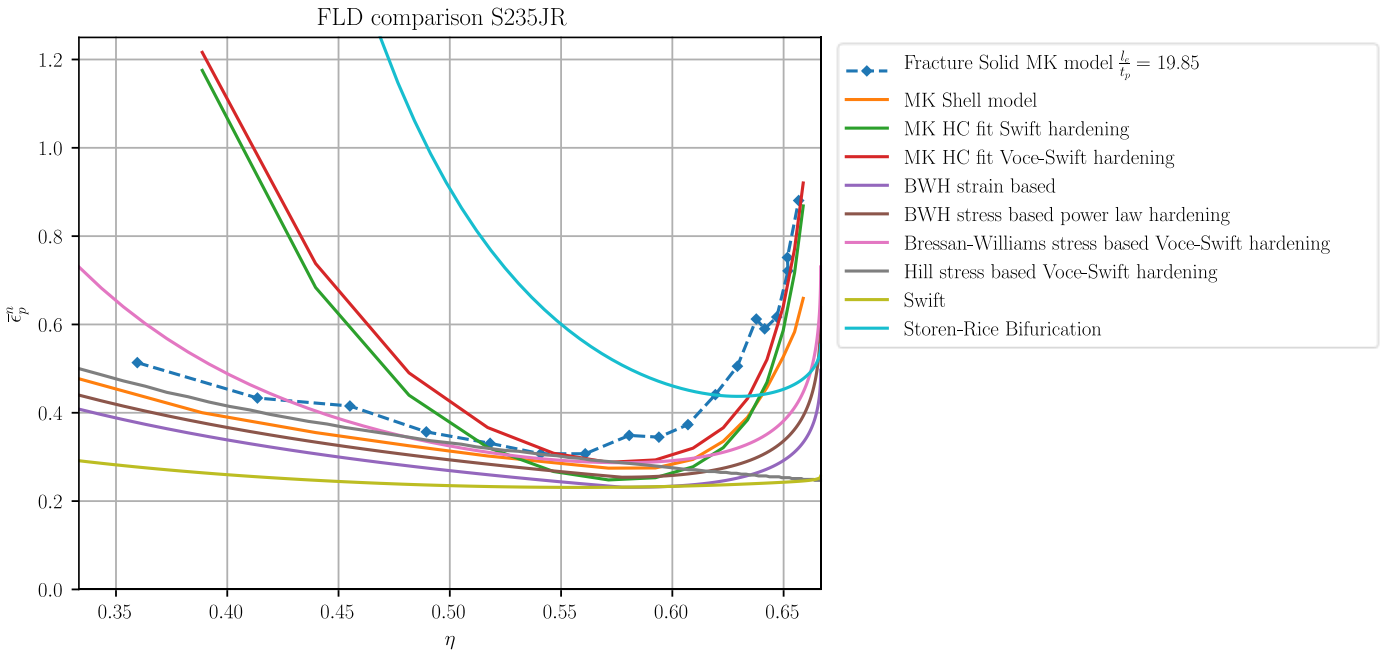

Figure 15 Comparison of FLD with different hardening models

6.5. Effective Fracture Strain Correction Methods

The second assessment is the NAE estimation of correction methods to see when the application is recommendable. The first method assessed is from Walters [2014], which can be calibrated by determining the EFFLD found at a specific l_e/t_p, and use the MMC fracture locus together with a necking criterion, in this comparison BWH, MK from a solid and shell element model. The NAE of the FFLD based on Walters [2014] using the FLD from the solid element plate model proposed in Chapter 4 labelled as FLD from model, DSSE-analysis, and BWH, are shown in Figure 16, Figure 17, and Figure 18, respectively.

The element length dependency of the EFFLD by Bijleveld [2018] uses effective fracture strains from a range of l_e/t_p from the uni-axial stress state from the solid model and uses the EFFLD points from the model at $l_e/t_p = 0.22$ as FFLD and at $l_e/t_p = 19.85$ as FLD in Figure 19. Normally, one uses an FFLD and FLD, and therefore the MMC FFLD calibrated with $l_e/t_p = 0.22$ is used, together with the FLD from DSSE, BWH, and the convention MK model in Figure 20, and Figure 21 respectively. The NAE of the method proposed in this thesis is shown in Figure 22, Figure 23, and Figure 24, for the FFLD + FLD from the model, MMC FFLD + DSSE FLD, and MMC FFLD + BWH FLD respectively. The range of NAE found within specific ranges of L_{el}/t_p is shown for each correction method and their FLD in Table 6, Table 7, and Table 8 for FLD obtained from the solid MK model, DSSE, and BWH, respectively.

These tables show that the FLD and FFLD are less accurate than EFFLD over almost the entire range, except for the FLD from the model when $l_e/t_p > 10$. Overall, the method from Bijleveld [2018] is more accurate as it acts as fit with an arctan shape using two calibration parameters.

The one case in which the model presented in this thesis performs better is when the FFLD and FLD from the solid element plate model presented in Chapter 4 are used. The used FLD from the solid element plate model is assumed to be the effective fracture strain at $l_e/t_p = 19.85$ according to equation 3.25, which is slightly higher than the real necking strain. The presented method is comparable to the method presented by Walters [2014], but the presented model performs better for smaller element lengths. The fitted method proposed by Bijleveld [2018] performs better with inaccurate fracture methods as it is more designed to be a fit.

The method from Walters [2014] performs comparably with the other methods when $l_e/t_p > 10$, as it is near the necking strain, which is the lower limit of the method. The inaccuracy at smaller element sizes is not surprising as an inverse linear function is calibrated at an element size at which the effective fracture strain is not entirely inverse-linear. The FFLD is recalibrated at the element size used for the method proposed by Walters [2014], which results in lower NAE around the calibrated element size.

The choice of a model depends on whether absolute accuracy, consistency, or number of calibration constants is preferred. n purely in NAE, the method proposed by Bijleveld [2018] is more accurate. Still, a

model with consistency, as in low dependence of element size range used for calibration on NAE, then the present model can be used. The present model is theoretically motivated and can be extended as the shape assumed is highly simplified for application.

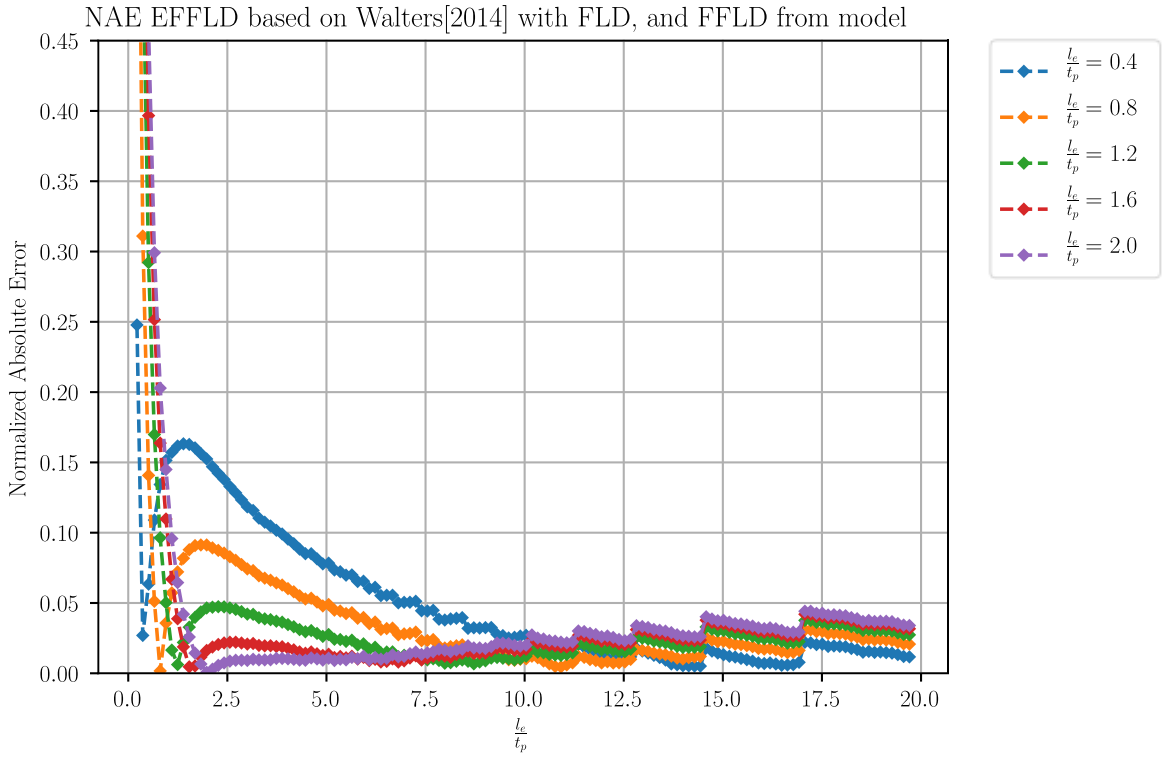

Figure 16 Performance of correction as proposed by Walters [2014] calibrated at five element sizes with the found FLD

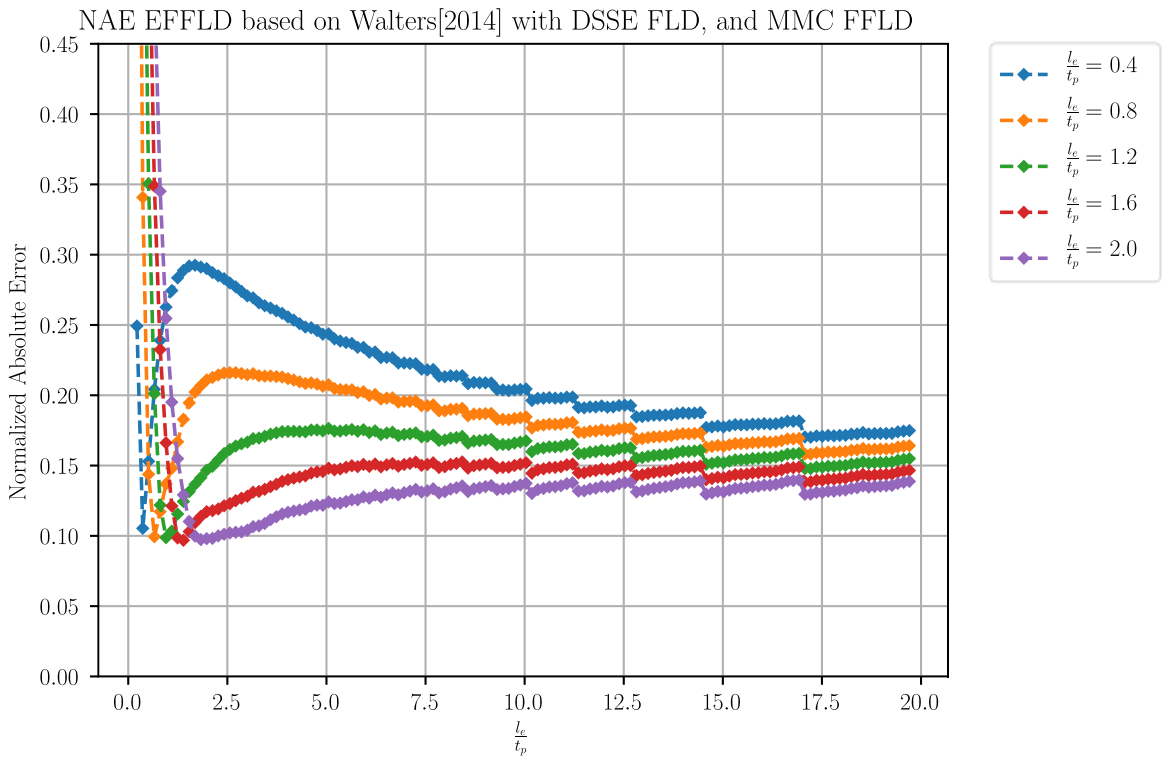

Figure 17 Performance of correction as proposed by Walters [2014] calibrated at several element sizes with the FLD found with DSSE

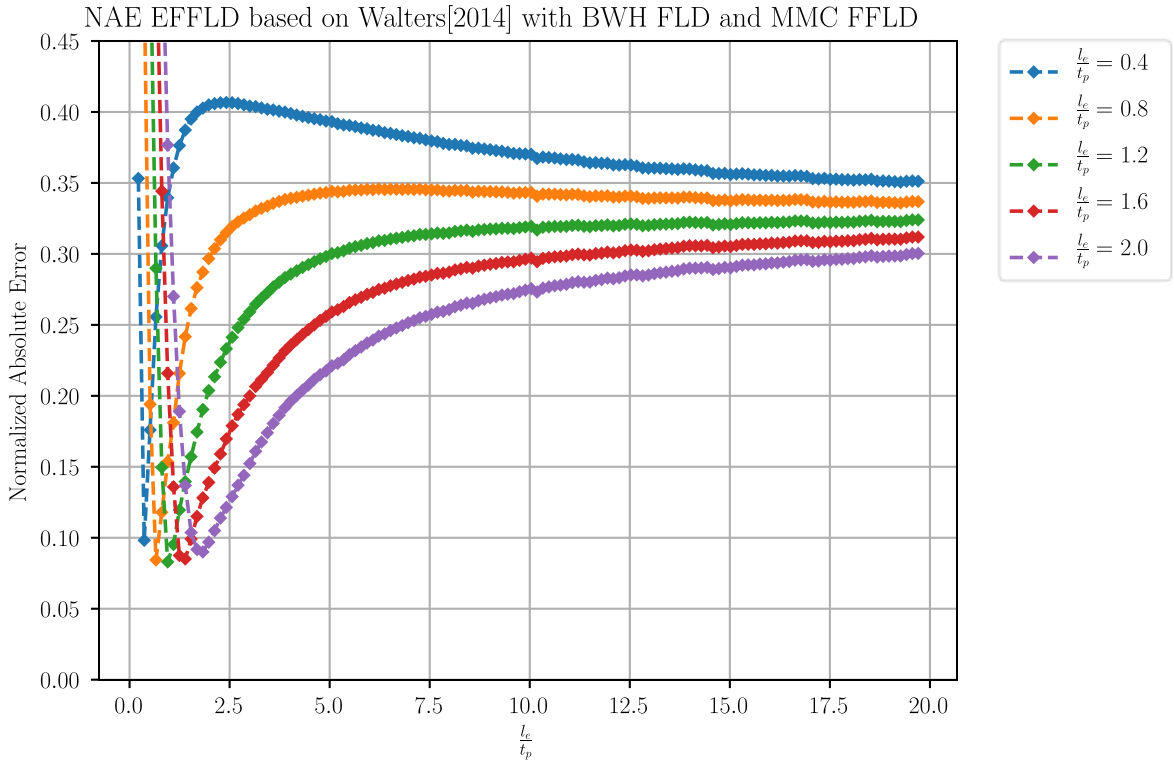

Figure 18 Performance of correction as proposed by Walters [2014] calibrated at several element sizes with FLD from BWH

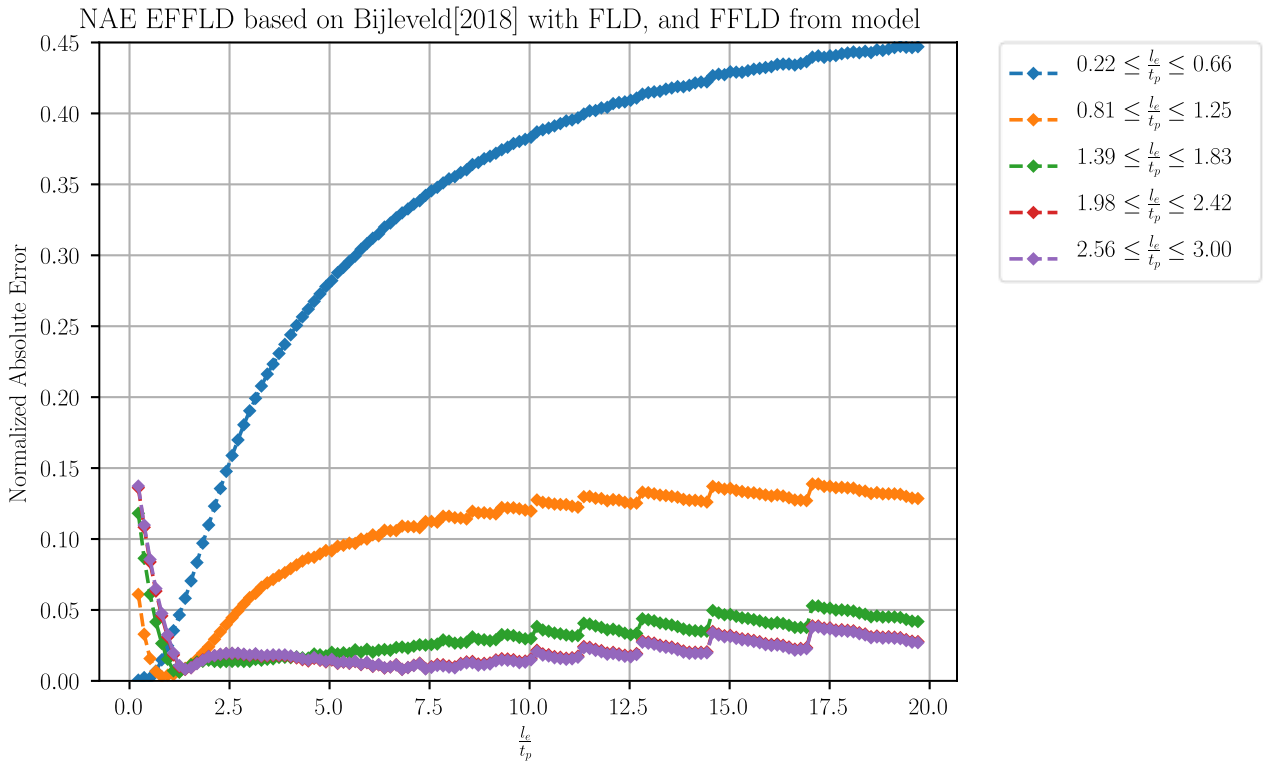

Figure 19 Performance of correction as proposed by Bijleveld [2018] calibrated at five element ranges with real FLD

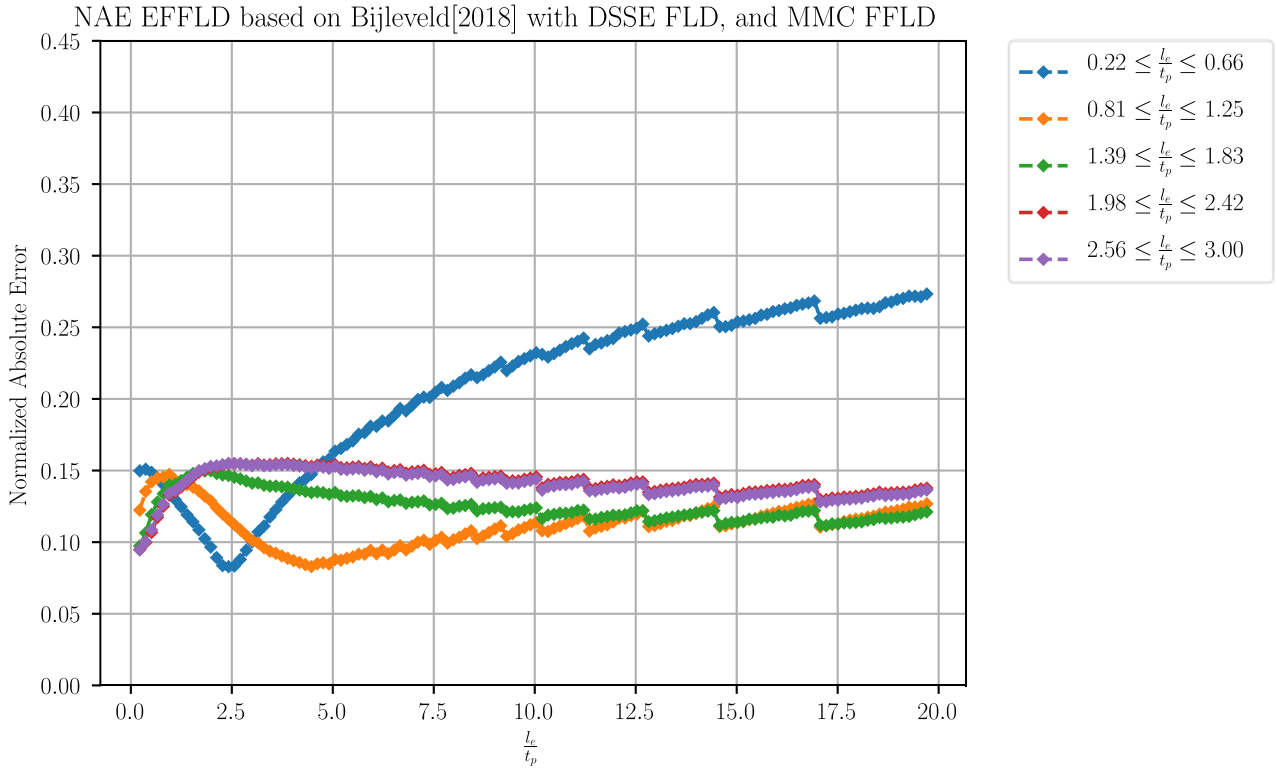

Figure 20 Performance of correction as proposed by Bijleveld [2018] calibrated at five element ranges with FLD from DSSE

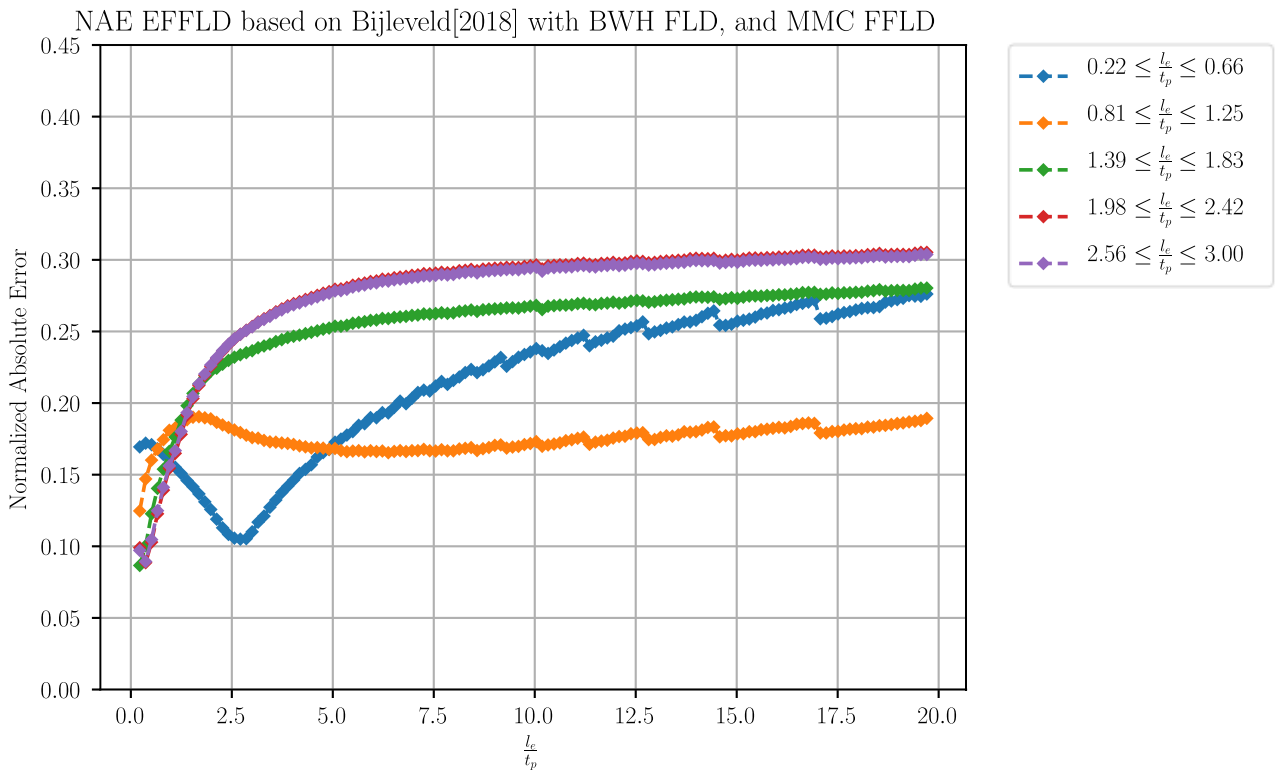

Figure 21 Performance of correction as proposed by Bijleveld [2018] calibrated at five element ranges with FLD from BWH

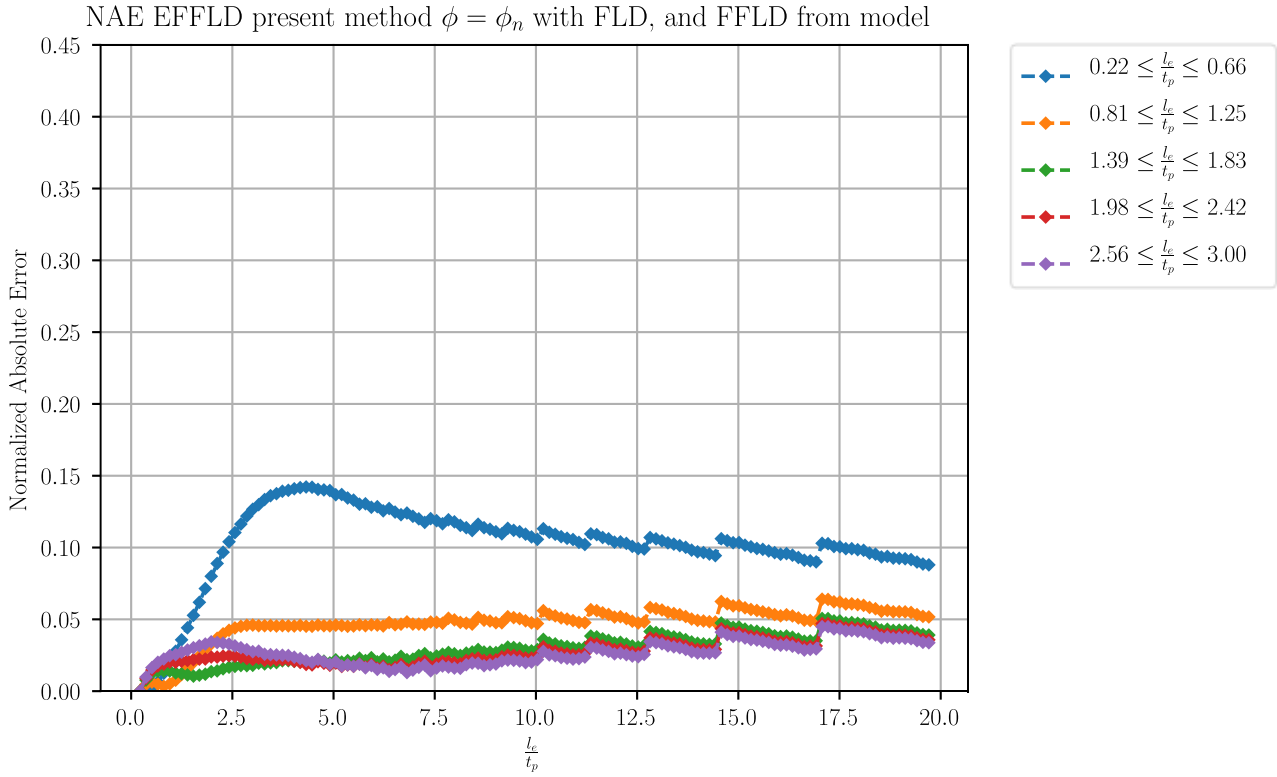

Figure 22 Performance of correction as proposed in this thesis, calibrated at five element ranges with FLD and FFLD from model

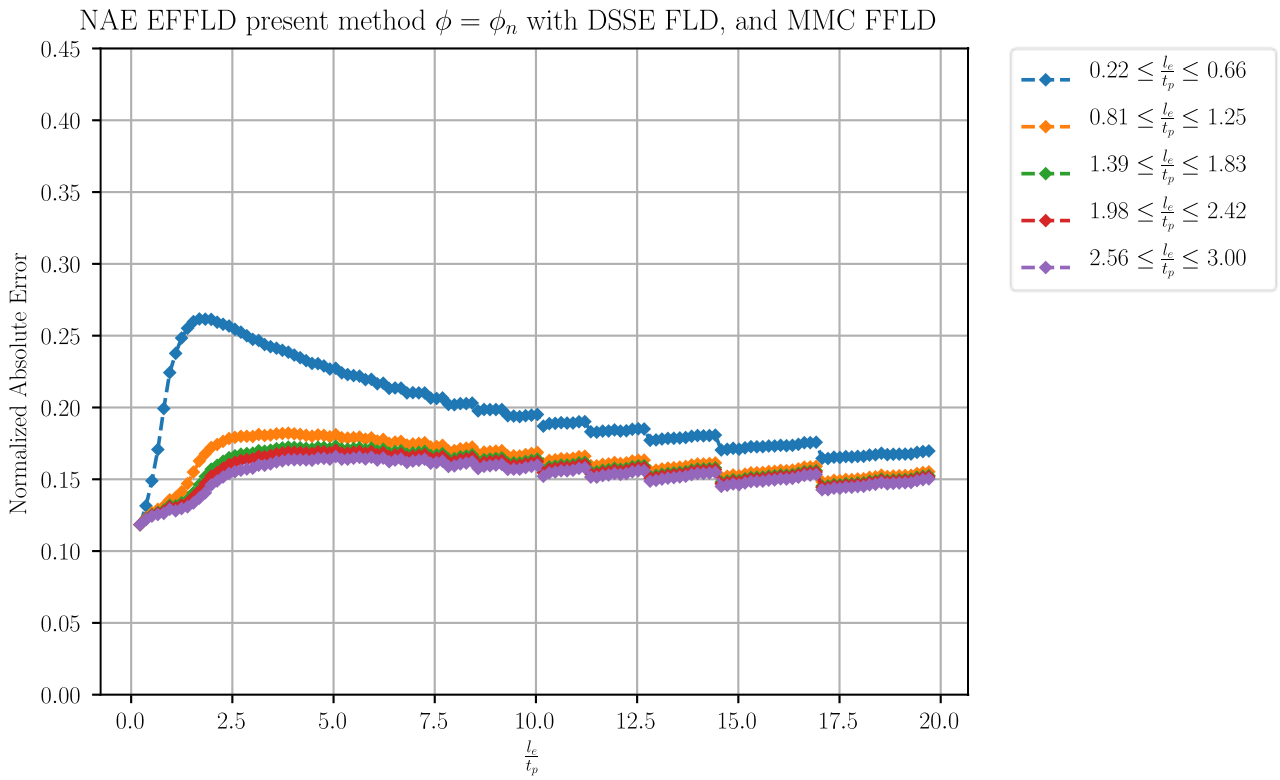

Figure 23 Performance of correction as proposed in this thesis, calibrated at five element ranges with FLD from DSSE

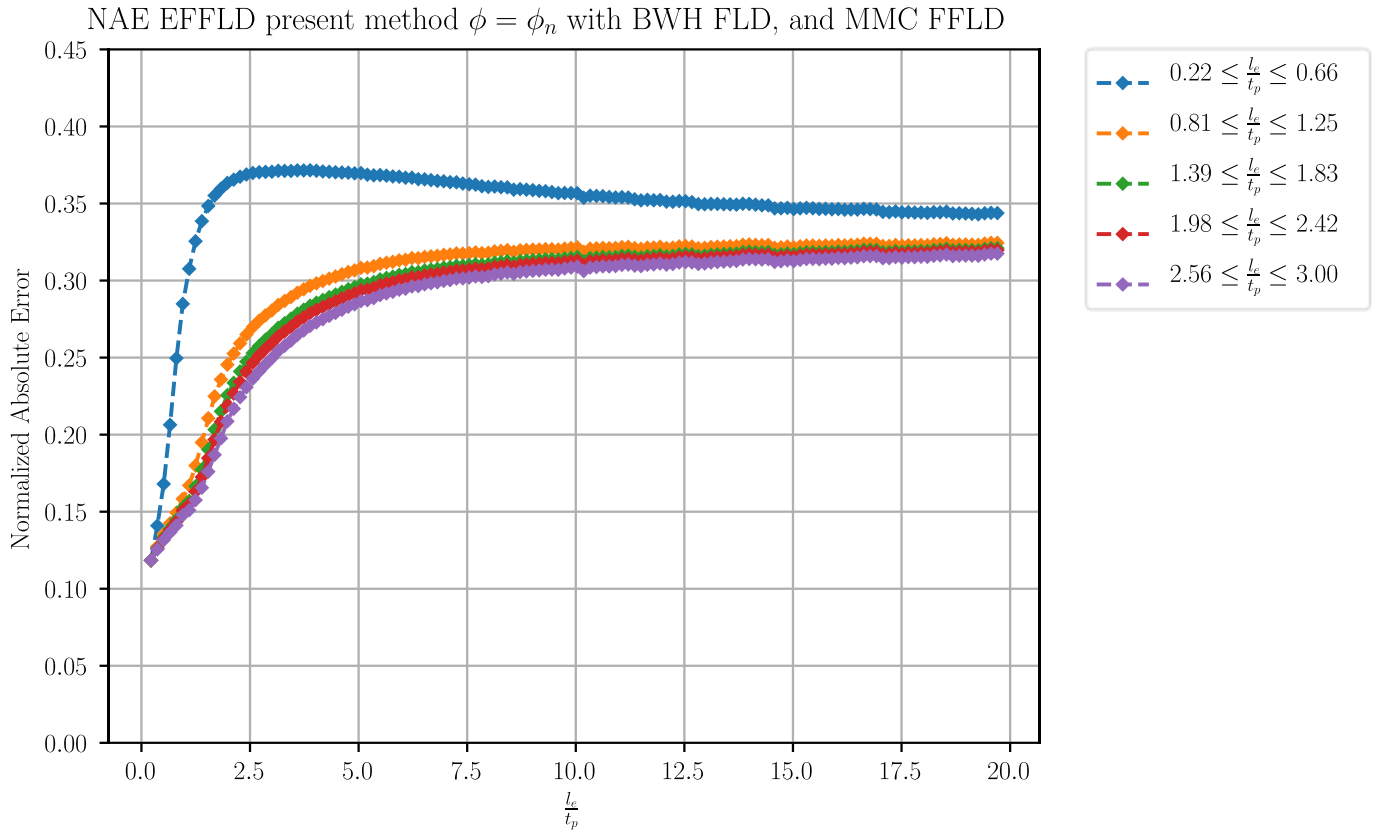

Figure 24 Performance of correction as proposed in this thesis, calibrated at five element ranges with FLD from BWH

Table 6 EFFLD % NAE with FLD from solid MK

		%NAE RANGE WITH FLD AND FFLD FROM MODEL		
	Le calibration	**1<Le/tp<5**	**5<Le/tp<10**	**10<Le/tp<20**
WALTERS [2014]	0.8	4.8 – 9.2	1.1-4.8	1.1-3
	1.6	0 – 12	0.9-2.3	2.3-4.4
BIJLEVELD [2018]	$0.81<l_e/t_p<1.25$	0.8-9.2	9.2-12.5	12.5-13.8
	$2.56<l_e/t_p<3$	0 – 1.8	0.7-1.3	1.3-4
PRESENT MODEL	$0.81<l_e/t_p<1.25$	0-4.6	4.6-5.3	4.5-6.2
	$2.56<l_e/t_p<3$	1.8-3.5	1.3-2.2	2.2-4.9
SOLID MK		12- 30	4-12	0-4

Table 7 EFFLD % NAE with DSSE FLD

		%NAE RANGE WITH FLD FROM DSSE		
	Le calibration	**1<Le/tp<5**	**5<Le/tp<10**	**10<Le/tp<20**
WALTERS [2014]	0.8	13.9 – 21.6	18.2-19.1	15.7-18.4
	1.6	9.6.2-23	12.5-13.7	12.7-13.7
BIJLEVELD [2018]	$0.81<l_e/t_p<1.25$	8.2-11.7	9.8-12.2	11.3-13
	$2.56<l_e/t_p<3$	10.7 – 12.3	12.1-12.9	11.9-13
PRESENT MODEL	$0.81<l_e/t_p<1.25$	13.7-18.2	16.5-17.9	14.7-16.8
	$2.56<l_e/t_p<3$	12.7-16.5	15.6-16.5	14.2-16.1
DSSE	0.8	28-44	22-28	18-22

Table 8 EFFLD %NAE with BWH FLD

		%NAE RANGE WITH FLD FROM BWH		
	Le calibration	**1<Le/tp<5**	**5<Le/tp<10**	**10<Le/tp<20**
WALTERS [2014]	0.8	16.8 – 34.3	34.2-34.3	33.5-34.2
	1.6	8.8 - 31.6	21.8-27.3	27.3-30
BIJLEVELD [2018]	$0.81<l_e/t_p<1.25$	12.6-13.8	13.5-17	16.6-18.7
	$2.56<l_e/t_p<3$	12.3- 23.9	23.9-27.3	27.1-29.4
PRESENT MODEL	$0.81<l_e/t_p<1.25$	15.4-30.7	30.7-32.1	32.1-32.8
	$2.56<l_e/t_p<3$	15.4-28.5	28.5-30.9	30.9-31.7
BWH		44-59	39-44	36-39

Remarks

A good necking curve is essential in predicting the minimum effective fracture strain for larger shell elements. However, the methods for determining one are estimations. This can be resolved with a Forming Limit Band rather than a single curve, which uses a band in which necking can occur. For example, MK analysis can provide a lower and upper bound of the FLD when a minimum and maximum imperfection is applied, respectively.

Another issue is the load path dependency of necking. Still, its impact is lowered with a Forming Limit Stress Diagram as proposed by among others Arrioux et al. [1982] together with proportional necking damage accumulation (forming severity concept) as proposed by Bai & Wierzbicki [2008b].

6.6. Potential of Correction Methods

The previous analysis only compares the theories in terms of NAE; another assessment is how well the theories agree with simulations as the FLD and FFLD that were used have an NAE. Initially, $\varepsilon_1^{f*}(x)$ the first principle effective fracture strain of the solid element plate model is analysed. This strain is displayed with and without a Gaussian filter for numerical for numerical differentiation. This numerical derivative is used the first principle strain of the plate at a distance $x/2$ from the centre of the neck and plate $\varepsilon_1^{f}(x)$. This local strain is derived in equation 6.2.

$$\varepsilon_1^{f*}(x) = \ln\left(\frac{x_f}{x}\right) = \ln\left(\frac{\int_0^x e^{\varepsilon_1^f(x)}\,dx}{x}\right) \rightarrow \varepsilon_1^{f}(x) = \frac{dx e^{\varepsilon_1^{f*}(x)}}{dx} \approx \frac{\Delta x e^{\varepsilon_1^{f*}(x)}}{\Delta x} \tag{6.2}$$

The first principle global and local fracture strain are displayed in Figure 25 and Figure 26, respectively with $\phi_0 \neq 90°$.

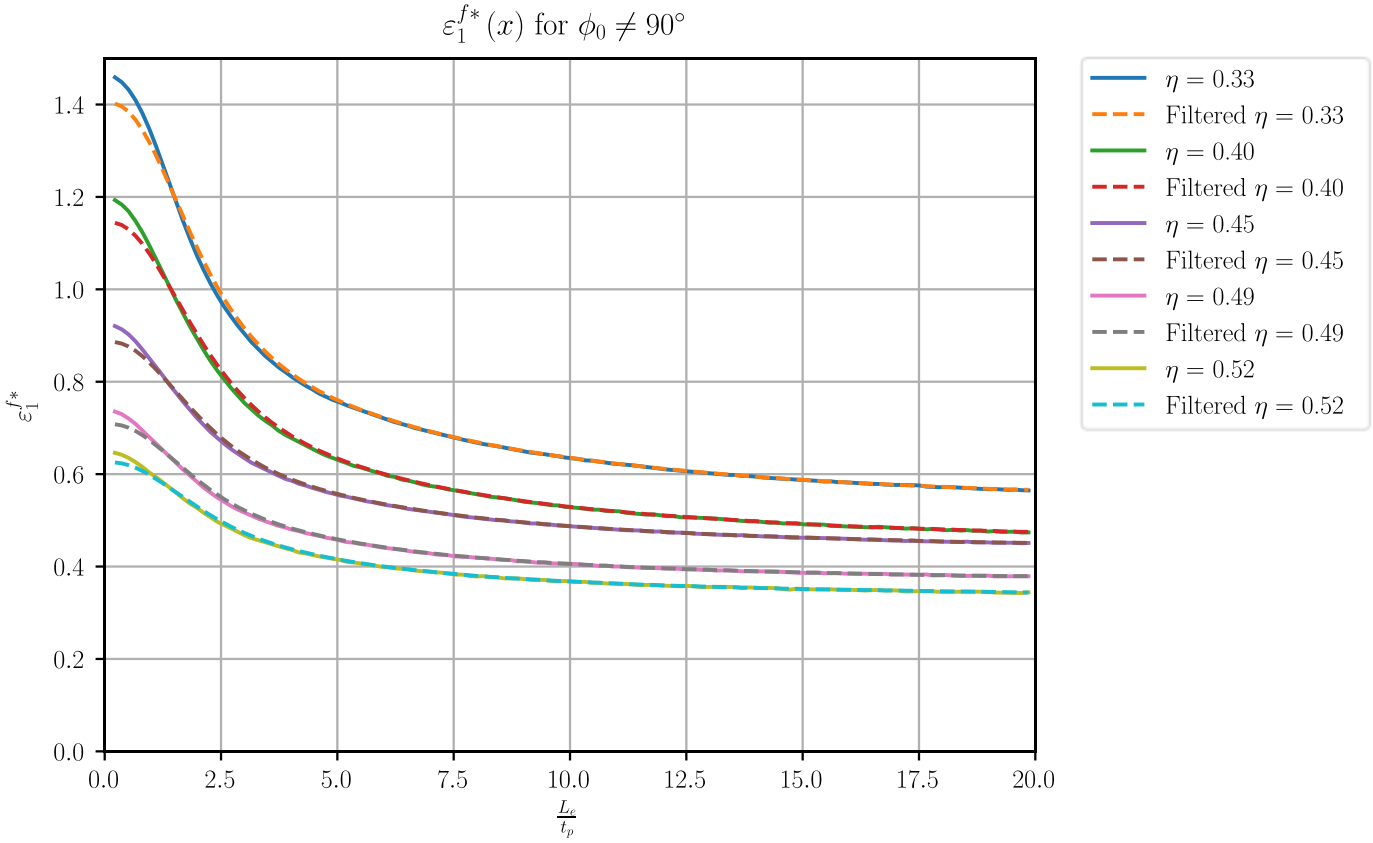

Figure 25 First principal strain at onset of fracture as function of element length filtered and unfiltered.

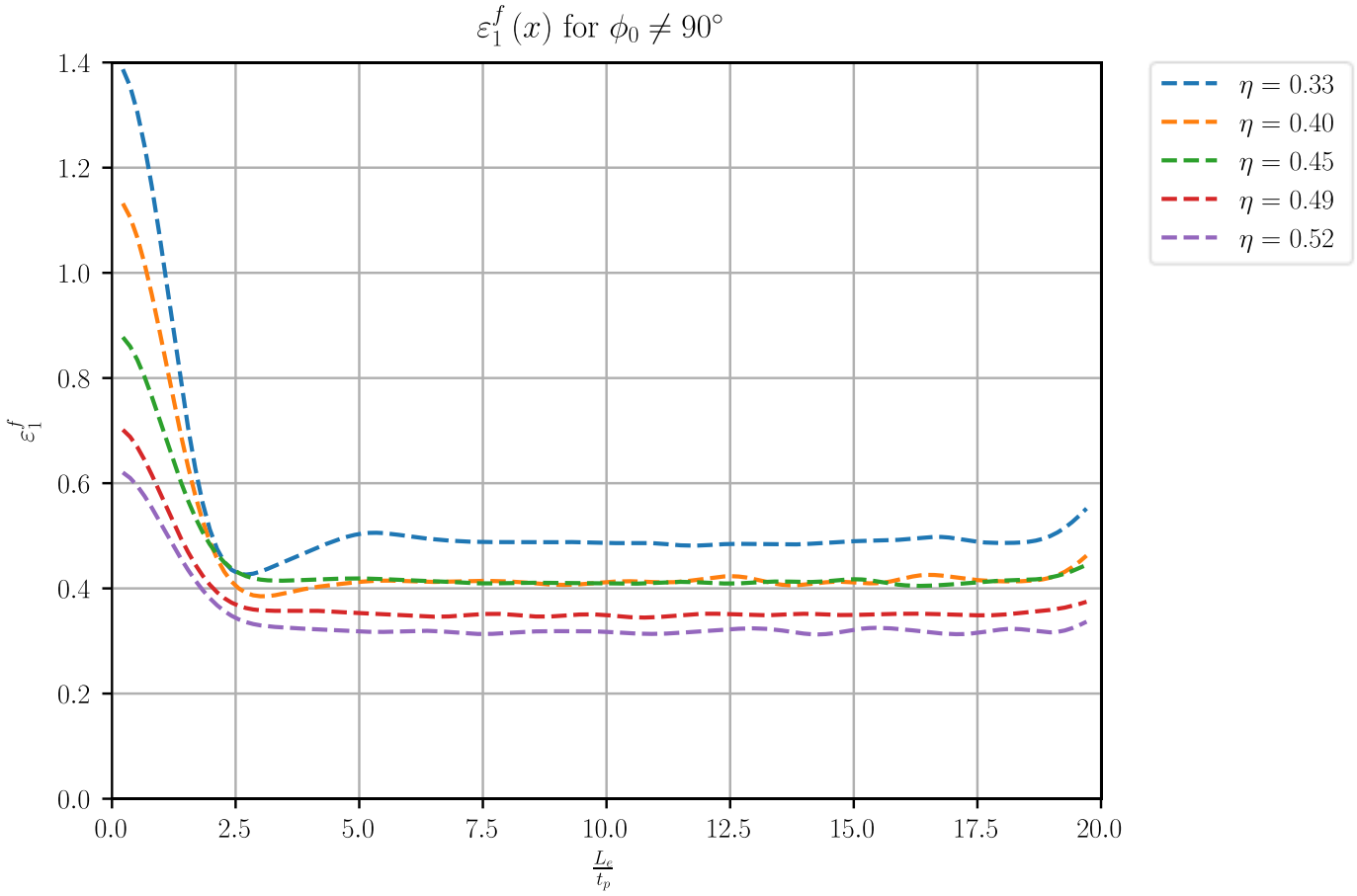

Figure 26 Local first principal strain at onset of fracture as function of twice the distance from the centre of the neck.

From $\varepsilon_1^f(x)$ in Figure 26, one can see that plastic strain past necking strain is limited to within the neck length (Gorji et al., 2016). The initial neck length is as proposed in Paragraph 3.6 almost constant over the stress states as $\frac{d\varepsilon_1^f(x)}{dx} = 0$ at $x \approx 2$. As expected, the strain within the neck increases when approaching the centre of the neck.

For a comparison of the other theories, over all stress states the scaling factor γ is obtained with equation 6.3 and shown in Figure 29. The plot contains all the stress states to show the consistency of γ over stress states.

$$\gamma = \frac{\left(\varepsilon_1^{f*} - \varepsilon_1^n\right)}{\left(\varepsilon_1^f - \varepsilon_1^n\right)} \tag{6.3}$$

Figure 27 shows that the proposed method and Walters [2014] with a good necking and fracture strain are highly accurate, but diverges at the larger element sizes, as the fracture strain of the largest shell element analysed is used instead of a necking strain. The method proposed in Walters [2014] and Bijleveld [2018] both require an effective fracture at a specific element size instead of an FFLD based on fracture strain at a

point. The figure also explains why the method of Bijleveld [2018] performed well in terms of NAE with strain based BWH as it mostly neglected the necking strain when calibrated with only five experimental points (calibrated within range $3/13 \leq L_{el}/t_p \leq 14/13$).

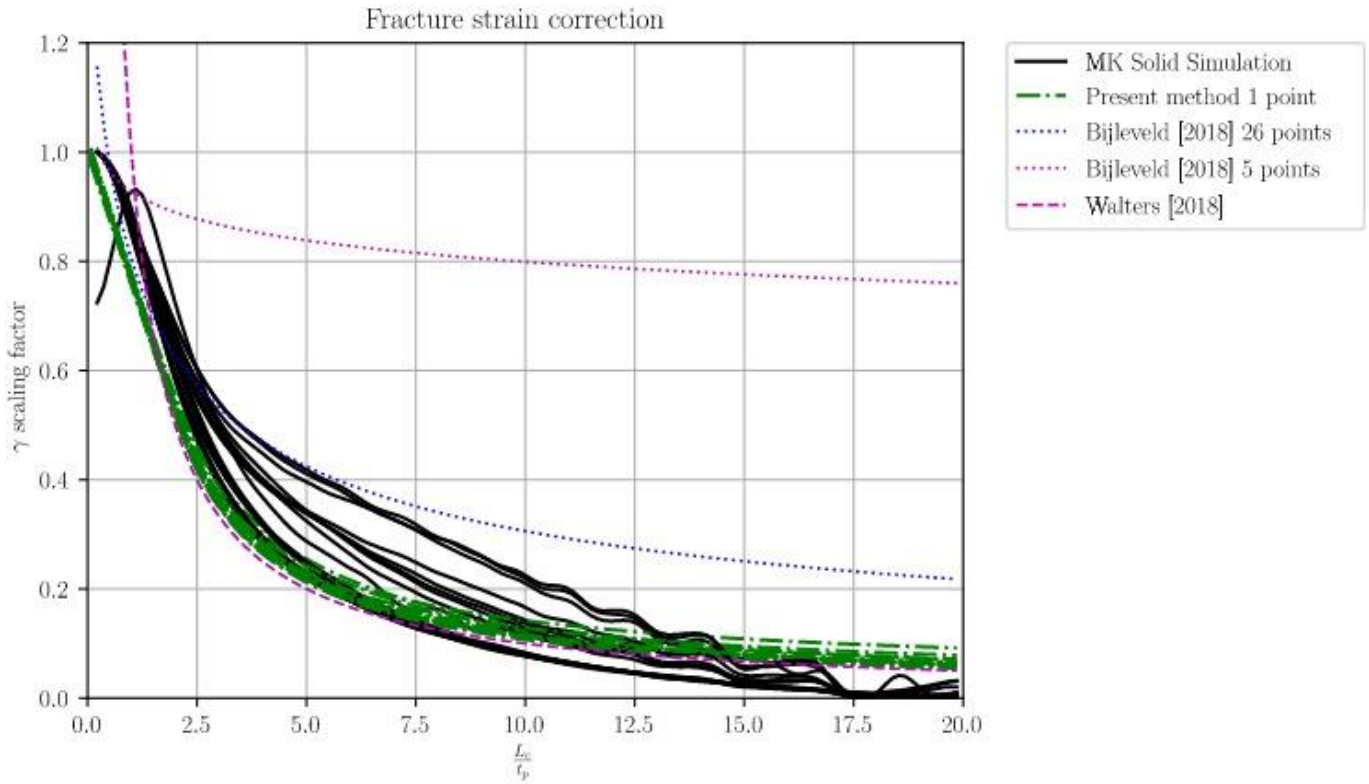

Figure 27 Fracture strain correction for element size

6.8. Conclusion

This chapter answers the first research question: "*How can the accuracy of stress state dependent ductile fracture prediction models for shell elements be evaluated?*". By using a solid MK model as a benchmark as described and calibrated in Chapter 4 and 5, respectively. The error can be estimated in terms of NAE as a function of L_{el}/t_p. Still, a more accurate method to determine the viability of a correction method is to identify the element length dependency as defined in paragraph 3.5. This enables unitless comparison over plane stress states.

The expectations that the EFFLD scales with L_{el}/t_p with stress state is confirmed in paragraph 6.3 and 6.6. Also, shells cannot capture the through-thickness localisation accurately (Paragraph 6.3), especially for element sizes equal to their plate thickness or larger, as the effect of necking increases. The expectation that fracture loci, such as HC or MMC can be applied to shells is valid (Pack & Mohr, 2017)(Figure 14), but with a margin of error and a constant element size should be used. Correction methods improve the accuracy of fracture prediction methods (Paragraph 6.5 and 6.6), especially when necking strains are

accurate. Both methods proposed in this thesis and in Walters [2014] can perform with high accuracy (Paragraph 6.6). However, the present method can predict fracture strain for smaller elements which the other correction methods cannot (Paragraph 6.6).
The forming limit diagram is best estimated with a higher accuracy hardening model with Hill and an MK HC fit combination (Paragraph 6.7).

7 Proposed Procedure

7.1. Introduction

The goal of this chapter is to answer the main research question of this thesis:
"*How can ductile fracture strains for hardening materials be converted to effective fracture strains in shell elements with practical dimensions for crash simulation?*". This research question is answered by proposing a procedure for obtaining effective fracture strains in this chapter.

Outline

The proposed procedure corrects fracture strain with the necking strain. The strain in the neck varies linearly with the distance from the centre of the neck, as suggested within Paragraph 3.6, and shown in Paragraph 6.5. The correction requires a neck length, necking strain, and fracture strain. The necking strain is determined through a forming limit diagram (FLD), which requires a hardening model. This is determined by iteratively adjusting an initially estimated hardening model in a FEM simulation of a dog bone shaped tensile test until the simulation and test converge (Paragraph 7.2.). With this hardening model, the FLD is determined for negative strain ratio $\alpha = \varepsilon_2/\varepsilon_1$ as shown in Hill [1952] (Paragraph 7.3.). With the necking and fracture strain known from the tensile test, the neck length is estimated (Paragraph 7.4.). The fracture strain is modelled by the HC fracture locus. This requires the calibration of two experiments for two different stress states in plane stress (Paragraph 7.5.). With the FFLD, FLD and neck width, the effective strain is obtained and put into an effective fracture forming limit diagram EFFLD (Paragraph 7.6) for direct implementation within a commercial FEM Package. For validation, the proposed procedure is applied with the material analysed within this thesis (Paragraph 7.7.). The full procedure from testing to EFFLD is summarized in the flowchart shown in Figure 28.

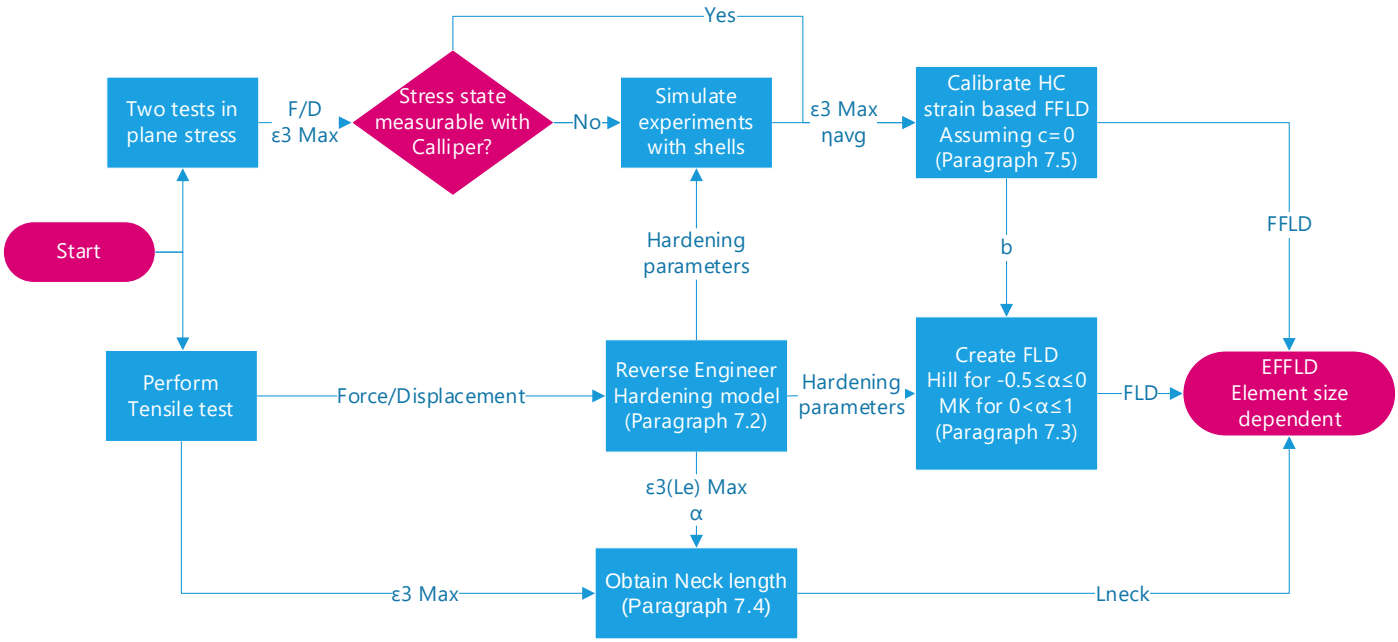

Figure 28 Flowchart for the proposed procedure of obtaining an EFFLD

7.2. Hardening Model

The hardening model is calibrated based on a tensile test on a flat dog bone shaped specimen with a minimum width to thickness ratio of five. The output of this test is in the form of a force-displacement curve. The force measurements and displacements are provided by the tensile testing machine and the extensometer over the gauge length, respectively. An initial hardening model is applied to the tensile test simulation, which is iteratively adjusted until the force-displacement curve of the FEA simulation matches the test. The geometry of the model requires only the gauge length. The recommended shell element size is a fifth of the width of the gauge section. This is assumed to be sufficiently small to describe diffuse necking and is closer to the larger element sizes typically used for crash simulations. The model is strained by applying the displacement measured by the extensometer in one direction on one edge and constraining displacement of the opposite edge in the same direction.

The shell elements are required to have thinned due to the conservation of volume. In this thesis, the Voce-Swift hardening model, from equation 2.19, is used to calibrate the hardening model. The input is the initial hardening parameters which are varied with each iteration, and the output is the force at each displacement step. The difference between the force from measurements and simulation is minimized with a root mean square error minimizer. The analysis is limited to plastic strains, and weighting factors are recommended to be reduced after necking as the capacity of shells to capture post necking deformation is limited, as is shown in Figure 3. For comparison, material hardening parameters for the material analysed in this thesis (S235) is found in

Table 3.

7.3. Forming Limit Diagram

The necking strain is obtained from two forming limit diagrams. This is because the first domain of $-0.5 \leq \alpha \leq 0$ is best described by straining instability and the second domain of $0 < \alpha \leq 1$ by shear instability. The first domain is accurately defined by Hill [1952] as shown in equation 3.13 with a correct hardening model; in this case Voce-Swift.

The second domain is best described by MK analysis, but for simplicity is described by Bressan Williams necking criterion as shown in equation 3.18. This combination of Bressan-Williams and Hill is referred to as BWH throughout this thesis and was introduced by Alsos et al. [2008].

7.4. Neck length Estimation

The neck length is obtained with the assumed linear strain distribution proposed in Paragraph 3.6 that assumes $\phi_0 = 0$. The neck length is explicitly solved in equation 3.54, such that:

- $\varepsilon_{1,\mathrm{N}}$ from necking criterion from Hill in equation 3.13 for $\alpha = -0.5$ as it is assumed to neck at a uni-axial stress state.
- $\varepsilon_{1,\mathrm{F}}$ measured from a tensile test with a ball point micrometer. The strain is obtained by measuring b and t as depicted in Figure 29 and using equation 7.1.
- ε_1^{f*} and L_e as the first principal true fracture strain and element length respectively of the shell element at the location of fracture from a simulation of the tensile test.

$$\varepsilon_{1,\mathrm{F}} = \int_{L_0}^{L} \frac{dL}{L} = \ln\left(\frac{L}{L_0}\right) = \ln\left(\frac{S_0}{S}\right) = \ln\left(\frac{b_0 \cdot t_0}{b \cdot t}\right) \tag{7.1}$$

With:

- b and t as the original width and thickness of the specimen at the cross-section, respectively.
- b_0 and t_0 as the width and thickness of the specimen at the cross-section respectively after fracture.
- S_0 and S as the critical element surfaces in the cross-section originally and after fracture, respectively.

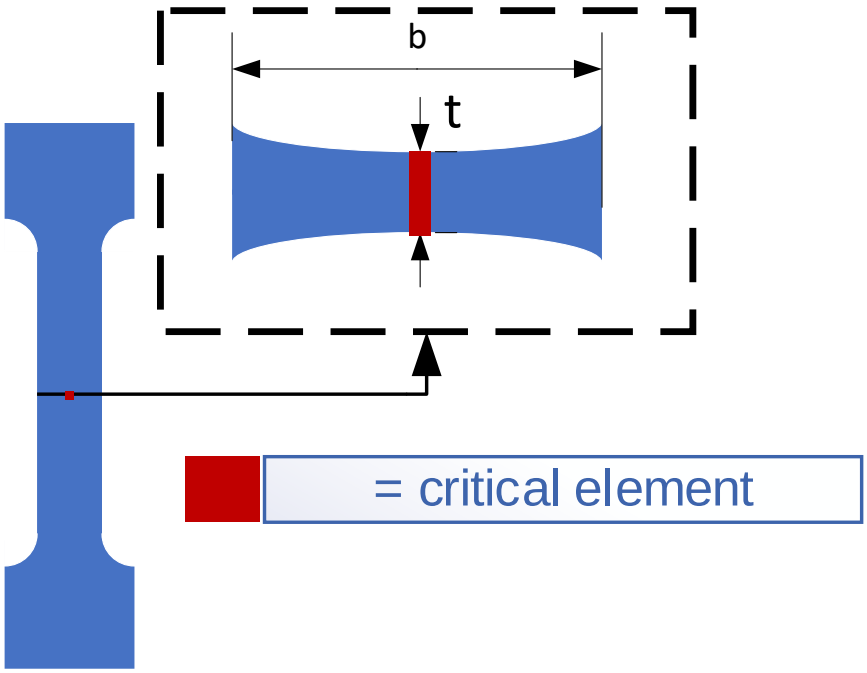

Figure 29 Sketch of the required measurements of a tensile test

7.5. Fracture Locus Calibration

This paragraph presents a method, similar to the one used by Roth & Mohr [2016], for obtaining the first principal fracture strain by calibration of an FFLD. The proposed FFLD is the HC fracture locus in equation 3.10. The calibration parameter c is assumed to be zero as it has limited effect in plane stress (Mohr & Marcadet, 2015). The fracture locus has two other calibration parameters 'a' and 'b', preferably obtained from a plane strain and stress test, and an equi-biaxial punch test. This is because the FFLD is best described by two separate FFLD from $0.33 \leq \eta < 0.58$ and $0.58 \leq \eta < 0.67$ as shown in Figure 12. The experiments are expected to fail in plane stress, and thus the strain is assumed constant over thickness. This allows accurate fracture strain derivation from thickness measurements with equation 7.2 plane strain ($\alpha = 0, \eta = \sqrt{3}/3$).

$$\varepsilon_{3,\mathrm{F}} = \ln\left(\frac{t}{t_0}\right) \tag{7.2}$$

From the third principal fracture strain $\varepsilon_{3,\mathrm{F}}$, the first principal true fracture strain $\varepsilon_{1,\mathrm{F}}$ is derived following the conservation of volume in equation 7.3, and 7.4 for the equi-biaxial punch test ($\alpha = 1$).

$$\varepsilon_{1,\mathrm{F}} = \frac{(-\varepsilon_{3,\mathrm{F}} - 1)\alpha - \varepsilon_{3,\mathrm{F}} - 1 \pm \sqrt{(\varepsilon_{3,\mathrm{F}} + 1)\left((\varepsilon_{3,\mathrm{F}} + 1)\alpha^2 + (-2\varepsilon_{3,\mathrm{F}} + 2)\alpha + \varepsilon_{3,\mathrm{F}} + 1\right)}}{2\alpha(\varepsilon_{3,\mathrm{F}} + 1)} \tag{7.3}$$

$$\varepsilon_{1,\mathrm{F}} = 1 - \frac{1}{\sqrt{\varepsilon_{3,\mathrm{F}} + 1}} \tag{7.4}$$

with $\varepsilon_{1,\mathrm{F}}, \varepsilon_{3,\mathrm{F}}$ and α, the equivalent plastic strain until fracture $\varepsilon_{\mathrm{eq}}^{f}$ is derived with equation 2.3.

Calibration parameter b is calibrated with $\varepsilon_{\mathrm{eq}}^{f}$ from the equi-biaxial punch test with equation 7.5, which is based on equation 3.7, solved for the equi-biaxial stress state.

$$b = \varepsilon_{\mathrm{eq-equi-biaxial}}^{f} \tag{7.5}$$

The other parameter is solved implicitly from equation 7.6 using the fracture strain of a plane strain and stress test specimen $\varepsilon_{\mathrm{eq-plane\ strain}}^{f}$.

$$(1 + 2^{a-1})^{\frac{1}{a}} = \sqrt{3}\left(\frac{\varepsilon_{\mathrm{eq-plane\ strain}}^{f}}{b}\right)^{-0.1} \tag{7.6}$$

A more accurate estimate is made for the FLD with the MK fit from Pack and Mohr [2017] in equation 3.7 for $0 \leq \alpha < 1$. The plane necking strain is from Hill necking criterion, as shown in equation 3.13.

This proposed equi-biaxial stress state and plane strain state specimens require no simulation for obtaining the stress state. The calibration parameters can alternatively be obtained with the fracture strains of two other plane stress tests with each a different stress state. Then equation 3.7 with $c = 0$ can be solved for a and b implicitly, or a minimizer can be used to find the calibration parameters.

7.6. Implementation

The EFFLD is calculated with equation 3.40 for $L_{el} \geq L_n$, and equation 3.41 for $L_{el} < L_n$. With the element length being the largest element expected to initiate fracture. For implementation, a plot for the EFFLD has to be provided with on the x-axis $\varepsilon_2^{f*} = \varepsilon_1^{f*}\alpha$ and on the y-axis ε_1^{f*}. To create the plot, the effective fracture strain is required to be evaluated over $-0.5 \leq \alpha \leq 1$, with at least ten values of α over which the FEM software will interpolate the effective fracture strain.

7.7. Validation

The proposed procedure is, in theory, more accurate, but validation is required. Therefore, the proposed fracture strain correction procedure is applied to the material analysed in this thesis.

The material had four calibration tests performed by Bijleveld [2018] and Haag et al. [2017]. The first two calibration tests are shown in Figure 30, and Figure 31 are tensile tests with a dog bone shaped specimen, and one of the two tests has a notch to evaluate a different stress state. The other two tests shown in Figure 32, and Figure 33 are punch tests of round flat plates tested in the die shown in Figure 34, and one is notched to evaluate a different stress state, called the Hašek punch test. The tensile tests and punch had a plate thickness of 6.1mm and 3.05mm respectively and were made from the same plate; more details are described in Bijleveld [2018].

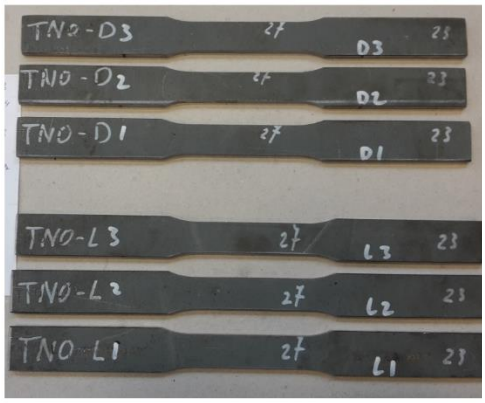

(a) Initial geometry

(b) Fractured geometry

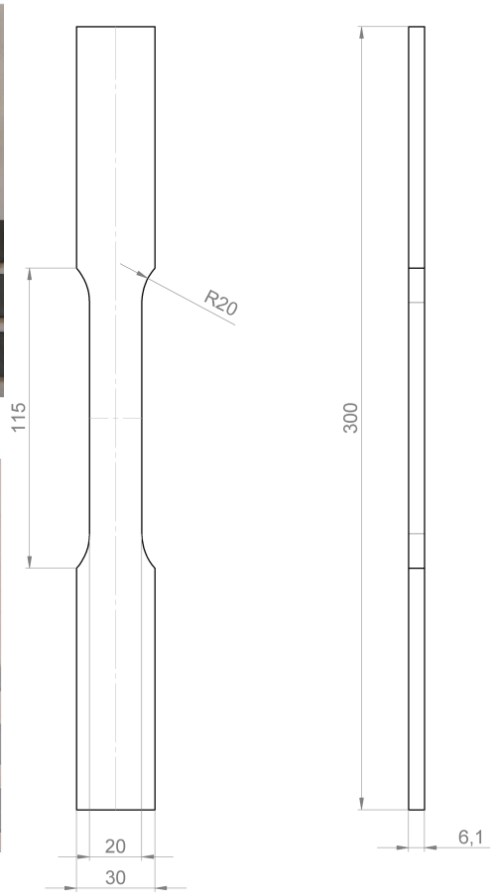

(c)

Figure 30 Pictures (a) before and (b) after testing and (c) drawings in mm of tensile test specimens from Haag [2017]

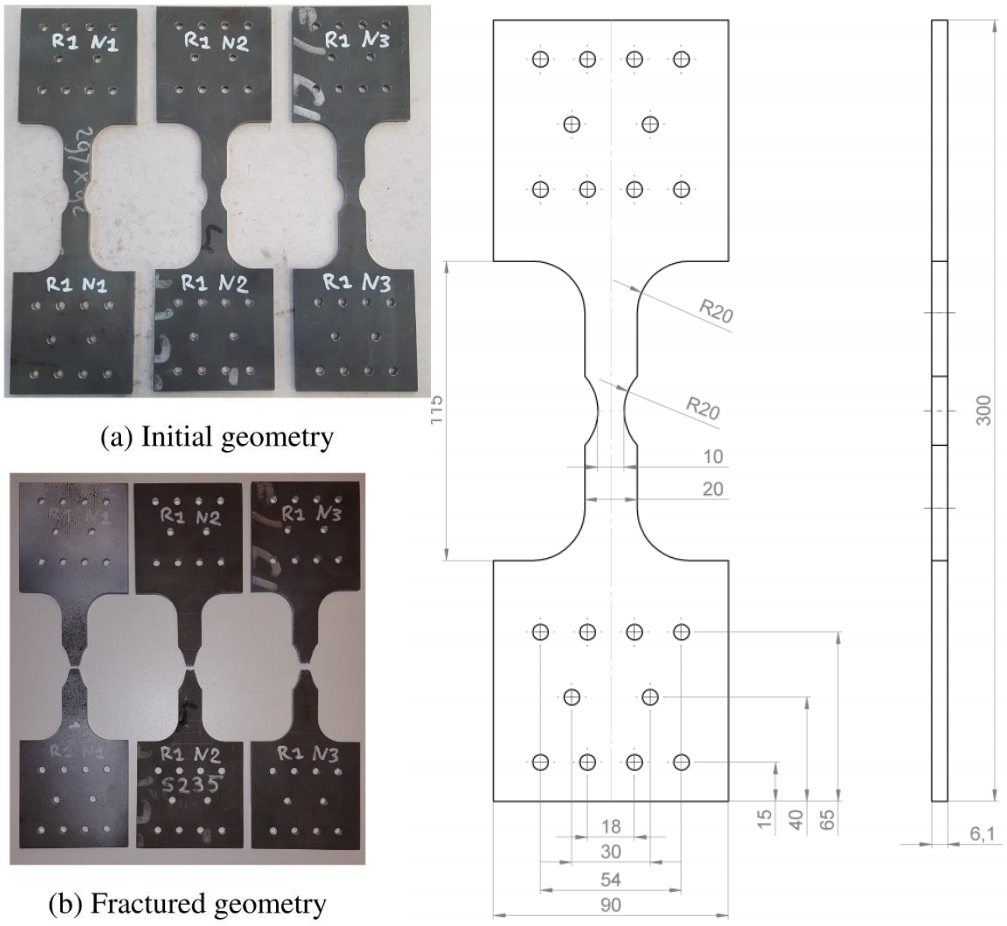

Figure 31 Pictures (a) before and (b) after testing and (c) drawings in mm of notched tensile test specimens from Bijleveld [2018]

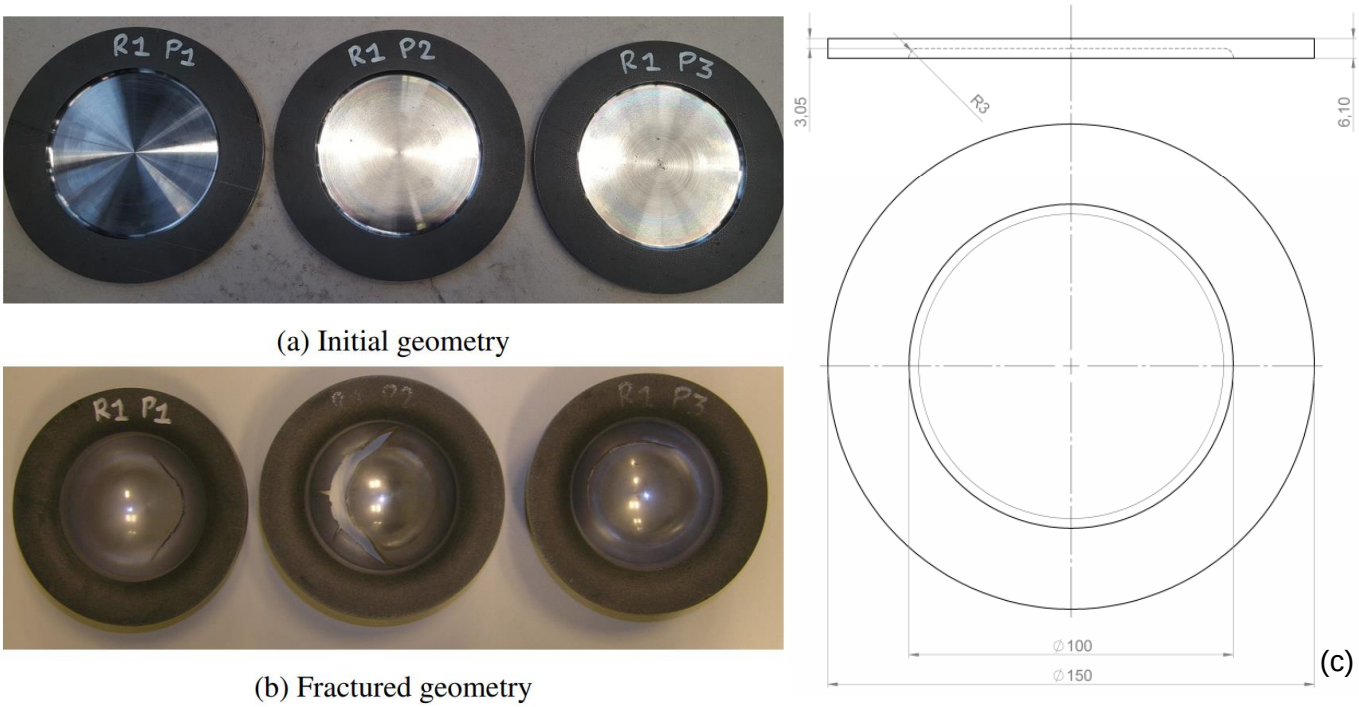

Figure 32 Pictures (a) before and (b) after testing and (c) drawings in mm of equi-biaxial punch test specimens from Bijleveld [2018]

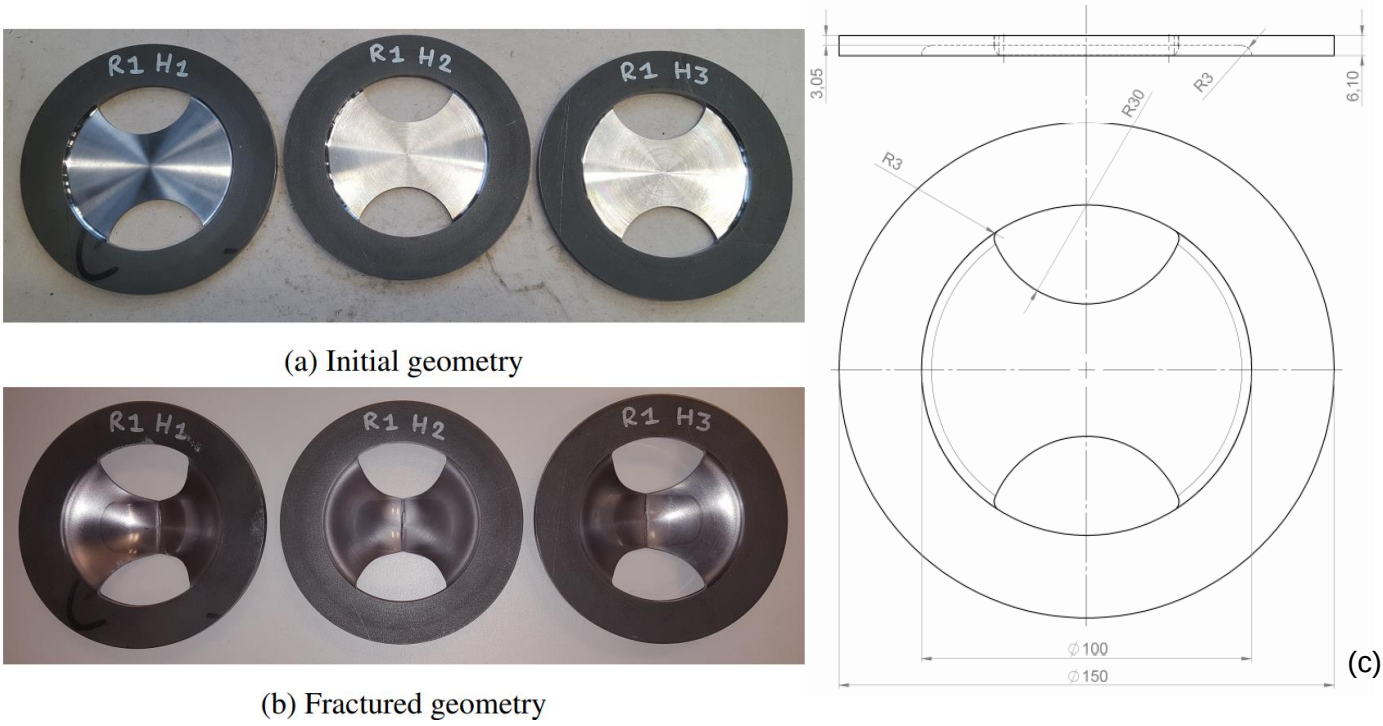

Figure 33 Pictures (a) before and (b) after testing and (c) drawings in mm of notched/ Hašek punch test specimens from Bijleveld [2018]

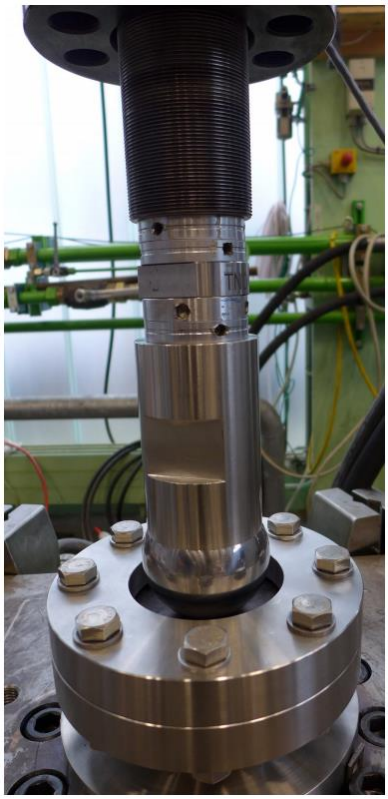

Figure 34 Experimental setup for punch testing from Bijleveld [2018].

The average stress states are obtained from FEM simulations of the experiments with either shells or solids. These simulations are done by Bijleveld [2018] with models of the tensile and punch tests with twelve and six solid elements through the thickness, respectively. The load path of the fractured element of each test is displayed in Figure 35 with depictions of the tests.

The hardening model is calibrated with the tensile test with a Voce-Swift hardening model. The hardening parameters are found in

Table 3. The neck is assumed to be two plate thicknesses wide, as it is the minimum found neck width in this thesis in Paragraph 6.6.

The FFLD is calibrated with two experiments that failed in plane stress each for one separate stress state. This means that $\bar{\theta}$ is a function of η as shown with a black line in Figure 1 and Figure 35(b). The latter figure shows that only the Hašek punch and equi-biaxial punch remain in plane stress. Therefore, only these two experiments are used for calibration. The FFLD is calibrated with $\varepsilon_{\mathrm{eq}}^{f}$ and the average triaxiality $\eta_{avg}$of both experiments displayed in Table 9. These values are fitted with an HC fracture locus with $a = 0.19$ and $b = 18.54$. The FFLD is validated by a raking test shown in Figure 36 in which two inclined plates are impacted by a spherically shaped indenter; more details of the setup are found in Haag [2017]. The DIC and ball point micrometer (BPM) measurements from Haag et al. [2017] are shown in Table 10 with estimated $\varepsilon_{\mathrm{eq}}^{f}$ in Table 11. Measurements from experiment 1 were omitted in Haag et al. [2017]. The first experiment required four times raising the indenter and dropping it before failure. Experiments 2 and 3 were sanded and lubricated better to reduce friction and increased the drop height to fail in one drop. Increased friction changes the strain distribution over the contact surface with the indenter. This can increase plastic strain outside the neck after necking. This can reduce the difference between the fracture strain from a fracture locus and the fracture strain measured further away from the centre of the neck. Figure 26 indicates the difference in fracture strain measured as function two times the distance from the centre of the neck. This is a possible cause of the difference in $\varepsilon_{\mathrm{eq}}^{f}$ from the measurements in Table 11. The difference in $\varepsilon_{\mathrm{eq}}^{f}$ between measurements and DIC is expected as it uses displacements of dots over a length of 20mm to 21mm, which act as nodes of a shell. This means that the strains from DIC are best compared with $\varepsilon_{\mathrm{eq}}^{eff}$ at $L_e = L_0/t_p = 20.5/6.1 = 3.36$.

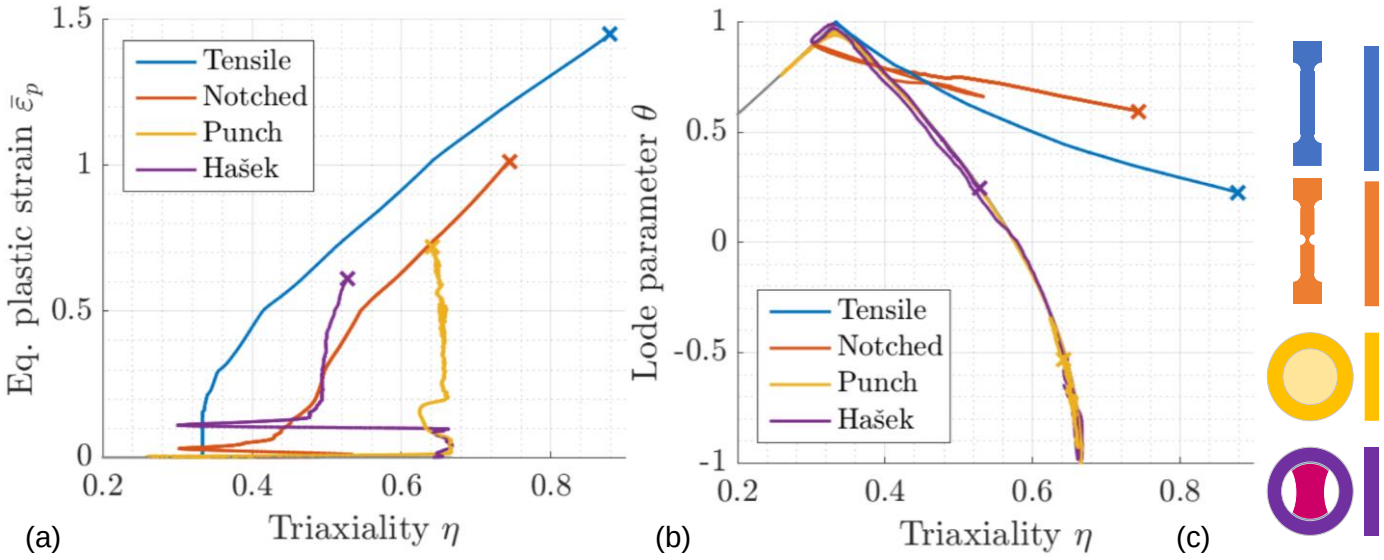

Figure 35 Load paths in terms of η and $\bar{\varepsilon}_p$(a), η and θ (b) for experiments from Bijleveld [2018] with illustrations of specimen top and side view (c).

Table 9 Fracture strain and stress state of plane stress experiments

	SIMULATION		MEASURED
	η_{avg}	$\varepsilon_{\mathrm{eq}}^{f}$	$\varepsilon_{\mathrm{eq}}^{f}$
HAŠEK PUNCH	0.52	0.61	-
EQUI-BIAXIAL PUNCH	0.65	0.72	0.71

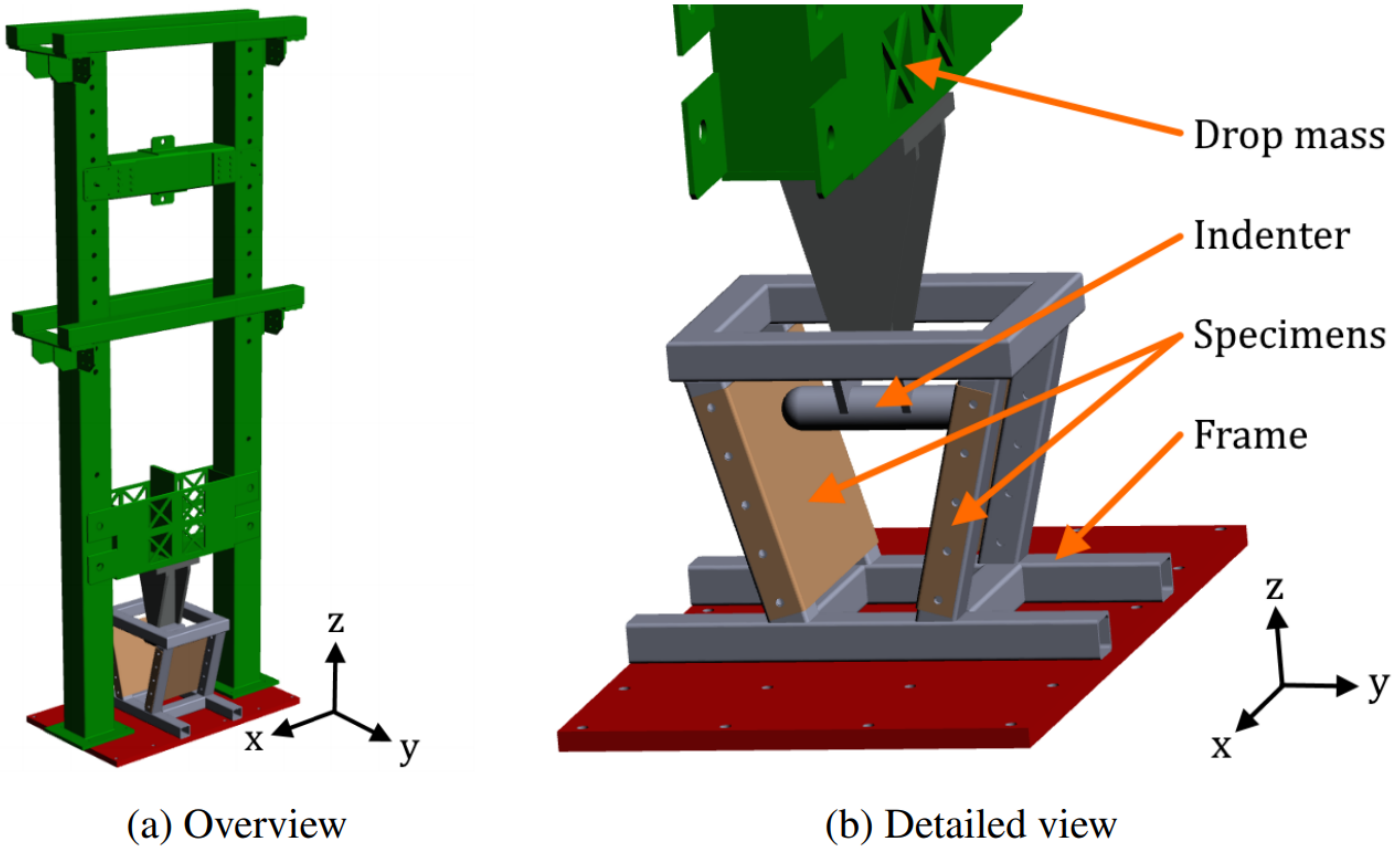

Figure 36 Computer aided (a) overview and (b) detailed view of a raking test setup from Haag [2017]

Table 10 DIC and ball point micrometer measurements of raking experiment from Haag [2017]

	DIC			BPM
	$\varepsilon_{1,\mathrm{F}}$	$\varepsilon_{2,\mathrm{F}}$	$\varepsilon_{3,\mathrm{F}}$	$\varepsilon_{3,\mathrm{F}}$
EXPERIMENT 2	0.61	0.07	-0.42	-0.38
EXPERIMENT 3	0.48	0.04	-0.35	-0.30
EXPERIMENT 4	0.48	0.06	-0.36	-0.33

Table 11 Fracture strain estimation from DIC and ball point micrometer measurements, and HC FFLD for raking test

				BPM	DIC	HC
	α	β	η	$\varepsilon_{\mathrm{eq}}^{f}$	$\varepsilon_{\mathrm{eq}}^{f}$	$\varepsilon_{\mathrm{eq}}^{f}$
EXPERIMENT 2	0.11	0.58	0.61	0.59	0.52	0.59
EXPERIMENT 3	0.08	0.56	0.60	0.48	0.40	0.58
EXPERIMENT 4	0.13	0.59	0.61	0.49	0.43	0.59

The FLD is calibrated with a MK HC fit by Pack and Mohr [2017] from equation 3.7 with $b = 12.91 \cdot 10^{15}$, $d = 0.07$ and $\varepsilon_{\mathrm{eq-PST}}^{n} = 0.29$ from the necking criterion from Hill in equation 3.13 with a Voce-Swift

hardening model and the equi-biaxial punch test for calibration. The necking strains for the stress states from Table 11 are shown in Table 12 for the separate FLD. This table shows the effective fracture strain under the name EFFLD DIC and EFFLD SHELL, which is obtained for the element length considered for DIC measurement and the shell element length used in Bijleveld [2018], respectively. These effective fracture strains are obtained with equation 7.7 using the HC fracture strains and the necking strains from BWH and the MK fit labelled BWH and MK fit, respectively. For comparison the effective fracture strain found in the solid element plate model is included in Table 12, labelled as MK solid.

Table 12 Necking strain and effective fracture strain for raking test

	FLD		**EFFLD DIC**			**EFFLD SHELL**		
	$\varepsilon_{\mathrm{eq}}^{n}$		$\varepsilon_{\mathrm{eq}}^{eff}$ for $L_e = 3.36$			$\varepsilon_{\mathrm{eq}}^{eff}$ for $L_e = 4.10$		
	BWH	MK fit	BWH	MK fit	MK Solid	BWH	MK fit	MK solid
EXPERIMENT 2	0.29	0.31	0.39	0.40	0.40	0.37	0.39	0.40
EXPERIMENT 3	0.29	0.30	0.38	0.39	0.39	0.37	0.37	0.38
EXPERIMENT 4	0.30	0.32	0.39	0.40	0.41	0.37	0.38	0.41

The effective fracture strain is calculated with equation 7.7 based on equation 3.40 for $L_{el} \geq L_n$.

$$\varepsilon_{\mathrm{eq}}^{eff} = ln\left(\frac{1}{L_{el}}\left(\frac{2\sqrt{\alpha^2+\alpha+1}}{\sqrt{3}}\frac{L_n}{\left(\varepsilon_{\mathrm{eq}}^{n}-\varepsilon_{\mathrm{eq}}^{f}\right)}\left(1-e^{\frac{\sqrt{3}\left(\varepsilon_{\mathrm{eq}}^{f}-\varepsilon_{\mathrm{eq}}^{n}\right)}{2\sqrt{\alpha^2+\alpha+1}}}\right)+\left(L_{el}-L_n\right)\right)\right)\frac{2\sqrt{\alpha^2+\alpha+1}}{\sqrt{3}}+\varepsilon_{\mathrm{eq}}^{n} \qquad (7.7)$$

The effective fracture strains from the solid plate model are included for comparison in the same table. The effective fracture strains do predict the lower measurements from DIC, and the FFLD does predict the maximum measured in one test.

For indication the cross-section of an element with $L_e = 3.36$ is shown in Figure 37, representing the fractured element in experiment 2. With distance representing the length of an element. This is with a neck length, strain ratio, fracture strain, and necking strain considered in this case study.

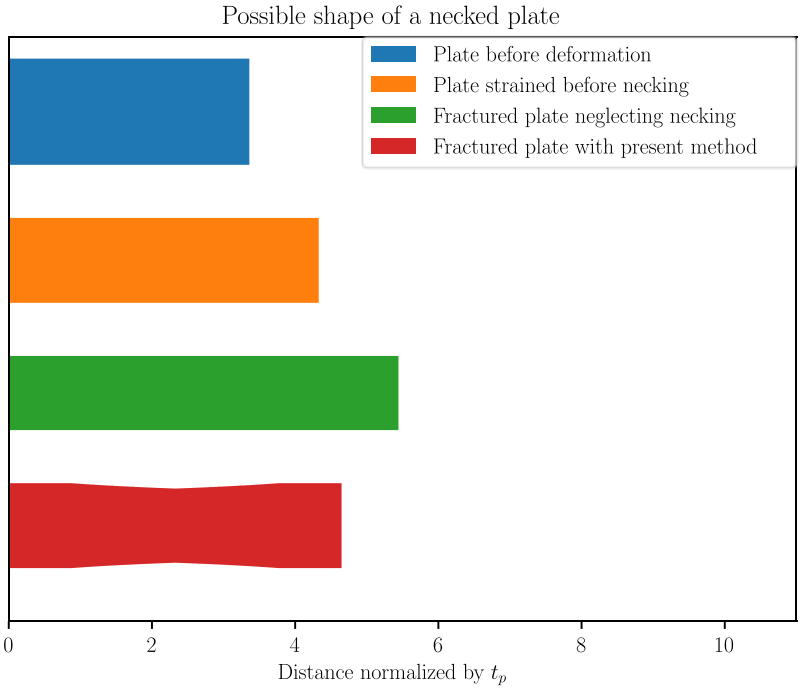

Figure 37 Proposed thickness of a cross section of an element after a raking test.

8 Discussion

8.1. Introduction

This thesis uses a higher-order model of a plate loaded at different stress states to estimate the error of previously proposed methods for fracture initiation prediction for shell element sizes in the order of the length of a neck for ductile material with hardening behaviour. While the impact of the basic assumptions is addressed in the literature review, one might argue that the effects of those unaddressed topics are significant. That is why several issues in the author's opinion have a considerable impact are discussed in this chapter.

Outline

The first influences are the ones that are impacting the point of and development of necking (Paragraph 8.2). After that, the way the simulated plate is loaded is discussed (Paragraph 8.3).

8.2. Localisation and Post-Necking Behaviour

Currently, only geometrical inhomogeneity of a plate is assumed in a simplistic manner as an imperfection band. The magnitude of this imperfection was adjusted to reflects the found necking strain or to precede fracture in equi-biaxial stress state as no necking is observed in that state. However, not all influences on necking were used in the model; other influences are:

- Geometrical variation (Gorji, Manopulo, et al., 2016).
- Porosity (Zheng et al., 2020).
- Anisotropy (Brunet & Morestin, 2001).
- Strain rate and thermal dependency as changes in the hardening model influence the FLD.

8.3. Difference in Loading

During crash scenarios, the material is stretched and bend at the same time, which is different and analysed by He et al. [2013], amongst others, in continuous bending tension tests, but the FLD is estimated to be higher due to deformation due to friction. The current approach does not consider bending of the material and may, in this case, underestimate the necking strain.

The plastic deformation in crash scenarios is applied by one-sided pressure and friction with the contact surface of the striking object. This may inhibit necking formation in one side, which is not considered in this thesis.

9 Conclusion

9.1. Introduction

This thesis is set out to answer: **How can ductile fracture strains for hardening materials be converted to effective fracture strains in shell elements with practical dimensions for crash simulation?**
As of now, it is not clear how the neck influences the effective fracture strain of shell elements. This question is answered partly by the following research questions:

1. **How can the accuracy of stress state dependent ductile fracture prediction models for shell elements be evaluated?**
2. **How do fracture strains in solids translate to effective fracture strains in shells smaller than five times the plate thickness?**
3. **What are the effects of boundary conditions on through-thickness necking?**
   Plates are often modelled with shell elements. In this thesis, detailed models of plates are made with solid elements that represent the shell elements, which requires boundary conditions that accurately represent a shell in a field of shell elements in a real structure.

These are answered in the following paragraph with the main research question answered in the previous chapter as an exact procedure.

9.2. Accuracy Evaluation of Fracture Prediction Method

This paragraph aims to answer the first research question:
"*How can the accuracy of stress state dependent ductile fracture prediction models for shell elements be evaluated?*".
This question is answered by providing a benchmark model in chapter 4 that simulates deformation and post-through-thickness necking based on the MK-analysis. With the assumption that a thickness imperfection of 0.5, 1, or 1.5% in a band will induce necking in a plate comparable to what would happen in an experiment.
The plate model is calibrated in Chapter 5, with results from Pack and Mohr [2017]. Pack and Mohr [2017] did not mention whether periodic boundaries or only nodal displacements were used. Therefore, both boundaries are simulated and compared, both lead to similar necking strains. The solid and shell element plate model uses periodic boundary conditions as it is meant to model a part of an infinite plate. The imperfection of the plate model is calibrated with a fracture strain at a stress state at which no necking was observed. This resulted in a one percent imperfection with neck orientations, as shown in Table 5, which are used for the solid MK model.

The accuracy is determined of correction methods in Chapter 6. This is done by looking at the deviation of equivalent plastic fracture strain of virtual shells and those obtained from correction methods.
The expectations that the EFFLD scales with l_e/t_p with the stress state is confirmed in paragraph 6.3 and 6.6. Also, shells cannot capture the through-thickness localisation accurately (Paragraph 6.3), especially for element sizes equal to their plate thickness or larger, as the effect of necking increases. The expectation that fracture loci, such as HC or MMC can be applied to shells is valid (Pack & Mohr, 2017), but with a margin of error and a constant element size. Correction methods improve the accuracy of fracture prediction methods (Paragraph 6.5 and 6.6), especially when necking strains are accurate. Both methods proposed in this thesis and in Walters [2014] can perform with high accuracy (Paragraph 6.6). However, the present method can predict fracture strain for smaller elements, while the other correction methods cannot (Paragraph 6.6). The forming limit diagram is for this material best estimated with a hardening model which can capture the hardening of experiments with the highest accuracy (in this case Voce-Swift is used) applied in Hill's necking criterion and an MK HC fit combination (Paragraph 6.7).

9.3. Fracture Strain from Solid to Shell

This paragraph aims to answer the second research question:
"*How do fracture strains in solids translate to effective fracture strains in shells smaller than five times the plate thickness?*". This is done by in Paragraph 3.6 estimating the shape of a neck and how a shell would interpret it in terms of effective first principal true fracture strain ε_1^{f*} in equation 3.40 and 3.41. Alternative methods that calculate the effect of the neck are presented in Paragraph 3.5. These methods use a relation of the necking, fracture and effective fracture strain, which is either inverse-linearly (Walters, 2014) or non-linearly (Bijleveld et al., 2018) dependent on the element size. These relations require the fracture and necking strain for which FFLD (Paragraph 3.2) and FLD (Paragraph 3.4) are presented, respectively. As an alternative to experimentally determining fracture strain the failure criteria as defined by classification institutes are presented in Paragraph 3.3.

9.4. Impact of Boundary Conditions on Necking

By comparing the periodic boundary conditions or purely nodal displacement-controlled boundary conditions on the shell plate model, the third research question "*What are the effects of boundary conditions on through-thickness necking?"* is answered.
The conventional MK analysis agrees the most with the plate model with periodic boundary conditions for $-0.5 \leq \alpha \leq 0$ and the nodal displacement-controlled plate model for $0 < \alpha \leq 1$. The orientation of the necking band for which the necking strain is the lowest varies with each model for $-0.5 \leq \alpha \leq 0.1$. The plate model

with periodic boundary conditions is, in theory, a part of an infinite plate, as suggested by MK-analysis. While using exact nodal displacements represents a plate with the exact dimensions.
The nodal displacement-controlled boundary conditions apply specific strains at the edges of the plate disabling strain localisation near the edges and may cause stress concentrations instead. This reduces the effect of necking and increases necking strain.

9.5. Effective fracture strains in shell elements.

This paragraph aims to answer the main research question: "*How can ductile fracture strains for hardening materials be converted to effective fracture strains in shell elements with practical dimensions for crash simulation?*". This question is answered partially by the sub research questions which were answered in Paragraph 9.2-9.4. The complete answer was given in the form of a proposed procedure (Chapter 7). This procedure models the strain inside and outside the neck using the necking strain, fracture strain, element length and neck length (Paragraph 3.6).
The fracture strain is obtained from a Hosford Coulomb fracture locus (Mohr & Marcadet, 2015) for plane stress. This locus requires a minimum of two experiments that each fracture at a different average stress state within plane stress.
The necking strain is obtained in Paragraph 7.3 by combining the necking criterion defined by Hill [1952] (Paragraph 3.4) and a fit of the Hosford Coulomb model proposed by Pack & Mohr [2017]. These criteria require a hardening model, in this case the Voce-Swift hardening model in equation 2.20, calibrated with a tensile test. This tests also provides the neck length, which is in this case assumed two times the plate thickness (Paragraph 6.6).
The effective fracture strain is directly obtained through equation 7.7 and is applied on a raking experiment from Haag [2017]. The effective fracture strains are comparable to the test results obtained through digital image correlation.
With this procedure the ductile fracture strains for hardening models can be converted to effective fracture strains for shell elements for all element lengths.

10 Recommendations

10.1. Introduction

Based on all the findings of this thesis and the preceding literature review, recommendations are made on how ductile fracture initiation can be predicted in shells. This chapter concludes with a framework when certain methods are recommended with which assumptions are applicable. For explanation, one is directed to the specific paragraphs of this chapter, which also include references to research within this thesis and articles outside of it.

Caveats

The proposed method has assumptions to reduce complexity, computation time, and effort to implement. In return, one might have different findings using more complex models that use, for example, non-associated plasticity, different element types and sizes. The resources for every study are finite as otherwise, one could propose to use exceptionally fine solids, strain rate dependent hardening, anisotropic hardening, or to apply random distributions to the properties of solid elements for a large number of simulations. The random distributions would vary the hardening model, fracture, porosity, and geometrical imperfection.

10.2. The Role of Minimizers in Locus Calibration

Using minimizers in combination for locus calibration is not new as in Bai & Wierzbicki [2009], and Cerik et al. [2018] used it. Still, it was named different, and not referenced as it is a logical manner of calibration. Use of a minimizer is recommended as using average stress states of the fractured element/volume is only valid if the load path is constant. The error can also aid in detecting errors introduced in simulations due to details are assumed negligible. These are, for example: imperfections, strain rates in experiments, anisotropy, temperature dependency, and accuracy of location of fracture initiation. When the error is significantly higher than reported then a assumption or model is incorrect. For reference, Cerik et al. [2018] and Park et al. [2019] obtained for DH36 and EH36 about 6% NAE with the HC and MMC fracture locus.

10.3. Steel Grade and Locus Estimation

Park et al. [2019] show that the fracture loci of same steel grade materials vary and using one parameter to calibrate a material does not suffice for calibrating a fracture locus for solids. However, FLD for shells can be calibrated using one tensile test or estimated using empirically determined averages of hardening parameters for the Swift power law (Swift, 1952), as Cho et al. [2015] provided estimates for engineering stress strain curves based on statistics. This through-thickness necking was shown for S235JR to precede

fracture, except the equi-biaxial stress state and Pack & Mohr [2017] assumed this to also be the case for the uni-axial stress state based on experiments on DP steel. However, both Pack & Mohr [2017] and Walters [2014] assumed that fracture could precede necking. This assumption requires 3 calibration tests for an accurate fracture model and necking model, which motivates the desire to look whether necking could be used as a failure model as Storheim et al. [2015], amongst other, applied it relatively successfully. The hypothesis is that the material is ductile enough to form through-thickness strain localisation before fracture. This can be an underestimation with backing from previous tests from the same steel grade. This assumption can be validated with a test around plane strain and stress state and check whether necking precedes fracture as this is the lowest point for both necking and fracture. Another method is by using one test and with about 6 to 10% variation in fracture strain and compose a minimal possible fracture locus for the plane stress state and use it when it precedes the FLD found by MK or DSSE.

10.4. Framework

A solid framework for implementation of stress state dependent ductile fracture prediction in a shell is recommended in chapter 7 for easy implementation.
An alternative lowest effort method requires a minimum of one calibration test, but more would provide more certainty. The hardening model is calibrated using a tensile test preferably with an analytical solution before necking occurs and an estimate based on inverse engineering for post necking. The FLD is estimated by preferably MK analysis (either by DSSE or general method, but a lower estimate can be made with BWH), with the imperfection calibrated for diffuse necking at uni-axial stress state or the hardening parameter “n” at plane strain can be used. Alternatively, one can use the fracture strain of a test at which no necking preceded as a lower bound, for example, a punch test. Afterwards, a lower bound FFLD is estimated with a preferred six to ten percent RMSE using either MMC or HC. The lowest value of either of the FFLD or FLD is to be used for the EFFLD.
This method is recommended for low efforts, and higher accuracy than RP’s, especially for element sizes larger than 7.5 time the plate thickness.

10.5. Possible Extension of Plate Model

The proposed framework does not use the presented solid element plate model as in its current shape, it is too computationally expensive. However, for research a similar model could be interesting as material properties can be added. For this application a faster model is desirable, which can be achieved with:

- By assuming symmetry would cut the model in half, or quarter, or eight when considering anisotropy, or orthotropy, or isotropy, respectively.

- By making the plate size only on the relevant scale as only a section of an infinite plate is modelled, which is about 7.5 times the plate thickness, which would result in about a seventh of the model.
- By stopping the simulation when a fracture strain is obtained, as the current model stops at a fracture strain of three.
- By limiting the number of stress states assessed.
- By only simulating the neck or the neck with a small portion of the outer material. When the maximum neck size is about two times the plate thickness, the model is reduced to a tenth.

A scenario could be that isotropy is assumed, only a relevant portion of the plate is simulated, and simulations stop when fracture is detected. Future analysis could be fast as the material assessed in this thesis was highly ductile. This means that simulations are longer as timesteps after massive plastic deformation take the most time.

Bibliography

Alsos, H. S., Hopperstad, O. S., Törnqvist, R., & Amdahl, J. (2008). Analytical and numerical analysis of sheet metal instability using a stress based criterion. *International Journal of Solids and Structures*, *45*(7–8), 2042–2055. https://doi.org/10.1016/j.ijsolstr.2007.11.015

Arrioux, R., Bedrin, C., & Boivin, M. (1982). Determination of an intrinsic forming limit stress diagram for isotropic metal sheets. *Proceeding of the 12th Biennial Congress IDDRG*, 61–71.

Bai, Y, Luo, M., Li, Y., & Wierzbicki, T. (2008). *Calibration of TRIP steel sheet (RA-K40/70) for fracture*.

Bai, Y, & Wierzbicki, T. (2008a). A new model of metal plasticity and fracture with pressure and Lode dependence. *International Journal of Plasticity*, *24*(6), 1071–1096. https://doi.org/10.1016/j.ijplas.2007.09.004

Bai, Y, & Wierzbicki, T. (2008b). Forming severity concept for predicting sheet necking under complex loading histories. *International Journal of Mechanical Sciences*, *50*(6), 1012–1022. https://doi.org/10.1016/j.ijmecsci.2008.02.010

Bai, Y, & Wierzbicki, T. (2009). Application of extended Mohr–Coulomb criterion to ductile fracture. *International Journal of Fracture*, *161*(1), 1. https://doi.org/10.1007/s10704-009-9422-8

Bao, Y., & Wierzbicki, T. (2003). *Prediction of ductile crack formation in uncracked bodies (Doctoral thesis)* (Massachusetts Institute of Technology). Retrieved from http://hdl.handle.net/1721.1/17634

Bijleveld, F. W. (2018). *Stress-state dependent fracture prediction : An application in numerical analysis of maritime collision (Master's thesis)* (Delft University of Technology). Retrieved from http://resolver.tudelft.nl/uuid:e5fd9747-f490-466a-b783-fcc4c6771469

Bijleveld, F. W., Hoogeland, M. G., Walters, C. L., & Van Bergen, J. W. (2018). A practical approach to ductile material failure during raking collisions. *Proceedings of the International Offshore and Polar Engineering Conference*, *2018-June*, 1599–1607.

Bressan, J. D., & Williams, J. A. (1983). The use of a shear instability criterion to predict local necking in sheet metal deformation. *International Journal of Mechanical Sciences*, *25*(3), 155–168. https://doi.org/10.1016/0020-7403(83)90089-9

Brunet, M., & Morestin, F. (2001). Experimental and analytical necking studies of anisotropic sheet metals. *Journal of Materials Processing Technology*, *112*(2), 214–226. https://doi.org/https://doi.org/10.1016/S0924-0136(01)00578-7

Cerik, B. C., Park, S.-J., & Choung, J. (2018). Ductile Fracture Modeling of DH36 Grade Steels. *Omae-2018*, V11AT12A008. https://doi.org/10.1115/omae2018-78681

Cho, S.-R., Choi, S.-I., & Son, S.-K. (2015). Dynamic material properties of marine steels under impact loadings. *Proceedings of the 2015 World Congress on Advances in Structural Engineering and Mechanics, ASEM15, Incheon, Korea*.

Considère, A. (1885). *Mémoire sur l'emploi du fer et de l'acier dans les constructions, Annales des ponts et chaussées I sem*.

Coulomb, C. A. (1776). *Essai sur une application des règles de maximis & minimis à quelques problèmes de statique, relatifs à l'architecture*. Paris : De l'Imprimerie Royale, 1776.

Det Norske Veritas. (2010). Design against accidental loads. In *Recommended Practice DNV-RP-C204*. Høvik, Norway.

Det Norske Veritas. (2013). Determination of structural capacity by non-linear FE analysis methods. In *Recommended Practice No. DNV-RP-C208, Det Norske Veritas GL AS, Oslo*. Retrieved from www.dnvgl.com.

Dunand, M., & Mohr, D. (2010). Hybrid experimental-numerical analysis of basic ductile fracture experiments for sheet metals. *International Journal of Solids and Structures*, *47*(9), 1130–1143. https://doi.org/10.1016/j.ijsolstr.2009.12.011

Ehlers, S. (2009). A procedure to optimize ship side structures for crashworthiness. *Proceedings of the Institution of Mechanical Engineers, Part M: Journal of Engineering for the Maritime Environment*, *224*(1), 1–11. https://doi.org/10.1243/14750902JEME179

Ehlers, S., Broekhuijsen, J., Alsos, H. S., Biehl, F., & Tabri, K. (2008). Simulating the collision response of ship side structures: a failure criteria benchmark study. *International Shipbuilding Progress*, *55*(1–2), 127–144.

Goodwin, G. M. (1968). Application of strain analysis to sheet metal forming problems in the press shop. *Sae Transactions*, 380–387.

Gorji, M., Berisha, B., Hora, P., & Barlat, F. (2016). Modeling of localization and fracture phenomena in strain and stress space for sheet metal forming. *International Journal of Material Forming*, *9*(5), 573–584. https://doi.org/10.1007/s12289-015-1242-y

Gorji, M., Manopulo, N., Hora, P., & Barlat, F. (2016). Numerical investigation of the post-necking behavior of aluminum sheets in the presence of geometrical and material inhomogeneities. *International Journal of Solids and Structures*, *102–103*, 56–65. https://doi.org/https://doi.org/10.1016/j.ijsolstr.2016.10.017

Gurson, A. L. (1977). Continuum theory of ductile rupture by void nucleation and growth: Part I—Yield criteria and flow rules for porous ductile media. *Journal of Engineering Materials and Technology*, *99*(1), 2–15.

Haag, S. R., Hoogeland, M. G., Vredeveldt, A. W., & Kaminski, M. L. (2017). *Ship Grounding Damage: An Estimate through Acceleration Measurements (Master's thesis)* (Delft University of Technology). https://doi.org/10.1115/omae2017-61732

Hancock, J. W., & Mackenzie, A. C. (1976). On the mechanisms of ductile failure in high-strength steels subjected to multi-axial stress-states. *Journal of the Mechanics and Physics of Solids*, *24*(2), 147–160.

https://doi.org/https://doi.org/10.1016/0022-5096(76)90024-7

He, J., Cedric Xia, Z., Zeng, D., & Li, S. (2013). Forming limits of a sheet metal after continuous-bending-under-tension loading. *Journal of Engineering Materials and Technology*, *135*(3).

Hill, R. (1952). On discontinuous plastic states, with special reference to localized necking in thin sheets. *Journal of the Mechanics and Physics of Solids*, *1*(1), 19–30. https://doi.org/10.1016/0022-5096(52)90003-3

Hollomon, J. H. (1945). Tensile deformation. *Aime Trans*, *12*(4), 1–22.

Hwang, Y.-M., Lin, Y.-K., & Chuang, H.-C. (2009). Forming limit diagrams of tubular materials by bulge tests. *Journal of Materials Processing Technology*, *209*(11), 5024–5034. https://doi.org/https://doi.org/10.1016/j.jmatprotec.2009.01.026

Johnson, G. R., & Cook, W. H. (1985). Fracture characteristics of three metals subjected to various strains, strain rates, temperatures and pressures. *Engineering Fracture Mechanics*, *21*(1), 31–48. https://doi.org/10.1016/0013-7944(85)90052-9 LK - https://tudelft.on.worldcat.org/oclc/4923063787

Keeler, S. P. (1961). *Plastic instability and fracture in sheets stretched over rigid punches*. Massachusetts Institute of Technology.

Lee, Y. (2005). Fracture Prediction in Metal Sheets (Doctoral thesis) (Massachusetts Institute of Technology). Retrieved from http://hdl.handle.net/1721.1/33560

Malvern, L. E. (1969). Introduction to the Mechanics of a Continuous Medium. In *Journal of Applied Mechanics* (Vol. 33). https://doi.org/10.1115/1.3625016

Marciniak, Z., Kuczyński, K., & Pokora, T. (1973). Influence of the plastic properties of a material on the forming limit diagram for sheet metal in tension. *International Journal of Mechanical Sciences*, *15*(10), 789–800. https://doi.org/10.1016/0020-7403(73)90068-4

McClintock, F. A. (1968). A Criterion for Ductile Fracture by the Growth of Holes. *Journal of Applied Mechanics*, *35*(2), 363–371. https://doi.org/10.1115/1.3601204

Mohr, D., & Marcadet, S. J. (2015). Micromechanically-motivated phenomenological Hosford-Coulomb model for predicting ductile fracture initiation at low stress triaxialities. *International Journal of Solids and Structures*, *67–68*, 40–55. https://doi.org/10.1016/j.ijsolstr.2015.02.024

Pack, K., & Mohr, D. (2017). Combined necking & fracture model to predict ductile failure with shell finite elements. *Engineering Fracture Mechanics*, *182*, 32–51. https://doi.org/10.1016/j.engfracmech.2017.06.025

Park, S.-J., Lee, K., Cerik, B. C., & Choung, J. (2019). Comparative Study on Various Ductile Fracture Models for Marine Structural Steel EH36. *J. Ocean Eng. Technol.*, *33*(3), 259–271. https://doi.org/10.26748/KSOE.2019.038

Park, S. J., Lee, K., Cerik, B. C., & Choung, J. (2019). Ductile fracture prediction of EH36 grade steel based

on Hosford–Coulomb model. *Ships and Offshore Structures*, *0*(0), 1–12. https://doi.org/10.1080/17445302.2019.1565300

Park, S. J., Lee, K., Choung, J., & Walters, C. L. (2018). Ductile fracture prediction of high tensile steel EH36 using new damage functions. *Ships and Offshore Structures*, *13*, 68–78. https://doi.org/10.1080/17445302.2018.1426433

Rice, J. R., & Tracey, D. M. (1969). On the ductile enlargement of voids in triaxial stress fields*. *Journal of the Mechanics and Physics of Solids*, *17*(3), 201–217. https://doi.org/10.1016/0022-5096(69)90033-7

Roth, C. C., & Mohr, D. (2016). Ductile fracture experiments with locally proportional loading histories. *International Journal of Plasticity*, *79*, 328–354. https://doi.org/10.1016/j.ijplas.2015.08.004

Safikhani, A. R., Hashemi, R., & Assempour, A. (2009). Some numerical aspects of necking solution in prediction of sheet metal forming limits by strain gradient plasticity. *Materials & Design*, *30*(3), 727–740. https://doi.org/https://doi.org/10.1016/j.matdes.2008.05.028

Scharrer, M., Zhang, L., & Egge, E. D. (2002). Collision calculations in naval design systems. *Report Nr. ESS*.

Stören, S., & Rice, J. R. (1975). Localized necking in thin sheets. *Journal of the Mechanics and Physics of Solids*, *23*(6), 421–441. https://doi.org/https://doi.org/10.1016/0022-5096(75)90004-6

Storheim, M., Amdahl, J., & Martens, I. (2015). On the accuracy of fracture estimation in collision analysis of ship and offshore structures. *Marine Structures*, *44*, 254–287. https://doi.org/10.1016/j.marstruc.2015.09.006

Stoughton, T. B., & Zhu, X. (2004). Review of theoretical models of the strain-based FLD and their relevance to the stress-based FLD. *International Journal of Plasticity*, Vol. 20, pp. 1463–1486. https://doi.org/10.1016/j.ijplas.2003.11.004

Swift, H. W. (1952). Plastic instability under plane stress. *Journal of the Mechanics and Physics of Solids*, *1*(1), 1–18. https://doi.org/10.1016/0022-5096(52)90002-1

Tang, L., Walters, C. L., & Heuvel, W. (2015). Effect of gage length on failure strain. *ECM*. Retrieved from http://resolver.tudelft.nl/uuid:fe61bf2f-ff2e-48e5-8de3-fd9ca24ff111

Tvergaard, V., & Needleman, A. (1984). Analysis of the cup-cone fracture in a round tensile bar. *Acta Metallurgica*, *32*(1), 157–169. https://doi.org/10.1016/0001-6160(84)90213-X

Tvergaard, Viggo. (1982). On localization in ductile materials containing spherical voids. *International Journal of Fracture*, *18*(4), 237–252. https://doi.org/10.1007/BF00015686

Voce, E. (1948). The relation between stress and strain for homogeneous deformation. *Journal of the Institute of Metals*, *74*, 537–562. Retrieved from http://www.csa.com/partners/viewrecord.php?requester=gs&collection=TRD&recid=18807CD%5Cnpapers2://publication/uuid/90C2A327-78EF-47F3-992D-0DE4A6348220

Voormeeren, L. O., Walters, C. L., Tang, L., & Vredeveldt, A. W. (2014). Estimation of Failure Parameters for Finite Element Simulations Based on a Single State of Stress and Arbitrary Stress-Strain Relation. *Proceedings of the ASME 2014 33rd International Conference on Ocean, Offshore and Arctic Engineering OMAE2014*, (45455). https://doi.org/10.1115/omae2014-23900

Walters, C. L. (2014). Framework for adjusting for both stress triaxiality and mesh size effect for failure of metals in shell structures. *International Journal of Crashworthiness*, *19*(1), 1–12. https://doi.org/10.1080/13588265.2013.825366

Wierzbicki, T., & Xue, L. (2005). On the effect of the third invariant of the stress deviator on ductile fracture. *Impact and Crashworthiness Laboratory, Technical Report*, *136*.

Zheng, X., N'souglo, K. E., Rodríguez-Martínez, J. A., & Srivastava, A. (2020). Dynamics of Necking and Fracture in Ductile Porous Materials. *Journal of Applied Mechanics*, *87*(4). https://doi.org/10.1115/1.4045841